Coherent spectroscopy of single quantum dots

John Howard Quilter

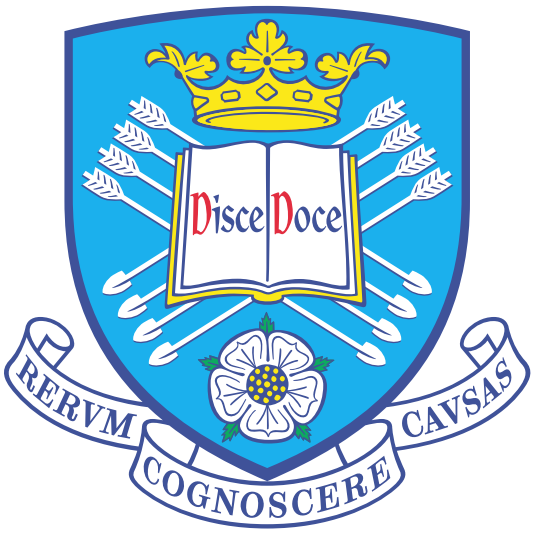

Department of Physics and Astronomy
The University of Sheffield

Thesis submitted for the degree of Doctor of Philosophy

December 2014

Acknowledgements

Firstly, I'd like to thank my supervisors Prof Mark Fox and Prof Maurice Skolnick for giving me the opportunity to study for my PhD in the LDSD group at Sheffield. Secondly, Andrew Ramsay for teaching me so much throughout the process and for being so incredibly dedicated to the project. Thirdly to Tim Godden, Rikki Coles, Alistair Brash and Feng Liu, with whom I have worked with on the experiments for this project over the past four years. I'd like to thank the collaborating team at Universiät Bayreuth for their excellent path integral calculations that feature in Chapter 6: Martin Glässl, Andreas Barth and Martin Axt. Big thanks to all members of the LDSD group for their helpful discussions and for making the LDSD such an excellent and enjoyable group to work in, particularly D Sercombe, J Chana, S Swartz, A Waeber, D Vaitiekus, J Dixon, M Durska, K Guda, N Wasley, J Peubla-Nunez, O Del Pozo Zamudio, R Toro, A Foster, M Sich, J Bradley, C Bentham, S Dufferweil, L Tinkler, M Woodhouse, M Pearce, D Davies, C Atkins, E Daghigh Ahmadi, R Hussain, I luxmoore, E Checkovich, T Goode, D Sakar, J O'Hara, R Schofield, M Hemmingway, N porter, R Bradley, P Walker, M Makhonin, B Royal, D Revin, N Prtljaga, J Orchard, F Li, A Ul Haq, B Dzurnak, F Fras, O Couto Jr, D Khrizanovskii, L Wilson, A Tartakovskii, P Kok, D Whittaker and D Mowbray.

I'm very grateful for the assistance of the following people during my time at Sheffield: Chris Vickers and Pete Robinson in the helium liquefier, Paul Kemp-Russell and the other workshop staff, All the III-V centre staff, especially N Babazedah and P Fry for helping with sample fabrication. Even though I never had the pleasure of meeting Yanwen Wu and M. Hopkinson, these experiments would not have been possible without the now-legendary single-dot wafer that they grew long ago. Thanks also to the department office staff for quickly dealing with my messy paperwork. For the funding to carry out this research, I'm grateful to the EPSRC.

I'd like to thank all of my family, especially my parents and sister, and also friends for being so supportive while I've been studying and finally thank you to my loving girlfriend Elie, who's been there for me throughout.

Cheers everyone!

Abstract

This thesis presents experiments carried out into the coherent properties of charge carriers confined within a single InGaAs/GaAs quantum dot. Specifically the ground state - single exciton qubit system is controlled with ultrafast optical pulses and then the population of the dot is measured by a high-sensitivity photocurrent detection technique. There are two principal results of these experiments, firstly by modulating the bias applied to the quantum dot diode, the detection efficiency of the photocurrent measurement technique is enhanced. The enhancement is possible as the modulated bias allows fast switching of the voltage-dependent carrier tunneling rates. Secondly, when the transition is addressed by an intense, positively detuned laser, the qubit system can be driven to a population inversion. This occurs due to phonon-assisted relaxation of the optical dressed states of the system. Here, the rapid thermalization due to the exciton-phonon interaction actually enables the population inversion, instead of simply being a source of decoherence.

List of Publications

Phonon-assisted population inversion of a single quantum dot

J. H. Quilter, A. J. Brash, F. Liu, M. Glässl, A. M. Barth, V. M. Axt, A. J. Ramsay, M. S. Skolnick and A. M. Fox
Currently under review for *Physical Review Letters*, ArXiv ID: arXiv:1409.0913 (2014).

Enhanced photocurrent readout for a single quantum dot qubit by bias modulation

J. H. Quilter, R. J. Coles, A. J. Ramsay, A. M. Fox, M. S. Skolnick
Applied Physics Letters 102 181108 (2013)

Fast preparation of a single-hole spin in an InAs/GaAs quantum dot in a Voigt-geometry magnetic field

T. M. Godden, J. H. Quilter, A. J. Ramsay, Yanwen Wu, P. Brereton, I. J. Luxmoore, J. Puebla, A. M. Fox, M. S. Skolnick
Physical Review B 85 155310 (2012)

Coherent Optical Control of the Spin of a Single Hole in an InAs/GaAs Quantum Dot

T. M. Godden, J. H. Quilter, A. J. Ramsay, Yanwen Wu, P. Brereton, S. J. Boyle, I. J. Luxmoore, J. Puebla-Nunez, A. M. Fox, M. S. Skolnick
Physical Review Letters 108 017402 (2012)

Contents

List of Figures

Chapter 1

Introduction

1.1 Quantum Information Processing

Current computer processors make use of logic gates made up of billions of transistors. Each transistor acts as an electronic switch, which can be assigned one of two available logic states (1 or 0) and is known as a bit. For decades, computing power has been increased simply by increasing the number of bits that make up the processor, via technological improvements that are pushing the miniaturization of transistors to the limit of semiconductor lithography techniques. Ultimately, transistors that switch on a single-electron basis represent a fundamental barrier to miniaturization, where the laws of quantum mechanics will be applicable.

Further improvements in processor technology will cease to follow Moore's Law (that the number of transistors on a chip will double every year [1]) and more powerful chips will have to be physically larger. Applications such as modelling quantum-mechanical structures and other complex phenomena, and factoring large numbers for cryptography purposes, will require computing demands that cannot be met with conventional technology. One proposed solution is to use quantum-mechanical objects as quantum-bits, or qubits, in a quantum computer. Unlike a classical bit, which is limited to having possible values of 1 or 0, a qubit can exist in coherent superpositions of these states, described by a wavefunction:

$$\psi_{\text{qubit}} = c_0|0\rangle + c_1|1\rangle, \tag{1.1}$$

where c_0 and c_1 are complex coefficients; the normalization condition is $|c_0|^2 + |c_2|^2 = 1$.

Quantum parallelism

In classical computing, logical operations mean switching the value of bits between $|0\rangle$ and $|1\rangle$. Demanding computing tasks are handled by a classical computer by repeating certain logic operations on a series of initial values. If the task requires more calculations to be made then it takes a longer time. As initially suggested by Feynman [2]

and Deutsch [3], this is not the case for a quantum computer. Since quantum logic operations are performed on superposition states, they are performed on $|0\rangle$ and $|1\rangle$ *simultaneously*. If two qubits are considered, the operation can be performed on a superposition of 4 states and in general, for N qubits, a superposition of 2^N states can be manipulated. This is an important advantage for quantum computers over their classical counterparts and is known as *quantum parallelism*. A system containing just a small number of qubits can calculate the final values for a large number of inputs simultaneously. Shor's algorithm [4] is an example of quantum computation used to solve a specific problem: finding the prime factors of an n-digit integer. Classically, the time taken to solve the problem scales exponentially with n, whereas with a quantum computer, this increase in time is polynomial with n. For large values of n, there is a huge difference in the processing time for the two different computers, with the quantum computer being by far the fastest.

1.1.1 DiVincenzo criteria

A viable quantum computer must meet the following set of criteria, as set out by David DiVincenzo in 2000 [5]:

A scalable physical system with well characterized qubits

For the qubit to be well-characterized, its physical parameters must be well known. This means that the eigenstates of the system must be identified, as well as any potential interactions with other states or external fields. Scalability necessitates a large number of individual qubits that can all be addressed.

The ability to initialize the state of the qubits to a simple fiducial state

In order to begin computation, the qubit register must first be initialized into a known state. One of the requirements of quantum error correction is an ongoing supply of qubits that are initialized in the $|0\rangle$ state.

Long relevant decoherence times, much longer than the gate operation time

If the qubit loses coherence then, instead of a superposition, the gate operation will attempt to act on an incoherent mixture of states. For fault-tolerant quantum computation, coherence times a factor of $10^4 - 10^5$ longer than gate operation times are necessary.

A "universal" set of quantum gates

As in classical computing, operations that manipulate qubits are called gates. A universal set of quantum gates is a set of gates to which any operation that is possible on a quantum computer can be reduced. The smallest possible universal quantum system is a two-qubit gate [6].

A qubit-specific measurement capability

After an algorithm is performed, the state of qubits in the register must be read-out. Ideally the measurement should not perturb other nearby qubits.

1.1.2 Qubit contenders

Due to the range of physical systems that can be coherently controlled, several different potential candidates for qubit implementation are currently being investigated. Some of the most well-studied of these are as follows:

Photonic qubits

The polarization state of a single photon is used to encode the qubit superposition and a series of wave-retardation plates are used to manipulate it [7]. Due to their constant motion, photons are referred to as 'flying' qubits as opposed to 'stationery' qubits, such as the other entries in this list. Photons are considered to be excellent carriers of quantum information between 'stationery' qubits due to their lack of interactions with the environment or each other. This means that the quantum state is not dephased during transit.

Trapped ions

Ion traps rely on using electromagnetic fields to isolate an individual ion [8, 9]. A qubit can be formed between the ground state and an excited state, and also between the vibrational states of the ion. The qubit can be addressed with a laser for high-fidelity operation.

Impurity centres in crystals

Crystal impurities, such as optically active nitrogen vacancy centres in a diamond crystal [10] or impurities in silicon crystals [11] can provide an isolated electron spin. Transitions between different spin states are used as the basis of a solid-state system. Currently these qubits offer the highest fidelity gate operations and longest coherence times for any system.

Atomic nuclei

Nuclear magnetic resonance experiments can be used to control the spin state of atomic nuclei in several material systems [12].

Josephson junctions

Qubits can be formed from either the charged state of the junction, the direction of the current flow or from transitions to excited states [13].

Quantum dots

Individual electronic carriers and excitons can be localized on the quantum dot (QD) and their spins manipulated [14] by optical, electronic or spin-resonance techniques.

1.1.3 Quantum dots

Quantum dots are man-made structures that are small enough to be comparable to the de Broglie wavelength for charge carriers in the semiconductor, allowing quantum confinement in all three dimensions. QDs can be formed in a variety of ways, such as: epitaxial island-like crystal growth in a solid, fluctuations in the thickness of a quantum well, colloidal nano-particles, variation in the crystal structure along a nanowire, and by electrically defining a localized potential in a 2D electron-gas. It is the first of these types of QD that are studied in this work: self-assembled QDs formed by localized crystal growth in a semiconductor, specifically InAs on a GaAs epilayer.

Advantages of using epitaxial QD qubits

Semiconductor QDs are a suitable qubit candidate because they offer an atom-like set of discrete energy levels and provide a stable solid-state environment without the need for complicated laser-traps. However, unlike individual atoms, they are man-made, so dot properties can be tailored during growth. QDs are optically active due to the direct semiconductor band-gap, making optical control a possibility. As semiconductors can be easily integrated into electronic circuits, electrical control and readout of the dot is possible. Devices and structures such as photonic crystals and micro-cavities can also be fabricated on the wafer, allowing QDs to be studied in conjunction with optical confinement methods.

Limitations of epitaxial QDs

The self-assembled nature of QD growth means that the QDs in the sample have a random distribution of sizes, positions and aspect ratios across the wafer. Currently, a great deal of work is being done both with site-controlled growth methods [15, 16] and QD registration techniques [17], which would be necessary in order to grow an array of QDs that could be used as an interacting set of qubits, or to precisely position a cavity structure relative to the QD location. Other possible limitations come from the two principal sources of dephasing for a coherent state in the QD. These are interactions with the nuclear spins that compose the QD and with phonons propagating through the crystal, as studied in this thesis in Chapter 6.

1.2 Chapter abstracts

Chapter 2: Background and review of literature

This Chapter presents a detailed overview of the physics of single QD qubits. The current state of the art is examined through a review of recent experiments presented in the literature.

Chapter 3: Experimental methodology

In this chapter, the details of the experimental set up used to carry out the experiments in chapters 4, 5 and 6 are discussed. Highly specialized techniques are required to coherently manipulate the quantum states of single dots. A detailed overview is presented of the sample wafer structure and processing steps, along with the optics and measuring circuit used to measure data.

Chapter 4: Characterization of quantum dot properties

Here, a summary of the properties of the individual QDs that are studied in this work is presented. These characteristics are important for the experiments that are presented in Chapters 5 and 6.

Chapter 5: Enhanced photocurrent readout for a quantum dot qubit by bias modulation

Coherent control of a quantum dot exciton using photocurrent detection is demonstrated with a sinusoidal reverse bias applied to the QD Shottky-diode structure. The aim of these experiments is to overcome the compromise between long exciton coherent lifetimes and the fast carrier tunneling required for a high photocurrent detection efficiency, by rapidly switching the bias voltage. Optical control is performed at low applied field strengths, where tunneling-limited coherence times are long. Following this step, the tunneling rates are increased to remove the long-lived hole, achieving a high photocurrent signal. For a detection efficiency of 68%, electron and hole tunneling times during optical control of 200 ps and 20 ns can be achieved, compared to 120 ps and 7 ns for the constant bias case, respectively. These experiments show that high photocurrent detection efficiencies can be achieved in conjunction with a long-lived exciton state.

Chapter 6: Phonon-assisted population inversion of a single Quantum Dot

A new approach to realize a population inversion of the excitonic two-level system through off-resonant optical excitation is demonstrated. The QD is driven by a laser pulse tuned within the high-energy phonon sideband of the neutral exciton. The population inversion is achieved by rapid thermalization of optically dressed states via phonon-induced relaxation. A maximum exciton population of 0.67 ± 0.06 is measured for a laser detuned by $+0.832$ meV and the phonon sideband is mapped as a function of both laser detuning and pulse area using a two-color pump-probe technique. These experiments are an important first step towards the realization of a thermal equilibrium between dressed states and a phonon-bath in the optical frequency regime. Traditionally, the interaction with phonons is one of the limitations to exciton coherence, but in

this scheme, they are essential.

Chapter 7: Conclusions and future work

The key experiemental results are summarized in a general conclusion and ideas for future experiments that would extend this work are presented.

Chapter 2

Background and review of literature

2.1 Semiconductor quantum dots

Stranski-Krastanov growth

The Stranski-Krastanov (SK) method is commonly used to grow QDs, where a contrasting semiconductor material (in this case InAs) is deposited on the surface of a crystal by molecular beam epitaxy (MBE). In this case, the substrate material is GaAs. These contrasting semiconductors have a 7% mismatch in their lattice constants, leading to strain between the two materials. InAs growth is epitaxial for the first few monolayers and a thin wetting layer of InAs forms; after this the strain becomes too large and it becomes more energetically favourable for additional InAs to self-assemble into small islands [18] (analogous to water droplets on a surface), rather than continuing as an even layer. All three dimensions of the QD are typically less than 100 nm in length. After the InAs deposition, the QD layer is capped with more GaAs, in order to suppress non-radiative pathways from exposed surface states. During the capping process, thermal annealing fixes the final shape and composition of the self-assembled QD (SAQD) and there is typically some diffusion of gallium into the dot, resulting in InGaAs QDs. In samples studied here, the shape is a truncated pyramid, with base diameter 25-30 nm and height 3-4 nm. Fig. 2.1 shows a scanning tunnelling microscope (STM) image of a cross section through a similar InAs QD, obtained by cleaving through the wafer and imaging QDs on the cleaved edge.

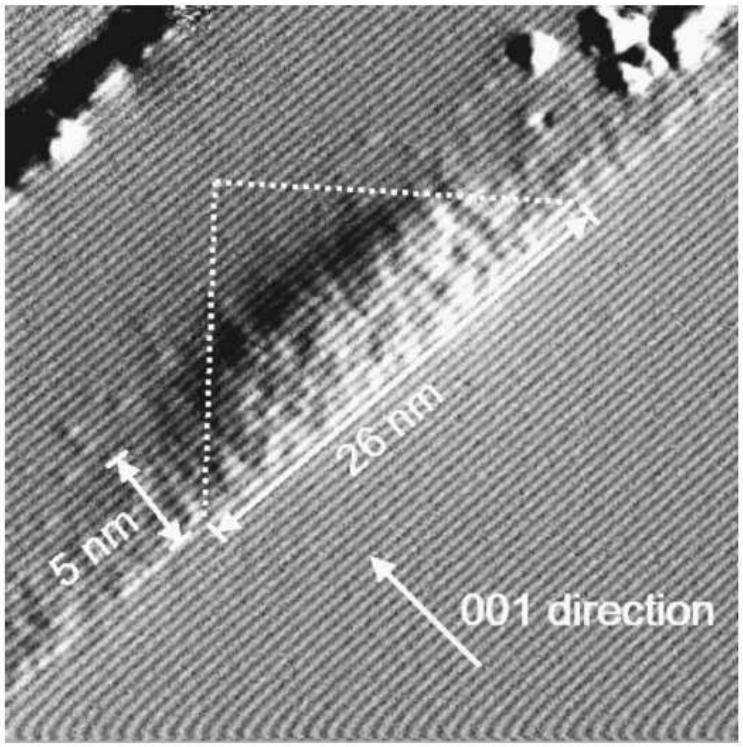

Figure 2.1: Cross-section STM image through a single InAs SK QD. The image shows a 40 nm × 40 nm area. The dashed white line indicates the un-truncated pyramid shape. The InAs wetting layer is visible extending from the QD base. From ref. 19, included with permission.

2.1.1 QD properties

Electron and hole energy levels

The energy level structure of a QD is very different from the band structure of the bulk material that the QD is made from. Firstly, the lower band gap of InGaAs compared with GaAs means that the reduced dimensionality of the QD results in 3D electronic confinement, with a discrete density of electronic states, rather than the continuum in the bulk material's valence and conduction bands. Secondly, the presence of strain in the crystal lattice of the QD further modifies the confinement potential experienced by carriers in the dot. As the crystal lattice is anisotropic, a piezoelectric field may also affect the potential, but this is usually considered to be a negligible effect for dots grown in GaAs unless the dot is grown on the (111) crystal plane. Calculations have been performed for QDs that are cylindrical or lens-shaped, with the radial direction in the growth plane. These calculations result in a radially symmetric confinement potential with the same energy spectrum as a 2D harmonic oscillator.

As the height of SAQDs is usually much less than the base diameter, electrons and holes are more strongly confined along the vertical (z) direction. Only the first vertically-confined state is usually considered due to the large energy gap before the

second level is reached. The in-plane angular motion of carriers allows a series of quantized orbitals, which take the form of circularly symmetric harmonic wavefunctions, analogous to the (spherically symmetric) shell structure usually found in atomic physics [20]. Shells are labelled $s, p, d...$ in accordance with the atomic physics convention of naming electron angular momentum orbitals. However, as the QD orbitals describe angular momentum in the plane only, a set of 2D orbitals are allowed. Compared with the atomic physics model (for a 3D harmonic oscillator), where the s, p, d... shells can support 1, 3, 5... degenerate pairs of opposite-spin electrons, respectively, the QD $s, p, d...$ shells can contain 1, 2, 3... electron (or hole) spin-pairs. Selection rules only allow electrons from a valence band to be promoted to the same shell in the conduction band, i.e. $s-s, p-p, d-d$ etc. (although an $s-d$ transition is weakly allowed.) These selection rules may be broken if the shells become mixed, for example in highly unsymmetrical dots.

The conduction and valence bands in III-V semiconductor materials respectively originate from *atomic* s and p-electron energy levels. QD electrons retain an atomic s-type wavefunction, with angular momentum, $l^{\mathrm{e}} = 0$. The total angular momentum projection in the z-direction (optical axis) of the electron is therefore given by its spin quantum number, defined as $s_z^{\mathrm{e}} = 1/2$. Two spin projections along z are possible for the electron, with $m_{s,z}^{\mathrm{e}} = \pm 1/2$. The hole wavefunction is predominantly p-type in character, with the orbital angular momentum, $l^{\mathrm{h}} = 1$. Two possible combinations for the total angular momentum result, these are labelled $j_z^{\mathrm{h}} = 3/2$ and $j_z^{\mathrm{h}} = 1/2$. The latter are split-off in energy and are usually not taken into account for QD transitions. Heavy holes ($m_{j,z}^{\mathrm{hh}} = \pm 3/2$) and light holes ($m_{j,z}^{\mathrm{lh}} = \pm 1/2$) in the valence band are degenerate in bulk semiconductors, but become split in confined systems such as quantum wells, due to the difference in confinement energy. The splitting is increased when the confinement is three-dimensional due to the strain in the QD, reaching values >10 meV. This splitting means that the light holes are usually neglected when considering the ground-state exciton transitions (although recently, light hole-excitons can be investigated [21]). If the dot shape is anisotropic [22] or, for example an in-plane magnetic field is applied [23], light hole-heavy hole mixing may occur, changing the optical selection rules so that transitions become elliptically polarized.

Bright and dark excitons

The confinement potential is stronger than the electron-hole Coulomb interaction, which acts as a small perturbation to the energy of a bound electron-hole pair (exciton binding energy). An electron and hole, which are both in their respective s-shells are bound together to form the ground-state exciton, which can have possible spin values: $S_z = m_{j,z}^{\mathrm{h}} + m_{s,z}^{\mathrm{e}} = -2, -1, +1, +2$. As the absorption of a single photon can only impart a change in angular momentum of ± 1, bright excitons with $S_z = \pm 1$ are

optically allowed. Dark exciton states with $S_z = \pm 2$ are optically forbidden due to the conservation of angular momentum. Fig. 2.2 shows the s and p energy levels of the QD, each filled with electrons or holes. The bright ground-state excitons are highlighted.

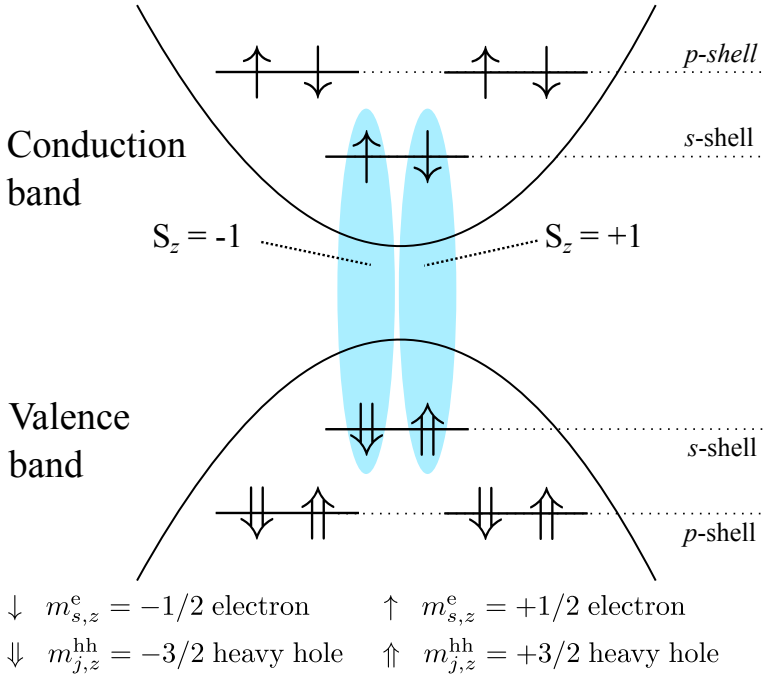

Figure 2.2: The s and p-shells in the conduction and valance bands for the QD. Each shell is twofold spin degenerate, as indicated by the up and down arrows. Blue highlights indicate the two ground-state bright excitons, $X_{\Downarrow\uparrow}$ and $X_{\Uparrow\downarrow}$. Light holes have been neglected for this diagram.

The composition of the QD is not uniform, due to the intermixing of gallium. The indium content of QDs grown under similar conditions as those studied in this work have been shown to have a vertical gradient from the top of the structure [24]. The hole wavefunction is confined to the top, where the indium content is high, and the electron wavefunction is located towards the bottom. Since the electron and hole are vertically aligned, the dots typically possess a strong permanent electric dipole moment.

Fine structure

If the QD is asymmetric in the $x-y$ plane, the electron-hole exchange interaction couples the bright exciton states, giving rise to eigenstates that are linearly polarized along the in-plane crystal axes [110] and [$\bar{1}$10] (x and y axes, respectively), described by the wavefunctions in eq. (2.1), which are formed as linear superpositions of circularly polarized bright excitons. The fine-structure split states are shown in fig. 2.3 (a).

$$\begin{aligned}\psi_x &= \frac{1}{\sqrt{2}}(|\Uparrow\downarrow\rangle + |\Downarrow\uparrow\rangle) \\ \psi_y &= \frac{1}{\sqrt{2}}(|\Uparrow\downarrow\rangle - |\Downarrow\uparrow\rangle)\end{aligned} \tag{2.1}$$

A fine-structure splitting ($\hbar\delta$) with magnitude 0-500 μeV is typically observed between the bright linear eigenstates. For fully symmetric QDs, $\hbar\delta$ is zero, but for elongated QDs the difference in confinement energy in the x and y directions increases the value of $\hbar\delta$. The fine-structure splitting has been shown to be dependent on the size of the QD [25].

Biexciton complexes

As both the conduction and valance band s-shells can be occupied by two spin-degenerate carriers, nothing prevents the two exciton states from being present at the same time, forming a biexciton complex ($2X$). Coulomb interactions between the two excitons mean that a biexciton binding energy (E_{2X}) modifies the $2X$ transition energy from simply being twice the energy of X. Fig. 2.3 (a) shows the $|0\rangle - |X\rangle - |2X\rangle$ system in the QD, in the case where the excitons are created individually by a linearly polarized laser. If the transition is addressed, with circularly polarized light, and the laser bandwidth is greater than $\hbar\delta$, then the superpositions $|\Downarrow\uparrow\rangle$ and $|\Uparrow\downarrow\rangle$ are effectively degenerate and have energy $\hbar\omega_X$, as shown in fig. 2.3 (b). This condition can also be met if a highly symmetric QD is addressed with a narrowband laser. The $2X$ state can be now be created, by cross-circularly polarized pulses.

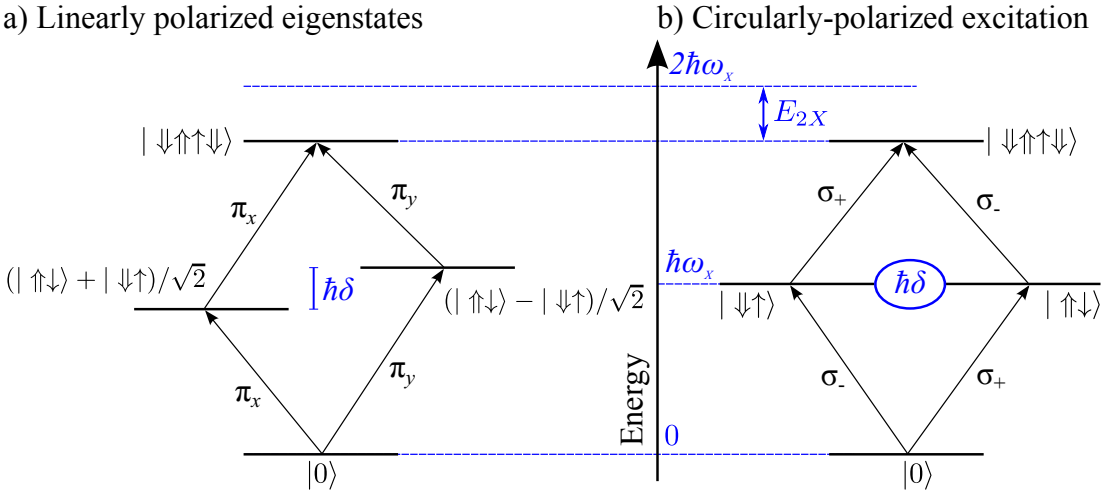

Figure 2.3: a) $|0\rangle - |X\rangle - |2X\rangle$ system showing fine-structure split exciton states. Arrows show the allowed linearly-polarized optical transitions. b) The circular polarization basis with laser pulsewidth $> \hbar\delta$ allows $X_{\Downarrow\uparrow}$ and $X_{\Uparrow\downarrow}$ to be addressed. Here $\hbar\delta$ acts as a small coherent coupling between the two states, indicated by the blue oval. $\hbar\omega_X$ is the exciton transition energy and E_{2X} is the biexciton binding energy. NB, the energy levels here are not to scale. In reality $\hbar\delta \ll E_{2X}$.

Factors such as strain and electric field have been shown to allow tuning of $\hbar\delta$, as well as a great deal of work growing QDs with $\hbar\delta$ close to zero. If $\hbar\delta$ is less than the radiative linewidth, a particularly interesting situation arises: the (linearly polarized) photons emitted in the biexciton cascade down to the crystal ground state are degenerate and can serve as a source of entangled photons [26, 27].

Application of a magnetic field

The application of a magnetic field splits the degenerate electron and hole spin states by the Zeeman effect. Typically, there are two configurations of magnetic field that are of particular interest. Firstly, if the field is applied in the growth direction of the sample, this is called the *Faraday* geometry. Secondly, if the magnetic field is applied in the plane of the sample then this is termed the *Voigt* geometry. These configurations of the magnetic field and the sample plane are shown in fig. 2.4.

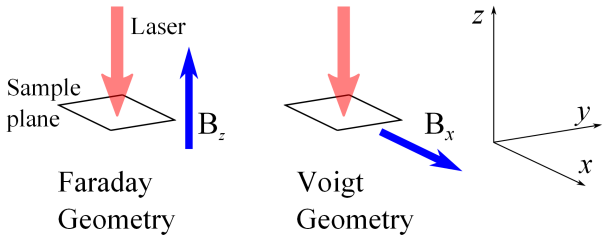

Figure 2.4: (a) A Faraday geometry magnetic field is applied to the sample, with the field direction parrallel to the sample growth direction. (b) In the Voigt geometry, the magnetic field is applied in the sample plane.

In the Faraday geometry the exciton spin states, $|\Uparrow\downarrow\rangle$ and $|\Downarrow\uparrow\rangle$ are split by the magnetic field as shown in fig. 2.5. The energy splitting between the two states is the Zeeman energy, given by eq. (2.2).

$$E_{\mathrm{Z}}^{i} = g^{i}\mu_{B}B, \tag{2.2}$$

where g^i is the g-factor for the species i (electron, heavy hole and exciton), μ_B is the Bohr magneton and B is the magnetic field strength. For simplicity, the hole spin ($m_j = 3/2$) is reduced to a *pseudospin* of value $1/2$ by including a factor of 3 in g^{h}. The exciton g-factor is given by $g^X = g^{\mathrm{h}} - g^{\mathrm{e}}$ and is found to be dependent on the QD size, typically taking values in the range $-2-1$ [28]. Schwan *et al* report the following values: $|g_z^{\mathrm{h}}| = 0.53$ and $|g_z^{\mathrm{e}}| = 0.60$ in a Faraday geometry B-field. When the field is strong enough for $E_{\mathrm{Z}}^{X} > \hbar\delta$, the exciton eigenstates for a QD with $\hbar\delta > 0$ become $|\Downarrow\uparrow\rangle$ and $|\Uparrow\downarrow\rangle$, with circularly polarized transitions, rather than the linear eigenstates given in eq. (2.1). A small spin-independent diamagnetic shift, proportional to B^2, also modifies the exciton energy [29].

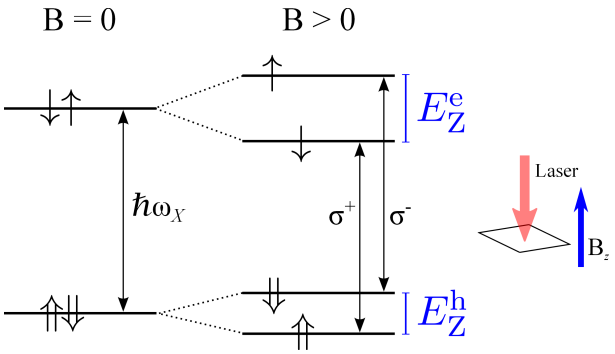

Figure 2.5: Zeeman splitting of electron and hole spin states with the application of a Faraday geometry magnetic field. Allowed optical transitions are shown, which are circularly polarized when the field is applied. The inset shows the orientation of the sample plane, laser and magnetic field.

In the Voigt geometry, the exciton eigenstates become less well defined as dark and bright states may become mixed [30]. Both g^{e} and g^{h} are anisotropic with respect to

the crystal axes, with g^{h} showing the largest anisotropy [31], with the magnitude of the g-factors becoming $|g_x^{\mathrm{h}}| = 0.08$ and $|g_y^{\mathrm{h}}| = 0.23$ for the hole, and $|g_x^{\mathrm{e}}| = 0.54$ and $|g_y^{\mathrm{e}}| = 0.52$. The Voigt geometry magnetic field configuration is of particular interest for single spin control schemes, as the Larmor precession about an in-plane field parallel to x is a Bloch sphere rotation about the x-axis, with angular frequency $\omega_{\mathrm{Z}_x} = E_{\mathrm{Z}_x}/\hbar$. Typically the precession is combined with an optically induced rotation (as discussed in § 2.5) to give full Bloch sphere control [32].

The relevant energy level schemes for spin control experiments are the spin-trion systems, which are shown in fig. 2.6. Here a singly charged QD is used so that a single spin can be isolated. Charged QDs can be grown by doping the QD during the MBE growth and neutral QDs can be charged either by voltage switching or by spin initialization techniques, as discussed in § 2.4.1. The electron (e), hole (h) and positive/negative trion ($X^{+/-}$) eigenstates in the Voigt geometry are aligned parallel ($|e_x\rangle$, $|h_x\rangle$ and $|X_x^{+/-}\rangle$) and anti-parallel ($|e_{\bar{x}}\rangle$, $|h_{\bar{x}}\rangle$ and $|X_{\bar{x}}^{+/-}\rangle$) with the in-plane B-field axis. The spin up or down states in the circular polarized basis are now superpositions of these eigenstates instead of the eigenstates in eq. (2.1). Each spin is coupled to both possible trion states via linearly polarized optical transitions, for example, the $|e_x\rangle - |X_x^-\rangle$ transition is allowed for π_x-polarized light.

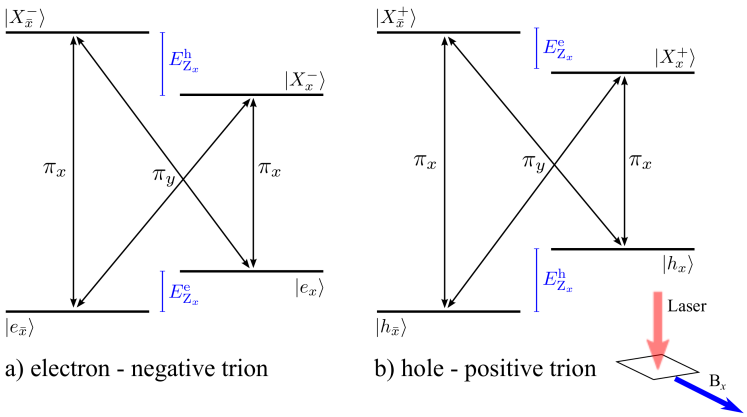

Figure 2.6: Charged QD electron (a) and hole (b)-trion energy levels in Voigt geometry. States are labelled (anti-)parallel to the in-plane B-field ($\bar{x}$)x. The inset shows the magnetic field orientation with respect to the the sample plane and laser.

DC Stark shift

If the QD is in the presence of a DC electric field, the confinement energy of the electron and hole is modified by the quantum-confined Stark effect (QCSE). They are pulled apart by the field and a red-shift in the exciton creation energy is experienced.

The QCSE is evident as a quadratic shift (ΔE_{Stark}) in exciton energy observed with increasing field strength, F, as described by eq. (2.3) [24].

$$\Delta E_{\text{Stark}} = pF + \beta F^2, \tag{2.3}$$

where p is the QD permanent dipole moment and β is the electric polarizability in the direction of the field. An example measurement of the Stark shift is presented later, in fig. 4.8 and discussed in § 4.4. A measurement of the DC Stark shift of the neutral exciton can be used to determine the average separation of the electron and hole in the dot [33]. In order to apply an electric field in the sample growth direction, diode structures are often fabricated onto the QD wafer [34–37]. Lateral field tuning can also be achieved, although in this case the field is applied perpendicular to the exciton permanent dipole so the QCSE is weaker. However lateral tuning can be used as a method for tuning the fine-structure [38, 39]

2.2 Optical control of a two-level system

Bloch sphere qubit notation

A qubit consisting of two coupled states, representing $|0\rangle$ and $|1\rangle$ can be schematically described by a Bloch sphere. The states $|0\rangle$ and $|1\rangle$ themselves, are the 'north' and 'south' poles of the sphere and any particular state can be described by the vector from the centre of the sphere. If the vector ends on the sphere surface, it defines a pure quantum state. However, if the vector is smaller than the sphere radius then a mixed state is indicated. Fig. 2.7 shows the Bloch sphere for a qubit. An arbitrary superposition state on the Bloch sphere can be described by coefficients in terms of the x, y and z axes: $x = 2\Re\langle c_0 c_1\rangle$, $y = 2\Im\langle c_0 c_1\rangle$ and $|z| = |c_1|^2 - |c_0|^2$. The population inversion of the system is equal to $-z$. The four states located on the equator of the sphere are the equal superpositions $\frac{1}{\sqrt{2}}(|0\rangle \pm |1\rangle)$ and $\frac{1}{\sqrt{2}}(|0\rangle \pm i|1\rangle)$. In the Bloch sphere picture, qubit gate operations are equivalent to rotations about the sphere of the state vector. Full coherent control of the system is achieved when any arbitrary vector can be rotated to any arbitrary position on the sphere.

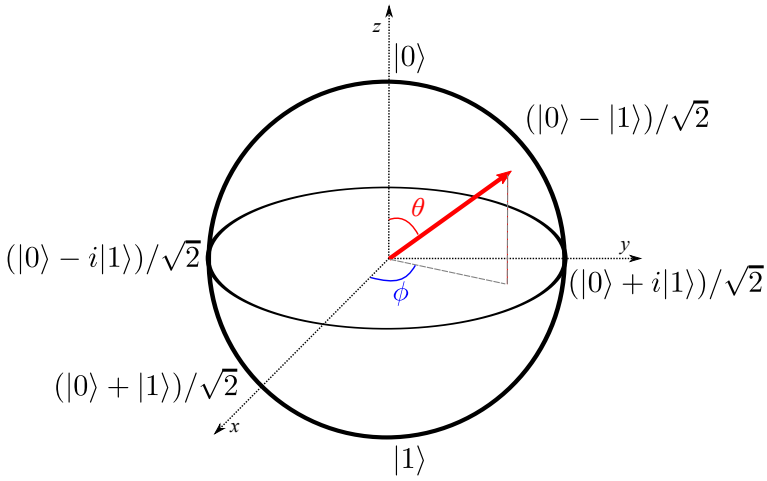

Figure 2.7: Bloch sphere diagram for a general qubit. An arbitrary Bloch vector is is defined by the angles θ and ϕ. The polar angle, θ determines the coefficients c_0 and c_1 from eq. (1.1). $c_0 = \sin(\theta/2)$ and $c_1 = e^{i\phi}\cos(\theta/2)$. Equal superpositions of $|0\rangle$ and $|1\rangle$, where $|c_0| = |c_1|$ lie on the equator and the phase of the superposition is given by the azimuthal angle, ϕ.

Rabi oscillations

Consider the qubit described in eq. (1.1). If the system is coupled strongly to a CW optical field (such that the interaction time is less than the coherence time), the system will undergo Rabi oscillations between the two states as a result of continuous absorption and stimulated emission. The probabilities that the system will be in either the ground state or the exciton state ($C_0(t) \equiv |c_0(t)|^2$ and $C_1(t) \equiv |c_1(t)|^2$, respectively) will oscillate with time, t, as follows:

$$C_0(t) = \cos^2(\Omega_R t/2) \tag{2.4a}$$

and

$$C_1(t) = \sin^2(\Omega_R t/2). \tag{2.4b}$$

The angular frequency of the oscillation between $|0\rangle$ and $|1\rangle$ is the Rabi frequency, Ω_R, as given by eq. (2.5):

$$\Omega_R = \frac{\mu_{01} E}{\hbar}, \tag{2.5}$$

where E is the (constant) electric field amplitude of the laser and μ_{01} is the optical dipole matrix element for the $|0\rangle - |1\rangle$ transition. For the QD $|0\rangle - |X\rangle$ transition, the value of μ_{0X} is approximately 75 D [40]. μ_{01} represents the strength of the coupling between the transition and the oscillating electric field of the laser. Fig. 2.8 shows the oscillation in the excited state population $C_1(t)$ with increasing pulse duration for undamped Rabi oscillations as a function of $\Omega_R t$ (black line). In reality, extending the time duration of the pulse has the effect that the oscillations are damped due to the finite coherence time of the excited state, as discussed in § 2.2. Strong and moderate

damping rates (γ) are used to calculate $C_1(t)$ according to eq. (2.6) [41]. These damped oscillations are also plotted in fig. 2.8 showing the effect of decoherence on the evolution of the system.

$$C_1(t) = \frac{1}{2(1+2\xi^2)}\left[1 - \left(\cos(\Omega' t) + \frac{3\xi}{(4-\xi^2)^{1/2}}\sin(\Omega' t)\right)\exp(-3\gamma t/2)\right], \tag{2.6}$$

where $\xi = \gamma/\Omega_R$ and $\Omega' = \Omega_R\sqrt{1-\xi^2/4}$.

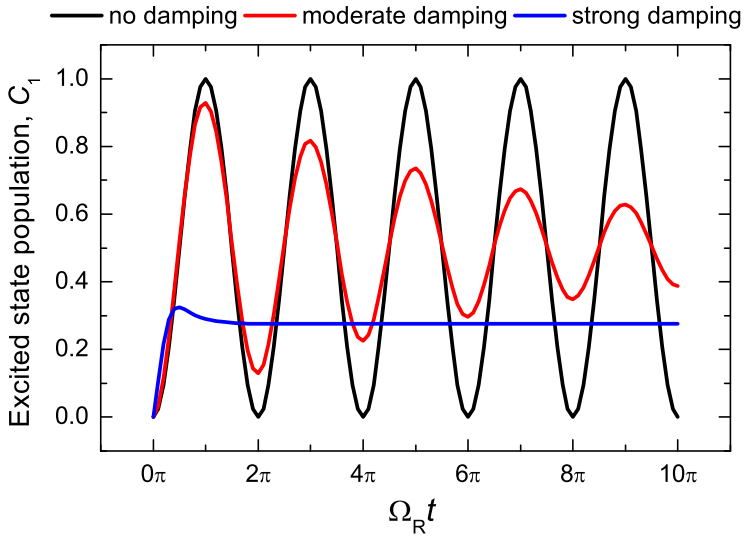

Figure 2.8: Rabi oscillations driven by CW excitation. In the ideal case of zero dephasing, the population inversion depends only on Ωt. If the damping rate γ is moderate *i.e.* $\gamma < \Omega_R$, oscillations with reduced amplitude may be observed. For strong damping, the excited state population for a given pulse reverts back to the weak-field limit, where $|C_0(t)|^2 \gg |C_1(t)|^2$, and the system never reaches a population inversion.

Pulsed excitation

Exciting the sample with a train of optical pulses allows time-resolved exciton dynamics to be studied following the inversion of the crystal ground state population. In this case, the time duration of the excitation pulse is fixed and the electric field amplitude varies according to the pulse-shape. At time t, the time-dependent Rabi frequency $\Omega_R(t)$ is given by:

$$\Omega_R(t) = \frac{\mu_{01}E(t)}{\hbar}, \tag{2.7}$$

where $E(t)$ is the instantaneous electric field amplitude, which for a Gaussian pulse shape (as used experimentally and discussed in § 3.3.2) is given by:

$$E(t) = E_0 \exp\left(-4\ln 2t^2/\Delta\tau^2\right), \tag{2.8}$$

where $\Delta\tau$ is the FWHM of the pulse in the time-domain and E_0 is the peak amplitude. The integral of the time-dependent Rabi frequency gives the pulse area, Θ:

$$\Theta(t) = \int_{-\infty}^{t} \Omega_{\mathrm{R}}(t')\,\mathrm{d}t', \tag{2.9}$$

a convenient quantity that defines the angle about the x-axis on the Bloch sphere through which the Bloch vector is rotated by the pulse and is equivalent to $\Omega_{\mathrm{R}}t$ in the CW case. The situation where the transition is addressed by a detuned laser is discussed in § 6.1.1. The peak Rabi frequency can be estimated by $\Omega_{\mathrm{R}}(0) \approx \Theta/\Delta\tau$. Optical pulses used to drive Rabi oscillations are conventionally named after their pulse area, for example, a pulse with $\Theta = \pi$ is referred to as a π-pulse. Several quantum logic gates require arbitrary rotation only about the x-axis, meaning that driving Rabi oscillations is an important experimental result. Specific examples of these include:

- The full inversion of the $|0\rangle$ and $|1\rangle$ populations when a π-pulse is absorbed, effectively a classical NOT gate.
- A $\frac{\pi}{2}$-pulse performs a Hadamard operation (of which there is no classical equivalent), which converts the $|0\rangle$ and $|1\rangle$ states into superpositions i.e. $\frac{1}{\sqrt{2}}(|0\rangle + i|1\rangle)$ when the $\frac{\pi}{2}$-pulse is absorbed by an empty QD.

Dephasing and coherence times

In reality, the qubit can never be a fully isolated system. Interactions with the environment cause a loss of coherence, resulting in a finite coherence time for performing a control operation. In practice, the need for high coherence necessitates the use of low-temperature experiments, which are usually carried out at liquid helium temperatures.

The coherence of a quantum state is usually described by two coherence times, T_1 and T_2, following the nuclear magnetic resonance conventions originally used by Bloch [42]. These describe two different mechanisms whereby information is lost about the superposition. Firstly, T_1 describes longitudinal decay of the quantum state, where the excited state $|1\rangle$ returns to the ground state $|0\rangle$. This process represents the lifetime for an initial population inversion and population is lost through the decay. Secondly, information can be lost about the phase of the superposition. Elastic collisions with the environment mean that although the energy of the excited state may not be changed (no change in population), the phase information (x and y components of the Bloch vector in fig. 2.7) becomes erased as shown in fig. 2.9 (b). This process called *pure* dephasing and occurs on the timescale T_2^*, leading to a mixed state where the state vector ends inside the Bloch sphere. Example sources of pure dephasing are atomic collisions in a gas, lattice vibrations in a solid and interactions with nuclear spins in QDs.

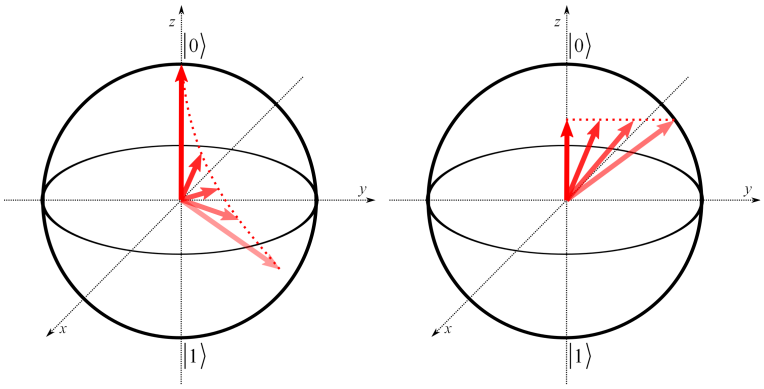

Figure 2.9: a) Longitudinal decay of the excited state population, in this case an arbitrary superposition decays back to the ground state $|0\rangle$. b) Transverse decay of the superposition, which becomes dephased after interactions with the environment, with no change to the population (z-axis component of the Bloch vector). In both cases the arrow with the highest transparency is the initial state, which decays to the solid colour arrow.

T_2 describes the total dephasing time of the system, including both population decay and pure dephasing, and is given by eq. (2.10). T_2 is the timescale where coherent manipulation of the Bloch vector is possible.

$$\frac{1}{T_2} = \frac{1}{2T_1} + \frac{1}{T_2^*} \tag{2.10}$$

The specific factors that determine the lifetimes and dephasing times of single excitons and spins in QDs are discussed respectively in § 2.6.1 and § 2.6.2.

2.3 Exciton and biexciton control

2.3.1 Exciton control

p-shell exciton control

The exciton is the simplest possible optical excitation of the QD, making it the natural first choice for coherent control experiments. The first experimental control of a QD state was reported in 1998 by the ground-breaking work of Bonadeo *et al* [43]. Here, a stabilized Michelson interferometer was used to excite the QD with two successive pulses, separated by a time delay, τ. Each pulse generates a p-shell exciton population in the QD, with a relative phase between the exciton wavefunctions dependent on τ. Quantum interference is observed in the PL emission from the s-shell exciton, into which the excited p-shell exciton relaxes before radiatively recombining. Several other experiments have been carried out on p-shell excitons, including further wavepacket interference [44], evidence of driven Rabi oscillations [45–47], dephasing through phonon interactions and excitation induced dephasing [48, 49] and polarization control of the

fine structure-split exciton states [50]. Although *p*-shell excitons have been studied, relaxation into the *s*-shell is very fast due to the rapid emission of a phonon. *p*-shell excitons typically have short T_1 times of ∼40 ps.

Rabi oscillation and observation of Rabi-splitting

Several groups have reported the observation of Rabi oscillations from the crystal ground state to a single exciton [40, 45–47, 51–55]. Rabi oscillation is observable in the frequency domain, as the exciton transition become dressed by a pump laser. To remove the high-frequency carrier oscillation associated with the laser frequency, the rotating wave approximation is made. Firstly, if emission is observed for a state that is not directly coupled to the laser (a 'witness' state), for example in the $|0\rangle - |X\rangle - |2X\rangle$ system, a pump laser resonant with the $|X\rangle - |2X\rangle$ transition dresses the $|X\rangle$ and $|2X\rangle$ states, forming the ladder of dressed state pairs shown in fig. 2.10: $|\alpha_N\rangle$ and $|\beta_N\rangle$, where N is the number of photons in the laser mode. The dressed states are an admixture of $|X\rangle$ and $|2X\rangle$ and $|0\rangle$ is the witness state. Emission from the $0 - X$ transition can now be observed as a Autler-Townes doublet [45, 56–60], split by an effective Rabi energy $\hbar\Lambda$ (see § 6.1.1). The Autler-Townes transitions are shown in fig. 2.10(i). Secondly, if the emission is monitored from the dressed transition itself, four transitions become possible, as shown in fig. 2.10(ii). Two of these transitions are degenerate, having energy $\hbar\omega_X$. The other two transitions have energies $\hbar(\omega_X \pm \Lambda)$, resulting in a Mollow triplet (or just the observation of Rabi side-bands) [56, 61, 62]. Experiments using resonance fluorescence techniques allow the excitation laser to be filtered from the signal, and have observed the Rabi-split side-bands of the exciton transition.

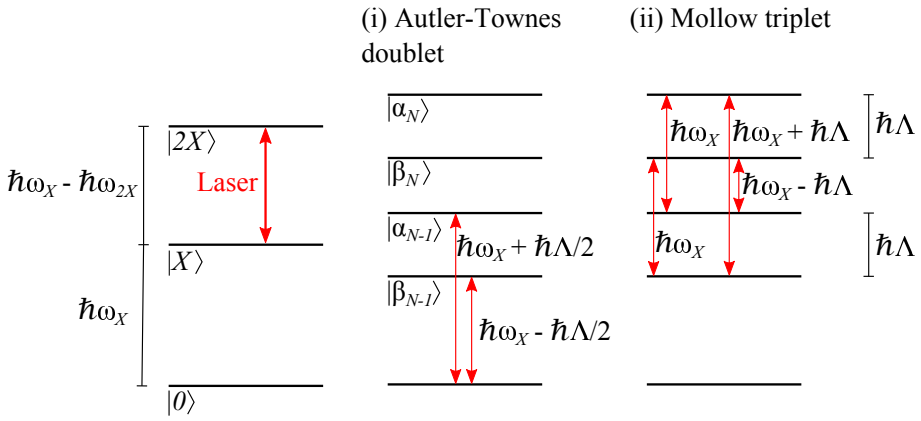

Figure 2.10: Level diagram for observation of Rabi-splitting. A pump laser dresses the $X-2X$ transition, forming a ladder of state pairs $|\alpha_N$ and β_N, where N is the number of photons in the laser mode. (i) Emission from the $0 - X$ transition is Rabi-split to form an Autler-Townes doublet. (ii) Four transitions are possible in the emission from $X - 2X$, of which two are degenerate, forming a Mollow triplet.

A complimentary experiment, carried out at Sheffield by Boyle [59] demonstrates the time-resolution of the $|X\rangle$ Autler-Townes doublet, by introducing a time-delay between the pump and probe laser. Beating between the dressed states is observed when the probe spectral width is increased sufficiently so that a superposition of the two dressed states is excited.

Ramsey interference

To achieve full coherent control, the Bloch vector must be rotated by arbitrary angles about two orthogonal axes. Driving a Rabi oscillation is one of these rotations, but for full control, this must be combined with an orthogonal rotation. Ramsey interference experiments can be carried out to measure the coherent precession of a superposition state about the z-axis [43, 46, 47, 63, 64]. The QD is excited by two $\frac{\pi}{2}$-pulses, separated by a time delay, τ_{delay}. The first pulse generating an equal superposition by rotating the Bloch-vector from $|0\rangle$ about the x-axis (fig. 2.11 (a)). The Bloch vector precesses in the $x-y$ plane, acquiring a delay-dependent phase $\phi = \omega\tau_{\text{delay}}$ (fig. 2.11 (b)). The axis of rotation is determined by ϕ, with (x, y, z) coordinates $(\cos(\phi), \sin(\phi), 0)$. Constructive (destructive) interference takes place when the phase is an integer, n, multiple of π. $\phi = 2n\pi$ ($\phi = 2(n+1)\pi$) and interference fringes are seen in the signal (fig. 2.11 (c,d)). Due to dephasing, the amplitude of the interference pattern decays with τ_{delay} and the extrinsic dephasing time (T_2) can be extracted.

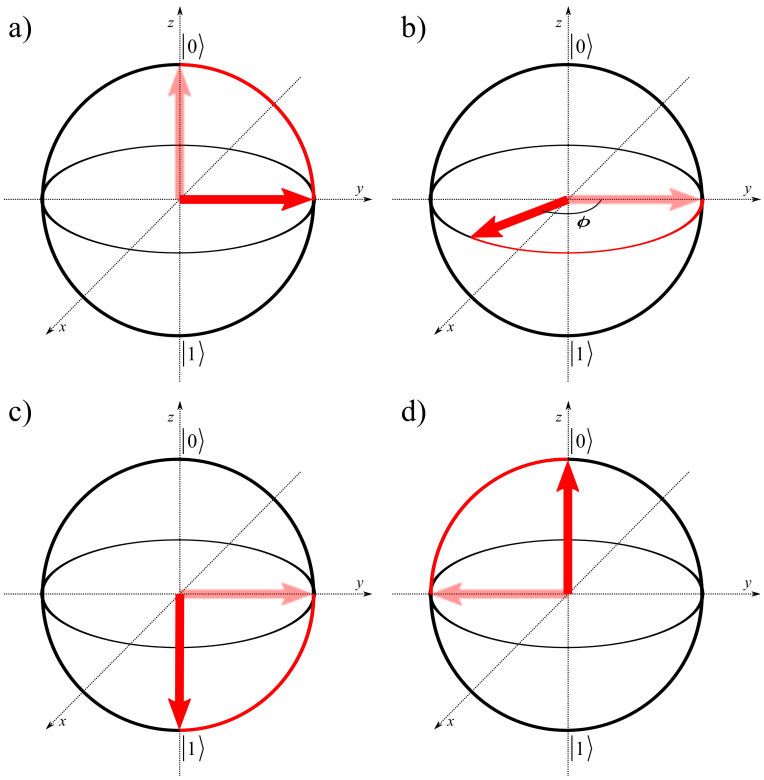

Figure 2.11: Ramsey interference experiment in the ideal case of zero dephasing. a) The qubit is initially in the $|0\rangle$ state (transparent arrow), absorption of the first $\frac{\pi}{2}$-pulse creates the superposition: $\frac{1}{\sqrt{2}}(|0\rangle + i|1\rangle)$ (solid arrow). b) The Bloch vector precesses in the $x-y$ plane. c) Constructive interference is observed if $\phi = 2n\pi$ and the vector rotates to $|1\rangle$. d) Destructive interference occurs if $\phi = (2n+1)\pi$ and the vector is returned to $|0\rangle$.

In work by Stufler *et al* [65], Ramsey fringes were observed in the photocurrent signal as a function of QD detuning from the laser, which was controlled by the reverse bias applied to the sample via the DC Stark-shift. Detuning the dot has the effect of changing the phase-shift for a fixed value of τ_{delay} as the coherent QD polarization no longer oscillates in-phase with the laser, as would be the case on resonance.

Control of fine-structure superpositions

The fine structure-split exciton eigenstates ψ_x and ψ_y, described in eq. (2.1), can themselves constitute the basis states for a qubit [66]. In these schemes, advantage is taken of the polarization selectivity of exciton states and a Bloch sphere is constructed from the different polarization states, mapping directly onto the Poincaré sphere. $\psi_{x(y)}$ represents an exciton linearly polarized along the major (minor) axis of the QD, accessible via linear polarization. These two states are aligned with the z-axis; diagonally polarized superpositions are aligned along x, and circularly polarized transitions along y. When the exciton is initialized into a superposition, the state vector precesses about z, with angular frequency δ. In order to control the exciton, a second pulse is used to

rotate the Bloch vector by performing a geometric phase operation [67, 68]. The axis of rotation is determined by the control polarization and the angle through which the rotation is performed is determined by the control detuning. A similar experiment was recently carried out by Müller *et al*, where the control pulse itself was resonant with $|0\rangle - |X\rangle$ [69].

2.3.2 Biexciton control

Conditional Rabi rotation

The exciton-biexciton system in a QD provides a opportunity to study a system that contains two-qubits in the same nanostructure. As the dot can contain two excitons of opposite spin, either can be accessed independently. Fig. 2.3 (a) shows the 4-level system involved. In total, there are four linearly-polarized transitions, two of which are between the fine-structure-split X states and $|2X\rangle$. These two transitions are conditional on the presence of the neutral exciton in the dot making a conditional Rabi rotation from $|X\rangle$ to $|2X\rangle$ possible, equivalent to a CROT (conditional rotation) gate operation. These experiments were first carried out for a GaAs interface dot [70] and in later work at Sheffield by Boyle for SK QDs [71]. Here, if an initial π-pulse is resonant with the $|0\rangle - |X\rangle$ transition, a second pulse, resonant with $|X\rangle - |2X\rangle$, is only absorbed if it is CO-linearly polarized with the first.

Coherent two-photon absorption

It is also possible to directly access the biexciton from the crystal ground state by using a two-photon absorption process [72]. Here, the sample is excited with a linearly polarized pulse with energy $\hbar\omega_X + E_{2X}/2$, where E_{2X} is the biexciton binding energy, as defined in fig. 2.3. Coherent coupling of two single-photon transitions (both slightly detuned from the laser) occurs, enabling the creation of the biexciton. In this case, the rotation is between a superposition of $|0\rangle$ and $|2X\rangle$, not $|X\rangle$ and $|2X\rangle$ as before, and can be seen as an entangling operation. The use of an interferometer allows the observation of Ramsey fringes in the biexciton signal. The oscillations are at twice the laser frequency as is characteristic of a two-photon process [72, 73].

2.4 Single spin control

Single carriers are potentially more suitable for use as qubits than excitons due to them having longer coherence times. Single-spin experiments are more complicated than exciton control schemes for two reasons. Firstly, unlike the exciton, a single spin cannot be initialized simply as a result of the absorption of a photon, since measures have to be taken to remove the other photo-generated carrier. Secondly, the spin-states electron (hole) $|\downarrow\rangle$ and $|\uparrow\rangle$ ($|\Downarrow\rangle$ and $|\Uparrow\rangle$) are degenerate in the absence of

a magnetic field, meaning that in order to observe spin precession, a magnetic field has to be applied. The first report of single-spin control was by Press *et al* [74], who demonstrated full control of the electron spin on the Bloch sphere. Here at Sheffield, we have recently investigated the coherent control of a single heavy hole in the QD [32]. Details of the spin control experiments that different groups have implemented are discussed in § 2.5.

2.4.1 Spin initialization

Optical pumping

Optical pumping can be used to initialize the spin with an extremely high fidelity [75]. This scheme requires samples that include a doped layer in addition to the QD layer to ensure that singly-charged QDs are the result. QDs can also be charged by changing the reverse bias applied to a QD in a diode structure. A charged exciton (positive or negative trion) is generated if a photon is absorbed. Fig. 2.12 (a) shows the energy level diagram for the electron and negative-trion system in the absence of a magnetic field.

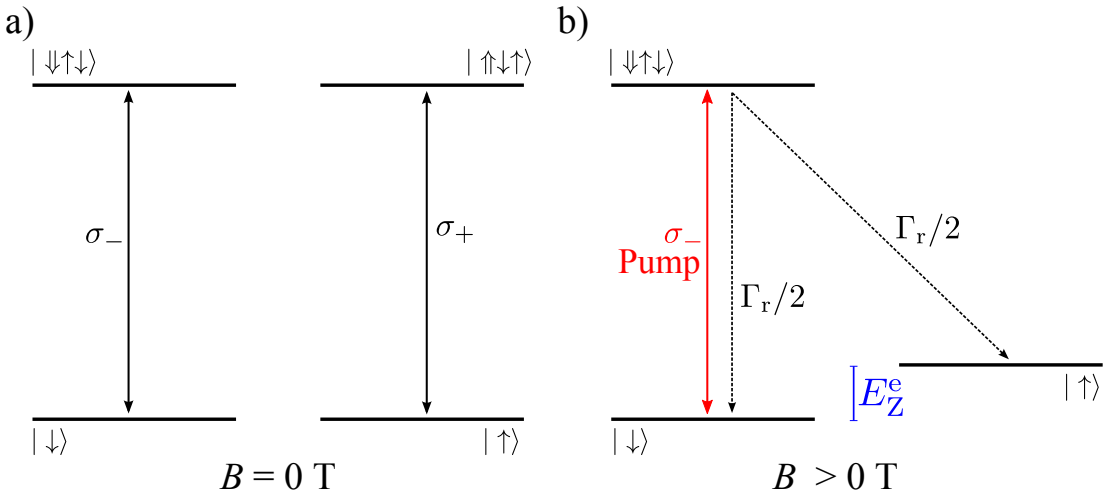

Figure 2.12: a) Electron-trion system energy levels with allowed circularly polarized transitions. b) Spin pumping scheme for electron initialization (with $B > 0$), Γ_r is the trion radiative recombination rate. Here the electron is initialized into the $|\uparrow\rangle$ state. Spin flipping between $|\uparrow\rangle$ and $|\downarrow\rangle$ reduces the spin preparation fidelity, unless a Faraday geometry B-field is applied.

Spin pumping relies on addressing one of the allowed optical transitions with a constant pump, in this case $|\downarrow\rangle - |\Downarrow\uparrow\downarrow\rangle$. Once the trion population is generated, it decays either radiatively or via a unidirectional Raman scattering process (which is much weaker than radiative recombination) into both electron spin states with an equal probability as shown in fig. 2.12 (b). This works because the radiative transitions are linearly polarized. If the trion recombines back to the $|\downarrow\rangle$ state then the electron is

recycled back into the trion by the pump laser. Spin-flip transitions between $|\uparrow\rangle$ and $|\downarrow\rangle$ are weakly allowed via the electron-nuclear hyperfine interaction. This effectively erases the initialized state, a problem that is overcome by the application of a Faraday geometry magnetic field. The field splits the electron spin-states by the electron Zeeman energy Z_Z^e, suppressing spin-flip events due to incompatible electron and nuclear Zeeman energies [76, 77]. The spin pumping scheme can be modified so that a Voigt geometry magnetic field is applied to the sample, as is required for spin precession measurements. Here, the increased light hole-heavy hole mixing due to the in-plane field results in faster spin initialization, with only a small loss of fidelity [74, 78].

A similar scheme can be used to initialize a single hole spin [79], which does not require a B-field for high-fidelity preparation due to the reduced hole-nuclear hyperfine interaction.

Coherent population trapping

Despite the impressive spin preparation fidelities that are achievable with spin pumping schemes, it is only possible to initialize the spin in one of the eigenstates of the system, and not an arbitrary superposition. Spin pumping also takes a relatively long time (> 1 ns) as many cycles have to be performed. In order to get past these limitations, a coherent population trapping (CPT) technique can be employed for initializing electrons [80] and holes [81]. Here, a Λ-transition is extracted from the electron-trion system for a singly-charged QD in a Voigt geometry magnetic field (fig. 2.6 (a)) by frequency selectivity. The resulting Λ-transition is shown in fig. 2.13.

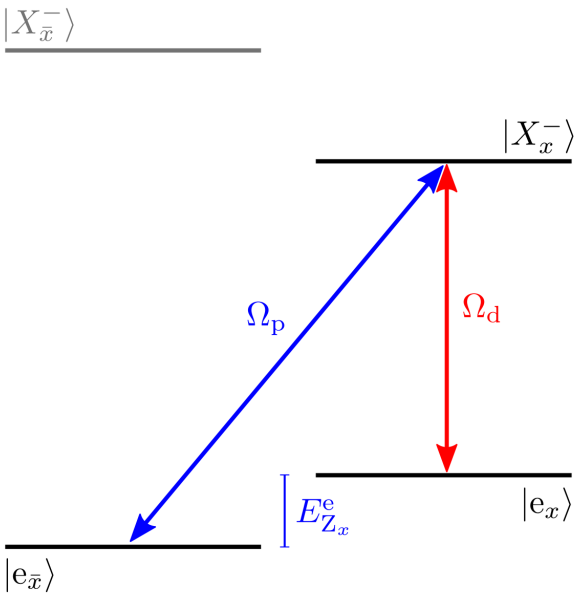

Figure 2.13: Electron-trion transition used for CPT experiments. A Λ-transition is constructed from the two electron levels and the lowest energy trion states.

Two CW lasers are used in this scheme, a driving laser resonant with $|e_{\bar{x}}\rangle - |X^-_{\bar{x}}\rangle$, and a probe laser, the energy of which is scanned through the $|e_x\rangle - |X^-_{\bar{x}}\rangle$ transition. The Rabi frequencies of the two lasers are Ω_d and Ω_p, respectively. When the probe laser is exactly on resonance with the transition a two-photon absorption process means that a 'dark' state is formed, evident as a dip in the probe absorption spectrum. The dark state is a superposition of the exciton eigenstates: $\psi = (\Omega_d|x\rangle - \Omega_p|\bar{x}\rangle)/\sqrt{\Omega_d^2 + \Omega_p^2}$ with no population remaining in the trion state. By varying the relative intensities of the lasers, any arbitrary superposition may be prepared.

Exciton ionization

If a diode structure has been fabricated on to the QD sample then it is possible to ionize the exciton by allowing only one electrical carrier to tunnel away from the dot by making use of a difference in the electron and hole tunnelling rates [77,82]. This method has the advantage over both optical pumping and CPT as it can be performed on a neutral QD, without having to initially charge the dot. Since holes have a larger effective mass than electrons, they are well suited to this technique as they have a longer tunnelling time than electrons. To enhance the tunneling difference, an additional tunnelling barrier (for example a layer of AlGaAs) can be included in the structure to reduce the hole tunneling rate. With the application of an electric field accross the sample, the electron tunnelling time can be faster than ∼50 ps, resulting in an ultrafast initialization that is faster than the other techniques. Circular-polarized excitation is used to prepare an exciton with a well-defined spin. In order to impart the hole with the original exciton spin, the electron tunnelling time has to be faster than the neutral exciton fine-structure precession period, otherwise the hole spin would be randomized due to the exciton precession before the electron tunnels. Application of a Faraday-geometry magnetic field improves the spin preparation fidelity [82] (∼99% can be achieved with B ∼2 T) as the Zeeman splitting between the exciton spin-states becomes larger than the fine-structure splitting of the linear exciton eigenstates without a field, ensuring that the exciton remains in a well-defined spin state for a longer time. As the fast initialization is compatible with the diode being under reverse bias, exciton ionization is the preferred method for spin preparation in photocurrent detection schemes. Recent preliminary measurements are featured in Appendix C, demonstrating the potential for near-unity hole spin preparation in the absence of a magnetic field when $\hbar\delta$ is close to zero. At the time of writing this thesis, further measurements are being carried out in order to fully characterize the high-fidelity preparation of the hole spin.

Hole spin control schemes require the B-field to be applied in Voigt-geometry, the hole spin preparation fidelity is limited to 75% by the dynamics of the exciton spin, as studied previously by Godden and myself *et al* [83] for a single QD. In the presence of the electron, the hole is modelled as having a rotating and counter-rotating phase

factor with respect to the exciton fine-structure precession. Optimal preparation occurs when $\hbar\delta \approx E^{\mathrm{h}}_{\mathrm{Z}_x}$: the rotating component is synchronised with the Larmor precession. However, the counter-rotating component is dephased. Preparation fidelities greater than 96% have been demonstrated for a double QD system, as advantage can be taken of the fast (5 ps) electron tunneling into the vacant QD electron level [84].

2.5 Spin control schemes

2.5.1 Optical gate operations

Stimulated Raman transition/optical Stark shift

Consider the electron and trion energy level scheme in Voigt geometry shown in fig. 2.6 (a). There is no allowed optical transition between the two electron states $|\mathrm{e}_x\rangle$ and $|\mathrm{e}_{\bar{x}}\rangle$. However, both of these states couple to both trion states $|X^-_x\rangle$ and $|X^-_{\bar{x}}\rangle$, via linearly polarized transitions. This means that two independent Λ-transitions can be constructed, each with $|\mathrm{e}_x\rangle$ and $|\mathrm{e}_{\bar{x}}\rangle$ coupling to one trion level. Each transition has a Rabi frequency: $\Omega_{x(y)} = \frac{\mu_0 E_{x(y)}}{\hbar}$ where $\Omega_{x(y)}$ refers to the $x(y)$-polarized transition and $E_{x(y)}$ is the electric field amplitude in the $x(y)$ direction. The system is addressed by a control pulse to change the phase of the electron spin superposition. A circularly polarized control pulse ensures that the probability amplitudes from both Λ-transitions add. The trion population is kept at a minimum by detuning the control pulse away from the transitions by Δ, such that $\Omega_x \ll \Delta$ and $\Omega_y \ll \Delta$, ensuring that the pulse is absorbed but that the trion levels are adiabatically eliminated [85]. The pulse therefore drives a Rabi oscillation between $|\mathrm{e}_x\rangle$ and $|\mathrm{e}_{\bar{x}}\rangle$, with effective Rabi frequency $\Omega_{x\bar{x}} \approx \Omega_x\Omega_y/\Delta$. In the work in ref. 74, a stimulated Raman transition is the rotation about the first axis on the Bloch sphere, and Larmor precession of the electron spin about the in-plane magnetic field is the second, orthogonal rotation.

An equivalent interpretation of the action of a detuned laser pulse is in terms of an optical, or AC, Stark effect (OSE), as used in experiments by Berezovsky *et al* [86]. In this picture, the circularly-polarized control pulse excites only one of the $|\downarrow\rangle - |\Downarrow\uparrow\downarrow\rangle$ and $|\uparrow\rangle - |\Uparrow\downarrow\uparrow\rangle$ transitions, resulting in an energy shift of that spin sublevel. The splitting can be understood to be an effective magnetic field, B_{Stark}, in the direction of the laser propagation (z axis on the Bloch sphere) about which the electron spin precesses. The phase change due to the OSE is related to the intensity and detuning by eq. (2.11) [87]

$$\phi_z \propto \frac{\mu_0^2 I}{2\Delta}\tau, \tag{2.11}$$

where I is the intensity of the control pulse and τ the time-duration of the pulse.

Geometric phase control

Prior to the experiments that are presented here, work by Godden and myself *et al* [32] demonstrated the use of a geometric phase to coherently control a single hole spin. The technique is similar to the methods used in the exciton control schemes in § 2.3.1. After the hole is initialized into $|\Uparrow\rangle$ or $|\Downarrow\rangle$, via exciton ionization, it is then free to precess about the Voigt geometry magnetic field axis (x). The control pulse is circularly polarized and has a bandwidth, $\Delta E_{\text{control}}$ which is larger than both the electron and hole in-plane Zeeman energies. The control pulse is resonant with the hole-positive trion transition, reducing the 4-level system in fig. 2.6 (b) to the two coupled 2-level systems in fig. 2.14, with each hole spin state coupled to a corresponding trion.

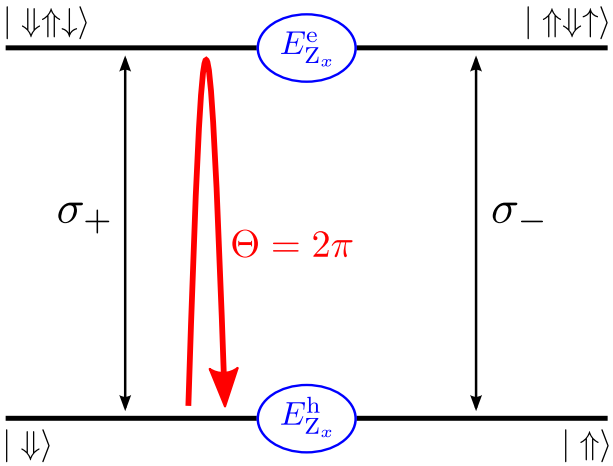

Figure 2.14: Hole and positive trion levels in Voigt geometry in circular polarization basis. The control laser pulse has bandwidth: $\Delta E_{\text{control}} > E_{\mathrm{Z}_x\mathrm{h}}, E_{\mathrm{Z}_x\mathrm{e}}$. The control pulse drives a 2π Rabi rotation, imparting a geometric phase on the hole superposition.

Before the control pulse arrives, the hole is in a superposition, described by $|\psi\rangle = h_{\Uparrow}|\Uparrow\rangle + h_{\Downarrow}|\Downarrow\rangle$. A σ_+ polarized control-pulse addresses only the $|\Downarrow\rangle - |\Downarrow\Uparrow\downarrow\rangle$ transition, driving a Rabi oscillation between the two states such that $|\psi\rangle \rightarrow h_{\Uparrow}|\Uparrow\rangle + h_{\Downarrow}(\cos(\Theta/2)|\Downarrow\rangle + i\sin(\Theta/2)|\Downarrow\Uparrow\downarrow\rangle)$. If $\Theta = 2\pi$ then the system is returned to the hole subspace, and a phase shift of π is acquired (equivalent to a rotation about the optical axis (z)). Control over the phase shift (ϕ_z) is achieved by detuning the control pulse, by $\hbar\Delta_{\text{control}}$ [67, 68], as described in eq. (2.12).

$$\phi_z = 2\arctan\left(\frac{\Delta E_{\text{control}}}{\hbar\Delta_{\text{control}}}\right), \tag{2.12}$$

2.5.2 Coupled-dot spin control schemes

Several QD layers can be deposited on the same substrate sample. If the layer spacing is small enough then the strain field from the first layer is experienced by the second, and so on, making the random locations of the QDs in the first layer preferable for the

nucleation of subsequent layers. Stacks of vertically aligned QD layers can therefore be grown [88]. The second layer of dots also have a similar size to the first, leading to similar confinement energies. The spacing between vertical dots can be tailored to be small enough for tunnelling to occur between two QDs, which as discussed in § 2.4.1 can be beneficial for single spin preparation by exciton ionization. Two dots, which are coupled together in this way are known as a QD molecule. Spins isolated on either of the dots can be coupled to the other QD and exciton or trion states can also be formed from carriers spread across the two dots.

Typically the application of a vertical electric field is used to tune the different QD molecule states, allowing switching between electronic states simply by moving to a different voltage.

Coupled dot systems provide a system for entangling electron spins, which are isolated on the two different dots [89]. In experiments by Greilich *et al* [90] optical control of one or two hole spin is demonstrated. Here, the diode structure is $p-i-$Schottky, allowing holes to be added one at a time to the dots. Single hole spin control is possible when one of the QDs is filled with two holes of opposite spin; interactions with a single hole in the other QD are supressed, essentially removing the influence of the second dot. When one hole occupies each QD, the two hole spins interact with each other to form a system of two coupled qubits, an important first step towards scalable qubit registers.

2.6 Decoherence of QD states

One of the main limitations to using QDs as qubits is the decoherence of the quantum states that are being manipulated, essentially limiting the number of coherent gate operations that can be performed. Single QDs never exist as a completely isolated system, as they constantly interact with the solid state environment of the semiconductor crystal. Effects such as lattice vibrations, fluctuating electric fields, heavy-light hole mixing and interactions with the ∼50,000 nuclear spins in the dot all cause decoherence.

2.6.1 Exciton dephasing

Exciton lifetimes, T_1^X

At cryogenic temperatures, which are necessary for electronic confinement in QDs, coherent exciton states are limited by the lifetime of the exciton (T_1^X), which is often dependent on carrier recombination, either by photon emission or non-radiative recombination, or for p-shell excitons, relaxation into lower-energy states. Radiative recombination typically occurs on a time scale of 400 - 1200 ps [91,92], setting a maximum value for T_1^X. In the photocurrent regime used here, exciton lifetimes are limited by the fast electron tunneling. This can be overcome by introducing a thicker barrier

for the electron, however the photocurrent detection efficiency is decreased as a result. In the work presented here in chapter 5, this compromise is overcome by modulating the bias voltage applied to the QD with a sinusoidal voltage.

Rabi rotation intensity damping

Damping is observed in the Rabi oscillations for neutral excitons in QDs where pulsed excitation is used to perform the rotation. Since the pulse area is proportional to the square root of the excitation power (as described in eq. (2.5) and eq.(2.9)), the damping of the Rabi oscillations depends on the intensity of the excitation pulse. Since the time duration of the pulse remains constant, the damping is notably different from the CW driving case; here, the coherence time is effectively decreased at higher laser intensities. The damping means that a full population inversion is never achieved as the amplitude of a π-pulse rotation can never reach unity. If the QD is well coupled to the optical field, then only a small intenstiy is required for a π-pulse, maximizing the possible inversion and the Rabi rotation amplitude can reach ~ 0.97.

The intensity damping has been extensively studied by the Sheffield Coherent Control group, particularly by Ramsay *et al* [93–95]. For ground state *s*-shell excitons, the main source of dephasing has been shown to be the interaction with longitudinal acoustic phonons propagating through the lattice, with increased damping evident at higher temperatures [93, 94]. A brief explanation of the underlying mechanism is that the electronic state of the QD is modulated at the Rabi frequency of the laser. Phonons are modelled as a bath of bosons that interact with the QD exciton via the deformation potential. Any phonons that are resonant with the effective Rabi frequency (as given in eq. (6.9)) allow a pathway for the exchange of energy between the QD and the phonon bath, at a rate that is a function of the effective Rabi frequency. A detailed model is presented in § 6.1.2. The loss of phase information from the phonon phase-space results in pure dephasing of the exciton superposition and as shown in ref 94, is accompanied by a shift in the Rabi frequency, induced by fluctuations in the phonon bath. The results presented in Chapter 6 extend the previous understanding of the exciton-phonon interaction by investigating the case where the phonon sideband itself is driven by a strong optical pulse, resulting in an excitonic population inversion.

2.6.2 Single-spin dephasing

Single spin lifetimes: T_1^{e} and T_1^{h}

In terms of coherent lifetimes, single spins have the advantage over excitons that they cannot radiatively recombine without the presence of the opposite charge carrier. Instead, the lifetime of single spins is limited by the spin-relaxation time, or the carrier tunneling time for QDs in diode structures. The spin is rotated about the Bloch sphere due to the spin-orbit interaction [96], where the electron or hole spin is coupled to its

orbital angular momentum. An electron moving in an electric field, **E** experiences an effective B-field, proportional to $\mathbf{E} \times \mathbf{p}$, where **p** is the momentum of the electron. In semiconductors, electric fields can originate from charged atoms in the lattice, deformation and piezo-electric potentials associated with the propagation of phonons, asymmetry in the crystal structure and charge fluctuations from electrical contacts. An important characteristic is the spin-orbit length, l_{SO}, defined as the length that a spin must travel before the effective B-field causes a π rotation of the spin. In GaAs, l_{SO} is typically 1-10 μm [97]. As the largest dimension of the QD is much smaller than this length, the spin-orbit interaction is therefore very weak. Very long spin relaxation times for electrons (T_1^{e}) have been observed [77], with a lower limit of ∼20 ms. The spin relaxation of QD holes is less than for electrons, due to heavy hole-light hole mixing [98,99]. Despite this, large values for T_1^{h} of ∼270 μs [100] and ∼1 ms [79] have been reported.

Single spin pure dephasing: $T_2^{*\mathrm{e}}$ and $T_2^{*\mathrm{h}}$

Spin-orbit coupling does not contribute towards pure spin dephasing [101], even with the application of a magnetic field in either Faraday of Voigt geometry. The primary source of dephasing is the interaction of the spin with the QD nuclear spins via the hyperfine interaction. Two mechanisms lead to the loss of spin phase information. Firstly, the thousands of atomic nuclei present in the dot mean that the electron or hole experiences a constantly fluctuating magnetic field (Overhauser field). Secondly, spin flips may occur for electrons as the spin may be exchanged with a nuclear spin at a rate proportional to $|A_{\mathrm{hf}}|^2/E_{\mathrm{Z}}^e$, where A_{hf} is the hyperfine constant and E_e is the electron Zeeman energy. Spin flips reduce the spin relaxation time and act as a mechanism for polarizing the nuclear spins. Electron-nuclear spin flip flops typically occur on a timescale less than 1 ns [102]. Heavy hole spin flip flops are forbidden due to conservation of angular momentum [103] unless the strain in the QD plane is anisotropic, causing mixing of heavy-hole and light-hole states [104].

The main contribution to the hyperfine interaction for the electron is the *contact* part, which depends on the probability density for the wavefunction at the nucleus. For an electron, the s-type wavefunction means that there is a relatively high probability density at the nuclear lattice sites. Due to the p-type wavefunction of a hole, the contact part of the hyperfine interaction is suppressed as the wavefunction is zero at the nuclear lattice sites. However, as recently demonstrated [105,106], the hole hyperfine constant has been shown to be only an order of magnitude weaker than for the electron. For holes, the hyperfine interaction is understood to be Ising-like in character, with the fluctuating Overhauser field acting in the z-direction. The hyperfine interaction is not the only source of pure dephasing for single spin: quadrupole interactions act to dephase the nuclear spin, which in turn acts to dephase the electron spin. Checkovich *et al* have

recently shown that the additional strain in QDs compared to bulk semiconductors suppresses the quadrupole interactions [107], which is advantageous for QD spin-qubits.

Values for $T_2^{*\mathrm{h}}$ of 1.7 ns [108], 12-17 ns [32] and 20 ns [90] for single holes have been demonstrated. Typically measured values for single electron spins $T_2^{*\mathrm{e}}$ are lower than $T_2^{*\mathrm{h}}$: 1.7 ns [109] and 5.5 ns [86]. Brunner *et al* performed coherent population trapping experiments and obtained an exceptionally large value for $T_2^{*\mathrm{h}}$, with a minimum value of 100 ns, and 40% confidence that $T_2^{*\mathrm{h}}$ exceeds 1 μs [81]. Hole spin dephasing has been studied theoretically by Fischer [103], who calculates that longer ($\sim \mu$s) timescales are associated with an in-plane field and a shorter ($\sim$ns) time constant defines dephasing from an out of plane field. It is possible that in Brunner's work, the first of these values was measured.

One of the most attributed reasons for dephasing is that due to the sensitivity of the spin g-factors on electrical fields. For QDs in diode structures, fluctuating charge environments cause the Larmor precession frequency to be randomized. This is particularly problematic for QDs embedded in p-type electrical diode structures [90,108]. Although the spin is dephased by charge fluctuations, this is an example which does not result in a mixed state, unlike the pure dephasing in fig. 2.9 (b). Instead, the spin precesses at an unknown frequency about the magnetic field axis and the end of the state vector never leaves the surface of the sphere. This is known as *homogeneous* dephasing, and can be reversed by using a spin-echo technique, removing the effect of T_2^* for averaged measurements. The coherence time is then determined by $T_2 \approx 2T_1$ and the measured coherence decay gives a direct measurement of T_2. Single spin spin-echo measurements of $T_2^{\mathrm{e}} = 2.6$ μs [109] and $T_2^{\mathrm{h}} = 1.1$ μs [108] have been observed.

Chapter 3

Experimental methodology

3.1 Introduction

In this chapter, experimental methods that were used to obtain the results throughout this thesis will be discussed. In order to achieve coherent excitation of a single quantum dot, several technical challenges must first be overcome, requiring sophisticated techniques and an experimental set-up that is especially designed for highly stable measurements. Coherent quantum states can only exist where they are well-isolated from their environment as any interactions are potentially sources of decoherence. For this reason, the sample must be kept in a low temperature cryostat during experiments.

In the experiments present here, optical excitation is used to control the QD states on a timescale that is short compared with the T_2^* coherence times discussed in § 2.6. Multiple laser pulses are needed to perform time-resolved measurements, and the optical properties of each pulse must be accurately controlled. The signal is then read out electronically, by performing a photocurrent measurement, which requires the sample to be electrically connected to a low-noise, high-sensitivity measuring circuit. The sample also has to be fabricated with an array of sub-micrometer apertures, in order to eliminate the excitation of several QDs simultaneously by the laser.

3.1.1 The principle of photocurrent detection

Photocurrent (PC) detection is an important measurement technique for coherent control experiments, as it allows direct electrical measurement of the occupancy of a single QD. Photocurrent detection has been used to measure both exciton [51,54,65,110,111] and hole-spin states [32,84]. With the correct device structure, single electrons may also be investigated. Photocurrent measurement is compatible with optical cavities [112], and recently, QD avalanche photodiode structures have been demonstrated [113].

To illustrate the principle of photocurrent detection, fig. 3.1 depicts the excitation of a single QD in a Schottky diode structure with a laser. To avoid exciting other QDs in the wafer, an opaque shadow mask is fabricated onto the diode surface. Typically,

the shadow mask is ∼100 nm of aluminium. At this thickness, single dots are accessed through apertures in the shadow mask that are < 1 μm in diameter. In this scheme, the QD is located ∼220 nm below the top surface of the semi-transparent Schottky barrier layer. In GaAs, at 4.2 K, the wavelength corresponding to the energy of 1.3 eV is $\sim$ 300 nm, QDs are located in the near-field region of the aperture as the QD depth is below a single wavelength from the aperture.

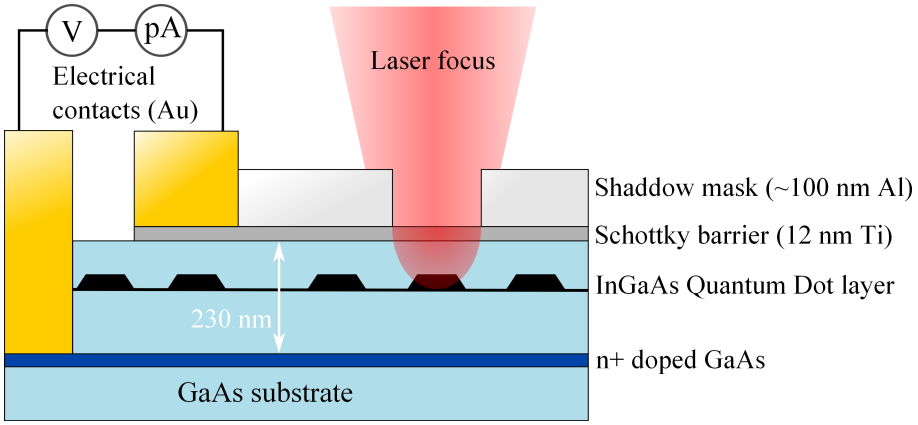

Figure 3.1: Photocurrent detection scheme for investigating single QDs. An excitation laser is brought to a focus on the surface of the sample. The intensity of the light is reduced by $\sim 10^5$ by the Al shadow mask, allowing the selection of a single QD by varying the laser energy. Electrical connections are made to the device contacts and the measuring circuit. When charge carriers tunnel out of the QD, a photocurrent is measured.

3.2 Sample details

3.2.1 Wafer structure

The sample is cleaved from the VN382 single-quantum dot wafer. This wafer was originally grown by H. Y. Liu and M. Hopkinson at the National Centre for III-V Technologies in Sheffield. The wafer structure is shown in fig. 3.2. The n^+ doped layer is used as a back electrical contact so that a diode can be fabricated vertically through the wafer layer structure, as shown in fig. 3.1. The nominal in-plane QD density is 30-60 μm^{-2}.

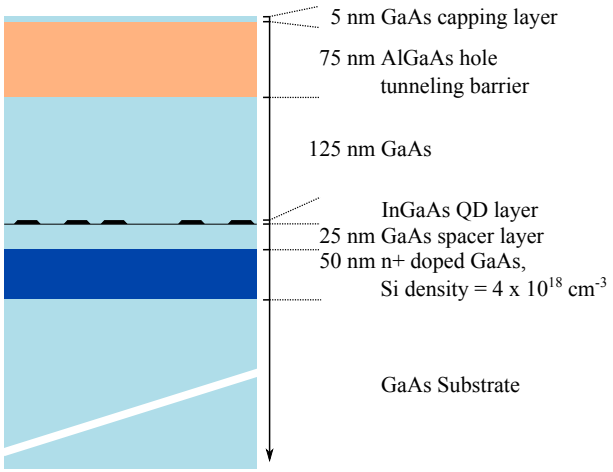

Figure 3.2: Schematic showing the VN382 wafer layer-structure. (Not to scale.)

3.2.2 Device fabrication

Schottky diodes

In order to connect to the measuring circuit, an array of Schottky diodes was fabricated on to the wafer. The diode properties have to be good enough to allow single-charge currents to be measured, the stringent technical specifications of the diodes will be discussed in § 3.4.3. The processing details for the diodes are summarized as follows:

1. *Wafer cleaving:* The wafer is cleaved along the [110] and [$\bar{1}$10] crystal axes. To ensure a high enough yield of diodes, the size of cleaved pieces was ∼1 cm × ∼1 cm, allowing the production of up to nine individual chips at a time.

2. *Ohmic contact definition:* An array of Ohmic contacts are defined on the wafer surface by UV photolithography. The contact pattern is then chemically etched down 230 nm into the wafer so that it reaches the doped layer.

3. *Ohmic contact evaporation:* The following sequence of metals are thermally evaporated onto the etched space to make the Ohmic contact: Ni (5 nm), AuGe (50 nm), Ni (50 nm), Au (200 nm).

4. *Thermal annealing:* Once the photoresist is removed from the sample surface with a solvent, the sample is baked at 380°C for 60 s to anneal the Ohmic contact. This promotes the diffusion of metal atoms into the doped layer to improve the electrical connection.

5. *Schottky contact definition and evaporation:* Again photolithography is used to define sixteen individual Schottky contacts. Each contact defines a mesa on the chip where the diode will be located. Two sizes of mesas are defined, large and small, having dimensions 340 μm × 390 μm, and 150 μm × 250 μm, respectively.

Eight of each sized mesa are defined on each common Ohmic contact. ∼12 nm of Ti is then evaporated onto the sample to form the semi-transparent Schottky contact on the semiconductor surface.

6. *Bond pad definition and evaporation:* A final photolithography step is used to define a bond pad directly onto the surface of the Ti Schottky contacts. 20 nm of Ti and 200 nm of Au are deposited to form the bond pad. The Ti layer promotes adhesion to the surface.

Apertures for single-dot spectroscopy

Once the diodes are fabricated, an I-V curves are measured for a representative number of diodes. If the yield of diodes with low noise and dark current is good, then single QD apertures are fabricated on the bare Ti contact, in a space surrounded by the Au bond pad. A micrograph of the surface of a finished chip is displayed in fig. 3.3. The following processing steps are carried out in order to fabricate the array of apertures.

1. *Aperture definition:* The apertures are typically too small to be resolved by visible light, necessitating the use of electron beam lithography to define an array of circular apertures on the Schottky contact. A *positive* resist is used for the aperture definition, resulting in solid pillars of resist (with height ∼1 μm) that will later be removed. A range of apertures sizes ranging from 200 nm to 1 μm in diameter are defined on the sample, ensuring that some of the apertures are correctly sized so that they allow access to individually resolvable QDs, even if there are errors in the aperture fabrication.

2. *Shadow mask definition and evaporation:* An opaque shadow mask is then defined on the area containing the aperture-pillars using UV lithography. 100 nm of Al is deposited. Aluminium was chosen for the shadow mask material in order to reduce the risk of Au diffusion into the GaAs, which reduces the diode quality.

3. *Aperture lift-off:* A solvent is then used to dissolve the pillars of resist, which leave behind an array of apertures in the Al mask.

4. *Final cleaving:* Individual chips are cleaved from the larger piece, each containing only one of the Ohmic-contact defined regions. Each chip is then labelled according to the processing batch and its position from the large piece.

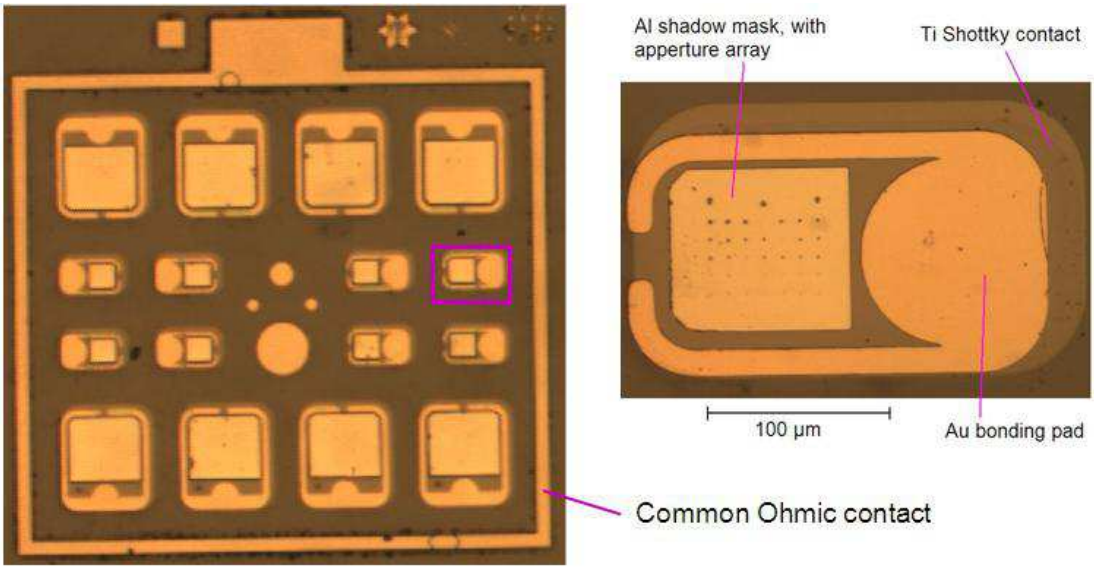

Figure 3.3: Micrograph of sample surface. The large image shows a single completed chip, as defined by one Ohmic contact. The circular features in the centre are Au markers. The close-up shows a single small mesa, including the Al shadow mask and aperture array. In this orientation the apertures are decreasing in size from the top, with each row having the same diameter.

Sample mounting

As all measurements were taken at cryogenic temperatures, the sample had to be mounted inside a liquid-helium cooled cryostat. Electrical connections between the diode contacts and the (room temperature) measuring circuit must be made, with cables that pass through the cryostat case. The sample needed to be moved relative to the laser beam so that the apertures could be aligned with the laser. Mounting the sample on a stack of piezo stages allows precise control of the sample position, relative to the laser spot.

The sample is first mounted in a non-magnetic, leadless chip carrier and is fixed in place with Ag-paint. Au wires are then bonded from the Ohmic bonding pad, and Schottky bonding pads to the chip carrier pins so that mesas can be connected into the measuring circuit individually. The chip carrier itself is then held in place in a ceramic (Macor) tile, which ensures electrical isolation from the cryostat. Brass screws are then used to make contact with the chip carrier pins and secure the position of the chip carrier. The ceramic tile is then screwed into place on top of the piezo stages. A photograph showing the mounted sample on the piezo stages is shown in fig. 3.4. The Sample temperature is monitored and controlled respectively by a calibrated Cernox temperature sensor and a heating element, which can be added to the mounting plate between the ceramic tile and the piezo stack.

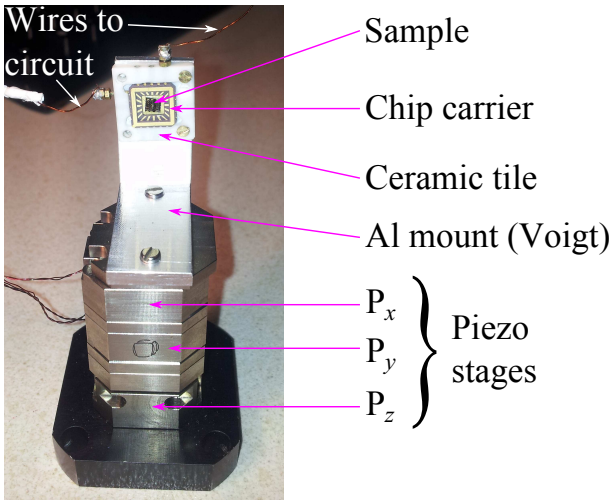

Figure 3.4: Photograph of sample mounted on top of piezo stages. The sample is mounted for Voigt geomety, *i.e,* the sample plane is parallel with the magnetic field direction. An optional temperature sensor and heating element can be attached to a modified Al mount.

3.2.3 Cryostat details

The sample is held in a helium-bath style cryostat (attocube systems) to maintain a stable, low temperature. The cryostat is essentially a 50 l reservoir of liquid helium, which is encased by a vacuum chamber. The entire cryostat is suspended from the case by springs so that the sample is strongly decoupled from vibrations in the environment. A cylindrical tube is used to house the sample, and is inserted into the reservoir. Inside the tube, the sample and piezo-stage assembly shown in fig. 3.4 is supported by a 35 mm cage system, composed of Thorlabs cage-rods and cage-plates. The sample space is sealed and evacuated before inserting into the cryostat and a small volume (< 10 cm^3) of gaseous helium is introduced to allow heat exchange between the sample and the sample-tube walls. The cryostat maintains a stable temperature of 4.20 ± 0.05 K for seven days between helium refills. The sample position is also kept stable enough that the QD remains coupled to the excitation laser even after filling the cryostat.

3.2.4 Magnetic field geometry

A 5 T superconducting magnet is located at the bottom of the helium reservoir in the cryostat, with the field aligned in the vertical direction. The sample in the ceramic tile can be mounted directly into the top of the piezo stages; in this case the magnetic field is applied in the Faraday geometry and the field direction is parallel to the sample growth axis as shown in fig. 2.4 (a). A magnetic field that is applied in the sample plane is termed Voigt geometry, as shown in fig. 2.4 (b). As the field axis is fixed, the sample has to be mounted on a 90° bracket, which is then attached to the top of the piezo stages, as in the green box in fig. 3.5.

3.3 Optics

The optical setup used in these experiments can be configured in two different ways according to the type of experiment being performed. Firstly, as shown in fig. 3.5, an ultra-stable configuration is used where two-pulse measurements are required. In this case, each pulse is independently shaped and then combined into one fiber before being sent to the sample. In the second case, the setup is optimized for high pulse-area single-pulse measurements, with the aim of transmitting a large optical power to the sample. The single pulse setup is shown in fig. 3.6 and is discussed in section 3.3.6.

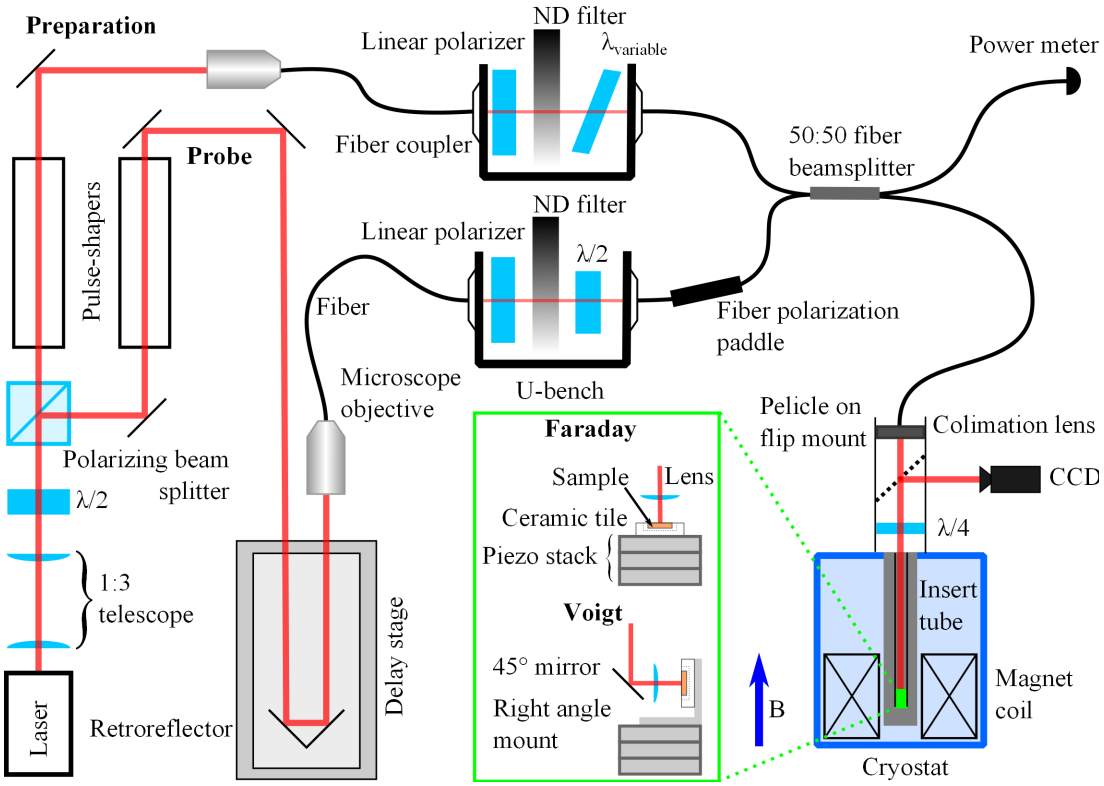

Figure 3.5: Experimental setup for two-pulse measurements.

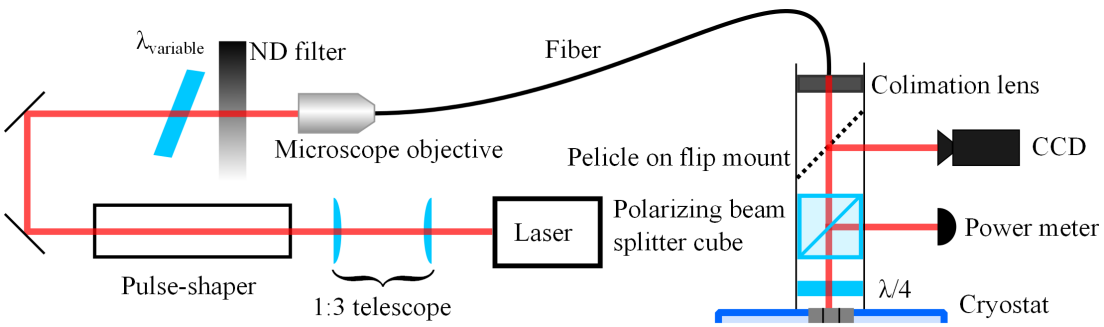

Figure 3.6: Experimental setup for single-pulse measurements.

3.3.1 Laser

The excitation laser used in all experiments is a tunable ultrafast Ti:sapphire (Coherent Mira 900, pumped by a Coherent Verdi G10). The laser is used in mode-locked operation, emitting pulses with a repitition rate of 76.2 MHz, corresponding to a temporal pulse separation of 13.2 ns. The central wavelength in air is tuned close to 955 nm, and the spectral width is 16.2 nm, giving a pulse duration of 80 fs. At best alignment, the optimal average mode-locked power output at this wavelength is 860 mW. 955 nm is approximately the wavelength associated with the neutral exciton transition for the QDs investigated here, ensuring that the maximum resonant power possible is transmitted to the sample. In order to prevent absorption by water vapour in the atmosphere, the Ti:sapphire was purged with dry N_2 and, in typical operation, the relative humidity was <3%. Both the pump laser and the Ti:sapphire crystal were cooled to 17°C by a deionized-water chiller to maintain output stability.

3.3.2 Pulse-shaping

The large pulsewidth of the pulses emitted by the laser makes them unsuitable for single-dot experiments as individual QDs are typically spaced in energy by 1-2 meV. Optical pulse shapers are used to spectrally narrow the pulses. The pulse-shapers can each be considered as a zero-dispersion $4f$ spectrometer, operating in transmission mode, as shown in fig. 3.7. Each pulse shaper consists of a pair of diffraction gratings (1200 lines per mm) in a subtractive dispersion configuration along an optical axis. Two lenses (Thorlabs cylidrical, focal length, $f = 500$ mm) are placed along the pulse shaper-axis such that the total length is $4f$. The lenses are arranged as a 1:1 telescope and each is f away from their respective diffraction grating. In this configuration, the spectral, spatial and angular properties of the output beam of the pulse-shaper are identical in principle to the input beam. A mechanical slit is positioned close to the focal plane at the centre of the pulse-shaper, allowing the selection of a narrow (0.2 meV) band of frequency components. If the slit is positioned exactly at the centre then the resulting pulse has a more top-hat character in the frequency domain and a sinc^2 temporal dependence. A small displacement (dx in fig. 3.7, typically ∼1 cm) results in a Gaussian pulse shape. The slit is mounted on a motorized linear translation stage (Newport MFA-CC) so that it can be scanned across the focal plane to change the wavelength that is selected. Detailed descriptions of ultrafast pulse-shaping, can be found in refs. [114, 115].

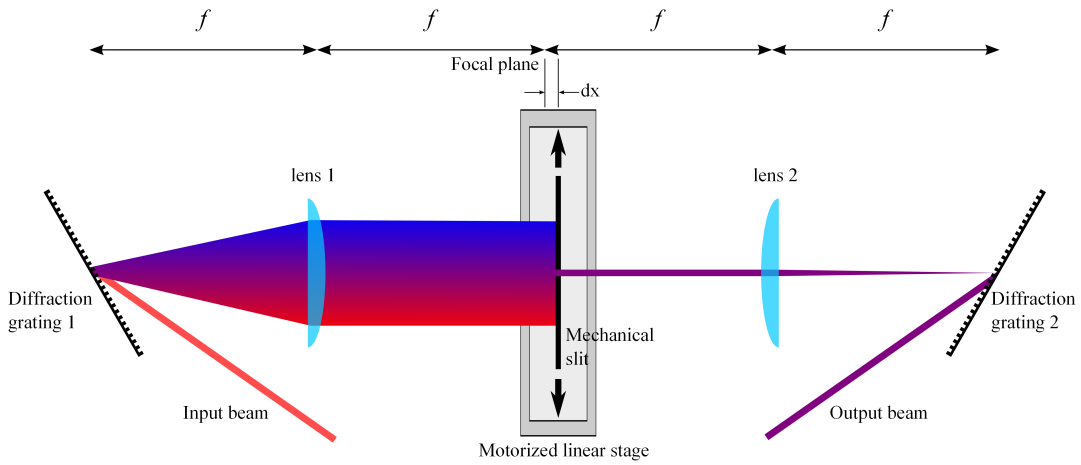

Figure 3.7: Schematic showing the operation of the pulse-shapers.

Pulse-shaper calibration

In order to characterize the output from the pulse-shapers, the optical properties of the output pulses were measured directly with a single spectrometer and back illuminated deep-depletion CCD detector. Fig. 3.8 (a) shows the pulse spectrum as the mechanical slit is scanned across the energy range used in experiments. The amplitudes of individual peaks follow the envelope of the (*almost*) un-shaped Ti:sa pulse. The finite diameter of lens 2 (25.4 mm) clips the outer edges of the spectrum. A close up spectrum of an individual peak is shown in fig. 3.8 (b), confirming that the final pulse after shaping has a Gaussian lineshape. To calibrate the energy of the pulses, the centers of the peaks in (a) are plotted as a function of the slit position in terms of distance along the motorized linear stage in fig. 3.8 (c). As expected for linear dispersion from the diffraction grating, a linear gradient relates the central energy of the pulse to the slit position.

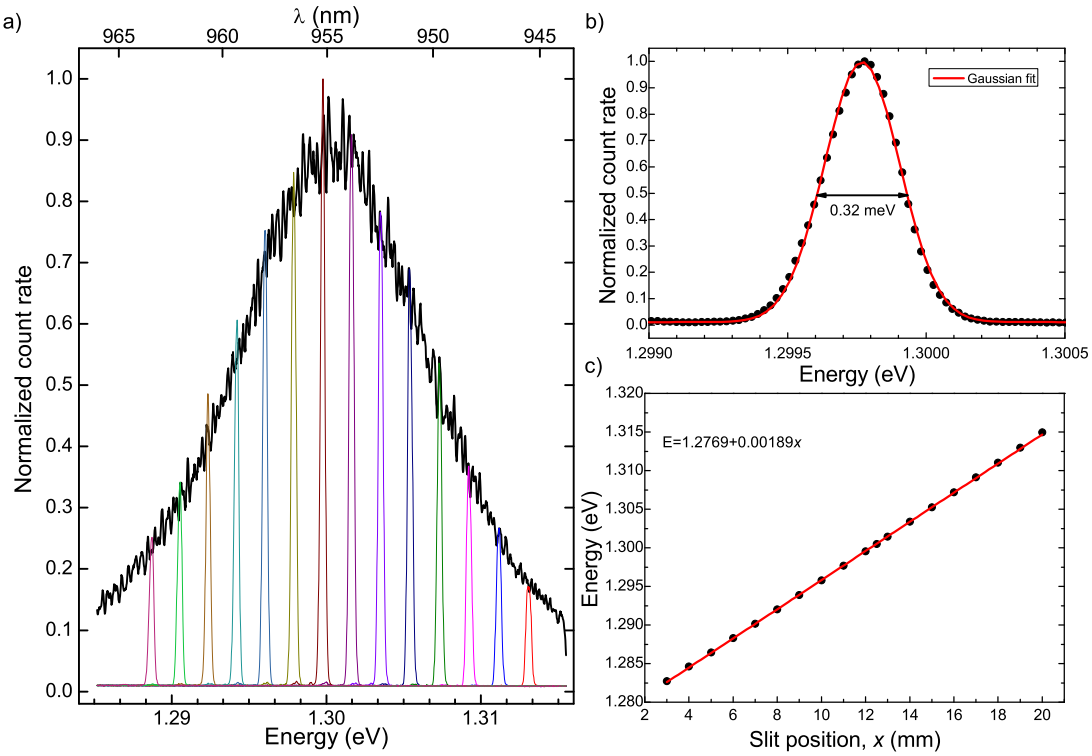

Figure 3.8: (a) Optical spectra showing the output of one of the pulse shapers. Colored lines are individual spectra with the slit at different positions. The amplitudes of these peaks are modulated by the spectrum of the laser pulse with the slit removed (thick black line). (b) Spectrum showing close up region of the peak at 1.29977 eV. Here the width of the slit was set so that the FWHM of the output peak was 0.32 meV. (c) Energy calibration of pulse-shaper, showing a linear relationship between the central energy of the output pulse as a function of the slit position. An equivalent calibration is used for the second pulse-shaper.

3.3.3 Optical delay

An optical delay stage is used in one of the beam paths to give a relative time-delay between the two pulses. The linear stage used is a Newport M-IMS 300, with 300 mm range of travel. Mounted directly on to the stage are two hollow retro-reflectors, each with a very high degree of output parallelism (1 arcsec) and 25.4 mm entrance aperture. A third retro-reflector is fixed in place on the optical table so that in total the beam travels four times the travel of the stage. The maximum extension to the optical path that can be achieved is 1.2 m, equivalent to a time delay of 4 ns. A two-pulse measurement, with both pulses resonant with the QD $|0\rangle - |X^0\rangle$ transition, is carried out in order to calibrate the zero-delay stage position. Quantum interference is observed when the two pulses overlap with each other, with an envelope defined by the pulse shape. Due to the divergence of the laser beam, the power that is coupled into the fiber is reduced by ∼10-15% over the full range of stage travel. In order to maintain the correct power (and therefore pulse area) transmission to the sample, a feedback loop is

used to stabilize the power by adjusting the ND filter angle.

3.3.4 Fiber network

The beams from the two pulse-shapers are individually coupled into optical fibers via microscope objective lenses(Olympus Plan acromat 10x), mounted on a high-precission x, y, z translation stage (Elliot Scientific Gold series xyz flexure stage), allowing 20 nm control over the relative position of the lens and fiber coupler. The microscope objectives were chosen to have a numerical aperture of 0.25 and a working distance of 10.6 mm in order to match the mode diameter of the focussed laser beam with the fiber diameter. Before focussing, the laser beam diameter is $\sim$10 mm. Coupling the light into the fibers is a major source of power loss; typically the transmission into the fiber is 30-50%. Connectorized single-mode fibers (thorlabs SM800) were used throughout the fiber network; these are specified for a wavelength of 830 ± 150 nm, with a low wavelength cut-off at 730 ± 30 nm. The fiber has a mode field diameter of 5.6 μm, encased in 125 μm cladding. Where possible, angle-polished fibers are used in order to minimize back-reflections, which would otherwise return to the laser cavity, reducing stability. After passing through the U-benches (see below), the fibers are combined using a 50:50 fiber-beamsplitter so that only one fiber is used to deliver the beam to the sample. The other output of the fiber beamsplitter is used for directly monitoring the power.

3.3.5 Polarization and intensity control

Individual control of the intensity and polarization of each pulse is achieved by using a free-space break in the fiber path. The fibers from the microscope objectives are connected to a (Thorlabs) U-bench system, as shown in fig. 3.6. Free-space optical components can then be inserted into the beam path before the beam is returned to the fiber. Both fiber couplers on the U-bench have 5-axis position control, allowing good transmission ($\sim$60%) through the U-bench.

Polarization control

An arbitrary birefringent phase shift is induced by passing the beam through the series of fibers. In order to keep this phase shift constant, the fibers are physically fixed in place so that the fiber tension is kept constant. Compensating for the fiber phase-shift adds a extra layer of complexity to the polarization control and is accomplished by the following procedure:

Firstly, the polarization is set in the preparation pulse arm to be linearly polaraized after the fiber to the sample by using the optics in fig. 3.6. A linear film polarizer is used to ensure that the polarization is initially in a well-known state; this polarizer is rotated to match the laser polarization. Film polarizers are used in order to minimize the

beam deflection through the polarizer as opposed to Glan-Thompson style polarizers. A variable quarter-wave plate is then used to compensate for the effect of the fiber. The extinction ratio, measured using another nominally identical film-polarizer is 1:1000.

Secondly, the polarization of the probe pulse arm is set relative to the preparation arm. Again a linear polarizer is used in the U-bench, so linear polarization is used initially. Compensation for the fibers is achieved by using a three-paddle fiber-waveplate to ensure a highly linearly polarized output (extinction ratio ∼1:500). The angle of the linear polarization is rotated by a motorized half-wave plate in the U-bench so that CO and CROSS-linear polarization with the preparation pulse can be selected.

Finally, for circularly-polarized excitation, a quarter-wave plate is inserted after the sample fiber, with fast axis rotated 45° relative to the polarization axis of the preparation pulse. The polarization of the probe pulse is then transformed into CO and CROSS circular polarization, with respect to the first pulse depending on its linear polarization direction.

Intensity control

The power of each beam is controlled with a circularly graduated neutral density (ND) filter mounted on a (Newport PR50-PP) rotation stage. Inside the U-bench, the free space beam is extremely stable in terms of direction, so this make a suitable point for the ND filter. A second advantage of filtering the power in the U-bench is that the beam diameter is very small (less than 0.5 mm), meaning that across the beam diameter, only a small change in the ND filter graduation so the power is filtered evenly at opposite sides of the beam.

3.3.6 High pulse area measurements

As the pulse area of the Rabi oscillation is proportional to the square root of incident power (eq. (2.5)), high excitation powers (typically ∼200-500 μW) are necessary in order to reach high pulse areas. In this case, the optical setup is modified by only including one pulse-shaper and removing as many of the lossy fiber optic components as possible, as shown in fig. 3.6. Here, the polarization compensation and power attenuation take place before the microscope objective. After the fiber collimator, the beam passes through a high-quality polarizing beam splitter. The laser already has a high degree of polarization, which is refined by the beam splitter. This method provides a similar extinction ratio to the film polarizer but allows the rejected (cross-polarized) part of the beam (typically less than 10%) to be sampled by the power meter.

3.3.7 Laser focusing at sample

A 4.51 mm focal length lens (Edmund Optics Molded Aspheric) is used to concentrate the laser intensity on the sample surface so that maximum power can be delivered to the

single QD. This lens has diameter 6.33 mm and numerical aperture 0.55, giving a final spot size for $\lambda = 950$ nm is $\sim$1.8 μm (FWHM of Gaussian electric field distribution).

3.3.8 Imaging and aperture optimization

The surface of the sample is imaged by inserting a pelicle beamsplitter into the beam path between the fiber collimator and the quarter-wave plate on the cryostat shelf. The scattered light form the sample is focused onto a CCD camera and the signal is viewed on a screen. The laser spot is defocused slightly, giving a field of view approximately 10 μm in diameter, allowing features on the surface to be identified. The sample is moved relative to the laser beam by using the piezo-stages. Once the aperture is located, a photocurrent (PC) spectrum is measured, and any exciton peaks are identified. The laser wavelength is set to match the QD transition and then the position of the sample is further optimized by making individual steps with all three piezo-stages so that the signal is increased. Several iterations of optimizing the signal and reducing the power so that the pulse area, $\Theta \approx \pi/2$ (where the PC is most sensitive to a change in the sample position) are performed. When optimized, the QD is positioned within the error of the minimum piezo-stage step (<10 nm) of the centre of the optical field, and the focal point of the lens.

3.4 Photocurrent spectroscopy

3.4.1 Electron and hole tunneling

The band structure of the QD photodiode under reverse bias is shown in fig. 3.9. For an ideal photodiode, the dark current flowing between the electrical contacts under reverse bias should be zero. In practice, an acceptable value for the dark current is less than 100 pA at a reverse bias of 3 V. This limit ensures that the response of the dark current with reverse bias is essentially flat in the experimental region of interest, allowing the photocurrent signal to be clearly observed. In order to make a current flow, electrical carriers must be injected into the intrinsic region. As the QD is optically active, electron and hole pairs are photogenerated by an incident laser pulse. Each carrier tunnels out of the dot and the resulting photocurrent can be measured. In the samples used here, an additional AlGaAs barrier is present, blocking hole tunnelling. This was included as the sample was originally grown for single-hole experiments. The Schottky device structure was chosen over a $p-i-n$ diode as it simplifies the MBE growth due to only requiring a single dopant. However in the work of Zrenner *et al* [51], $p-i-n$ structures are used successfully for photocurrent measurements.

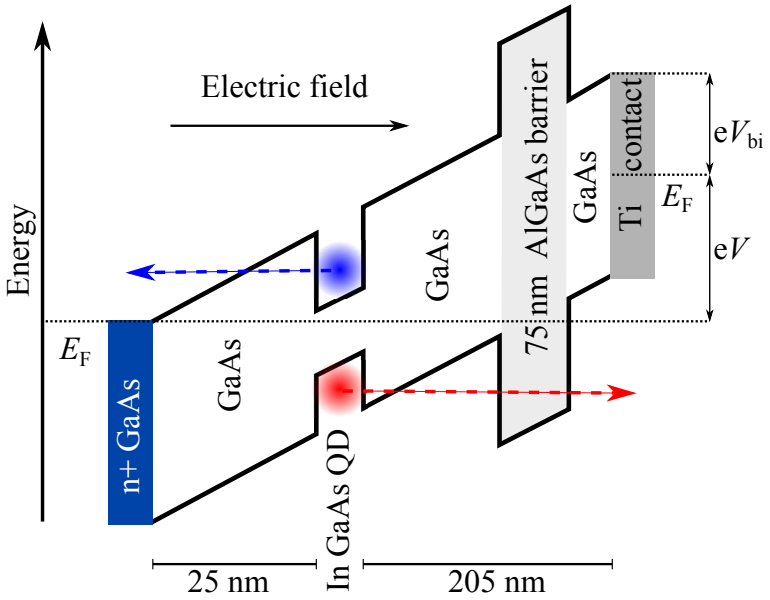

Figure 3.9: Schematic showing the band diagram of the single QD photodiode under reverse bias. An electron (blue) or hole (red) confined in the dot tunnels out and can be measured as a photocurrent. E_F is the electron Fermi-energy.

The electric field (F) applied to the sample is given by eq. (3.1) [35]

$$F = (V + V_{bi})/W_i, \tag{3.1}$$

where V is the applied *reverse* bias, V_{bi} is the built-in voltage of the diode, which is estimated to be 0.76 V (half the band gap of GaAs), and W_i is the width of the intrinsic region. W_i is considered to be the distance between the Ohmic and Schottky contacts, which for these samples is 230 nm. The voltage range used here ($0.5-1.2$ V) correspond to a range of applied electric fields of $5.48 - 9.39$ MVm^{-1}. Tuning the applied field tilts the band diagram in fig. 3.9 and at some fields can allow charges to tunnel onto the QD from the contacts, giving control of the charge state of the QD [36]. Typically the diode has to be positively biased or at a very small reverse bias to allow charges to tunnel in, while at larger reverse biases, in the case of no illumination, the QD is uncharged.

3.4.2 Measurement circuit

The measuring circuit is specifically designed to reduce ground loops in order to ensure that electrical noise levels in the circuit were minimized. A schematic diagram of the measuring circuit is shown in fig. 3.10. Ground loops were avoided by using a single, common ground on the chassis of the pico-ammeter (Keithly 6485). The case ground of the voltage source (Keithly 230) and the cryostat ground were both grounded through this connection. Coaxial BNC cables were used throughout the circuit, with the outer core used exclusively as shielding, as indicated by the blue lines in the circuit diagram.

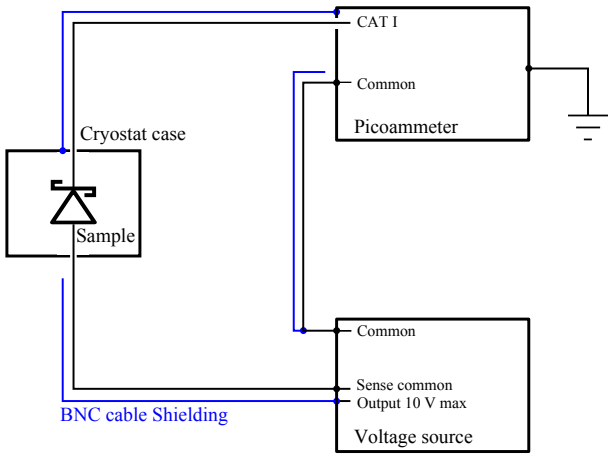

Figure 3.10: Photocurrent measuring circuit. The blue lines represent the outer core for coaxial cables, used as shielding only.

3.4.3 Electrical properties of the sample photodiode

Photocurrent detection requires that the diodes have extremely good electrical properties. I-V curves for the diode used in this work are shown in fig. 3.11 for room temperature and (inset) 4.2 K. The breakdown voltage of these diodes is approximately -6 V. In reverse bias, the dark current is very low: less than 20 pA is observed up to 3 V at room temperature. When the sample is cooled to 4.2 K, this is reduced to 5.3 pA, with a gradient of 0.22 $\pm$0.02 pA/V. The inset in fig. 3.11 is a close up of the reverse bias at low temperature and shows noise fluctuations present in the dark current of $\pm$0.6 pA. The low dark current and flat response with voltage means that an excellent signal to noise ratio can be achieved, across a range of reverse bias values.

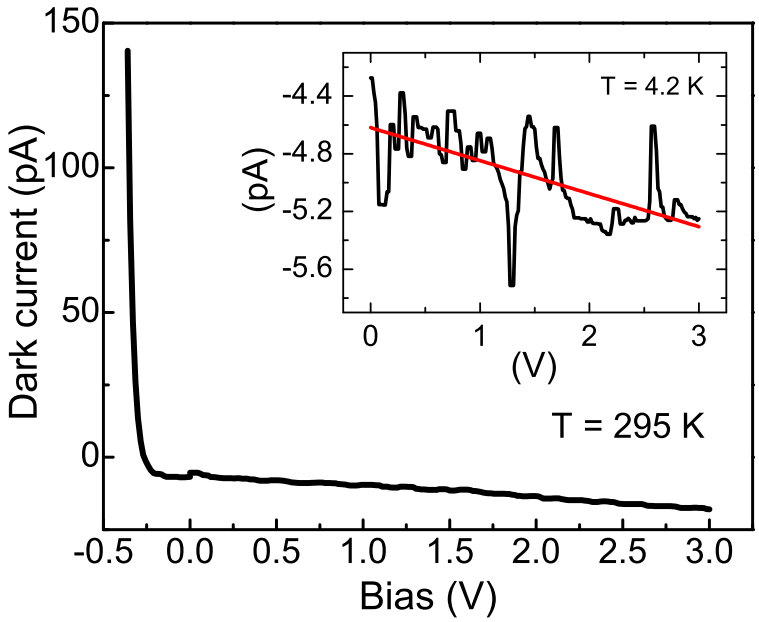

Figure 3.11: Dark IV curves at 295 K and 4.2 K (inset). Due to the definition of the E-field direction in eq. (3.1), negative bias voltages indicate forward bias behaviour and positive voltages correspond to reverse biases. The red line in the inset is a linear gradient.

3.4.4 Photocurrent spectra

An example PC spectrum showing a close up of the neutral exciton peak is shown in fig. 3.12. The spectrum is taken by scanning the linear stage in the pulse-shaper and recording the photocurrent as a function of slit position. Each data point is recorded at intervals of the stage travel of 0.02 mm, equivalent to an energy spacing of 37 μeV. The pulse area of the laser in this measurement is π and $V = 0.9$ V. The resolution of spectral lines is limited by the 0.2 meV pulse spectral width of the laser, meaning that individual QD lines can be seen if they are well spaced in energy but the fine-structure is too small to be resolved. The maximum amplitude for a single exciton peak is 12.2 pA. This value corresponds to a single electron charge multiplied by the pulse repetition rate of the laser (76.2 MHz) [51]. The shape of the peak in the spectrum excellently replicates the excitation laser's Gaussian lineshape, as shown previously, in fig. 3.8 (b). It is important to note that the photocurrent spectrum uses the exciton transition to sample the laser power, rather than the electric field intensity.

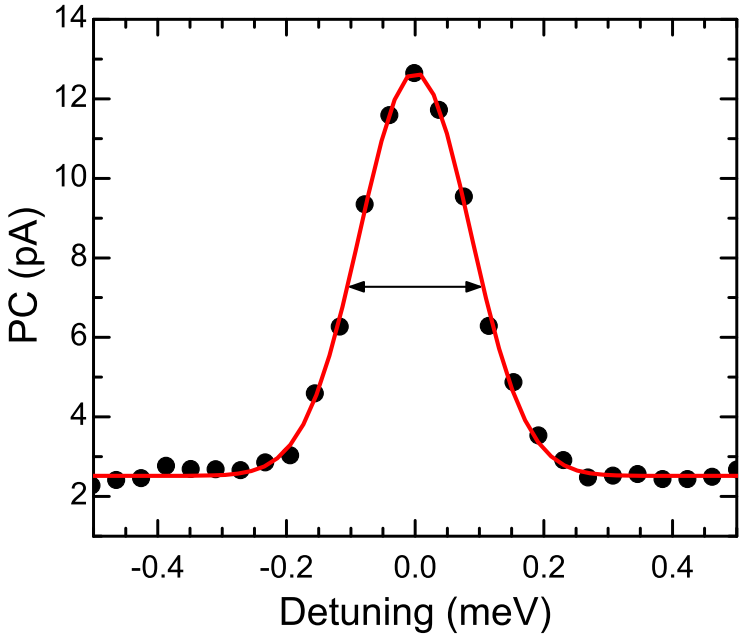

Figure 3.12: Close up PC spectrum showing X^0 peak in detail. The red line is a Gaussian peak fit. For this measurement, the laser is circularly polarized. The FWHM of the peak is 0.202 meV, replicating the linewidth of the laser. A background PC of 2.5 pA is present in the data, attributed to carriers generated non-resonatly in the semiconductor. The QD featured in this spectrum is labelled C1A in fig. 4.1 (a).

3.5 Summary

The combination of the methods presented in this chapter give an extremely stable experimental set-up, which is capable of controlling QD states via ultrafast optical pulses. Polarization-dependent, time-resolved photocurrent detection is possible, with individual control over all the pulse properties. Extremely low photocurrent signals can be measured giving an accurate value as to the excitonic occupation of the single dot.

Chapter 4

Characterization of quantum dot properties

This chapter includes a comparison of the quantum dot properties for thee dots that are used experimentally throughout this thesis. The specific properties that are relevant to this work are the neutral exciton absorption energy, Rabi rotation, fine structure, DC Stark shift, and the electron and hole tunnelling rates.

4.1 QD absorption energy identification

Figure. 4.1 displays PC spectra for the two apertures studied in this work. The apertures are both found in the same column of apertures in the array and consequently have the same diameter (nominally 400 nm). In aperture C1, three QDs are clearly identified in the energy range shown, of these, C1A and C1B are well-coupled to the laser field and show a strong signal (approaching the theoretical maximum 12.2 pA, as discussed in § 5.1) with amplitudes close to 10 pA. The dot labelled C1C is poorly coupled so the signal is reduced. A slight shoulder is observed on the low-energy side of the C2A peak. This is attributed to a very weakly coupled dot and is not considered to affect the properties of C2A.

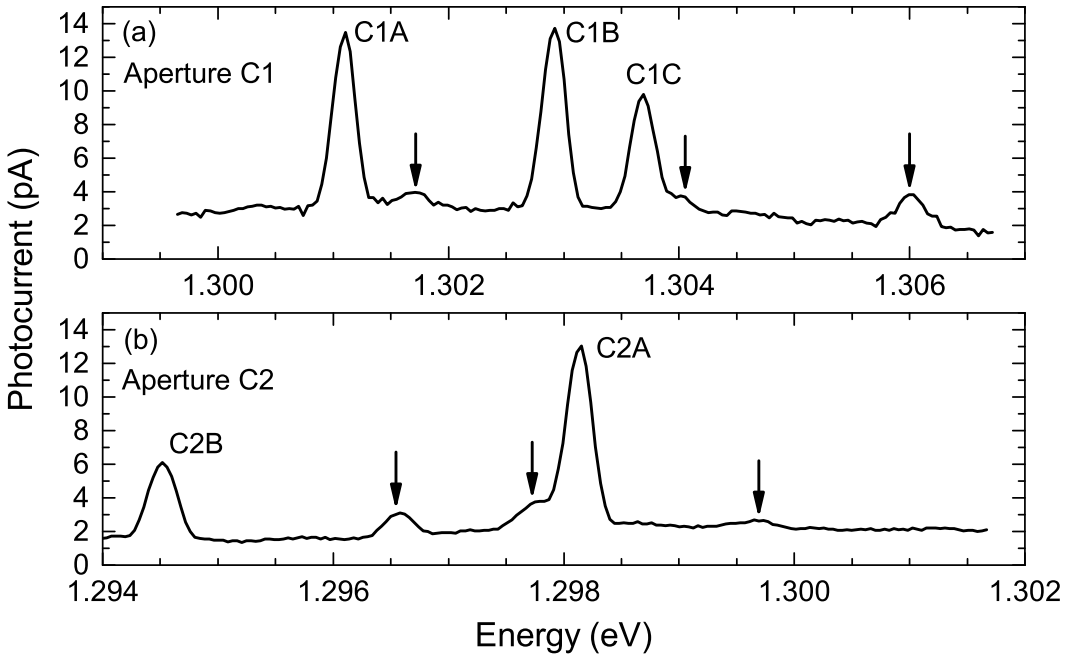

Figure 4.1: QD identification spectra. PC spectra measured for two different apertures on the sample. (a) shows a spectrum measured for aperture C1 and (b) shows a similar spectrum for aperture C2. Individual QDs are labelled from low to high energy for each aperture. $V = 0.9$ V in both spectra. C1A, C1B and C2A are considered to be well-coupled to the optical field and spectrally isolated enough to be suitable for single-dot spectroscopy. The arrows indicate more weakly coupled dots that are also present in the spectra.

4.2 Neutral exciton Rabi oscillation measurements

An example Rabi oscillation measurement is shown in fig. 4.2. This kind of measurement is performed by tuning the laser to be on resonance with the QD neutral exciton transition and measuring the photocurrent as the power is increased, by stepping the angle of the ND filter in the rotation mount. A background PC is observed, and subtracted from all Rabi oscillation measurements. The background is linearly proportional to the laser power and attributed to incoherent absorption from other nearby QDs in the wafer. The raw data from the measurement are shown in fig. 4.2 (a). The background PC has a gradient of 1.085 ± 0.002 pA/μW and this value is typical for other similar measurements. Subtracting this background reveals the Rabi oscillation, as shown in fig. 4.2 (b).

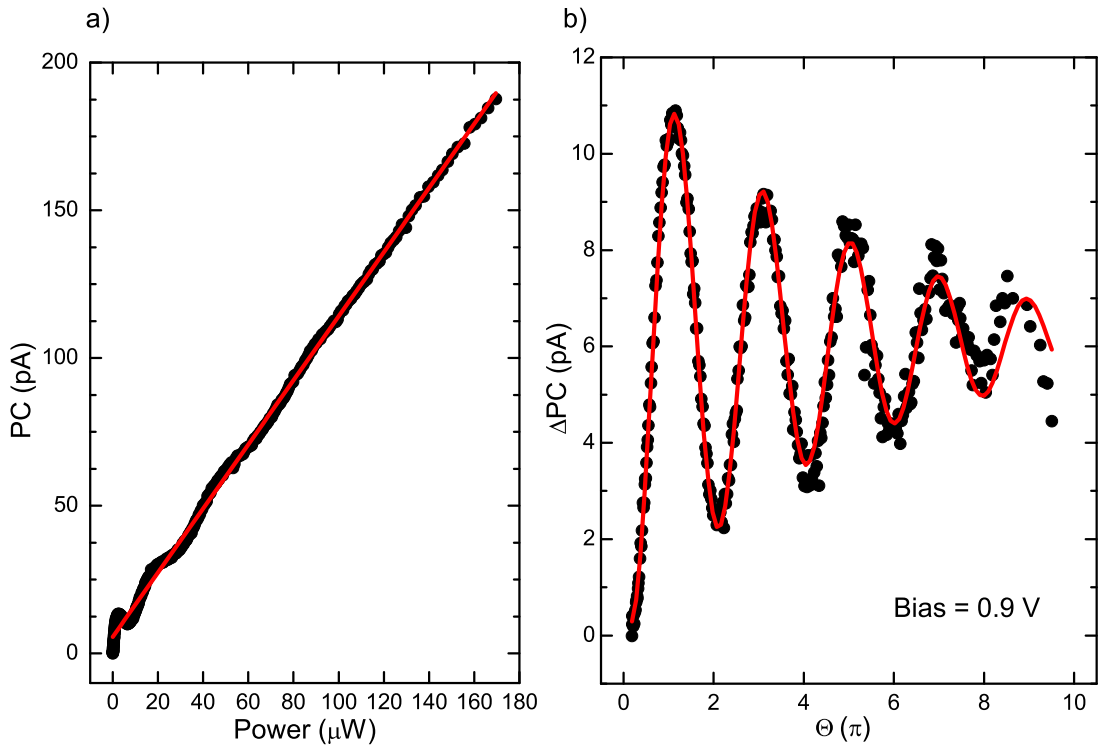

Figure 4.2: Example Rabi oscillation measurement. This measurement was carried out with the laser on resonance with the neutral exciton transition of the C1B QD. (a) Raw data from the measurement, the red line is a linear fit, which gives the background PC. (b) Data after background subtraction, plotted against pulse area, which is proportional to the square root of the power in (a). The red line in (b) is a fit to a damped sinusoid function.

4.3 Inversion recovery technique

An inversion recovery measurement was performed as described in ref. [64]. The photocurrent is recorded for two, time-separated π-pulses, as a function of the inter-pulse time delay, τ_{delay}. Both pulses are circularly polarized; the pump pulse is σ^+-polarized and the probe can be chosen to be σ^+ (co-polarized with the pump), or σ^- (cross-polarized with the pump). The population inversion of the system is probed by the absorption of the second pulse and exciton spin information is investigated by making use of the circularly polarized selection rules for the neutral exciton, as given in fig. 2.3 (b). The raw data from a typical inversion recovery measurement on the QD identified previously as C2A are presented in fig. 4.3, as a function of voltage for both co, and cross-polarized pulses. Similar measurements were carried out for C1A and C1B, but are not presented here.

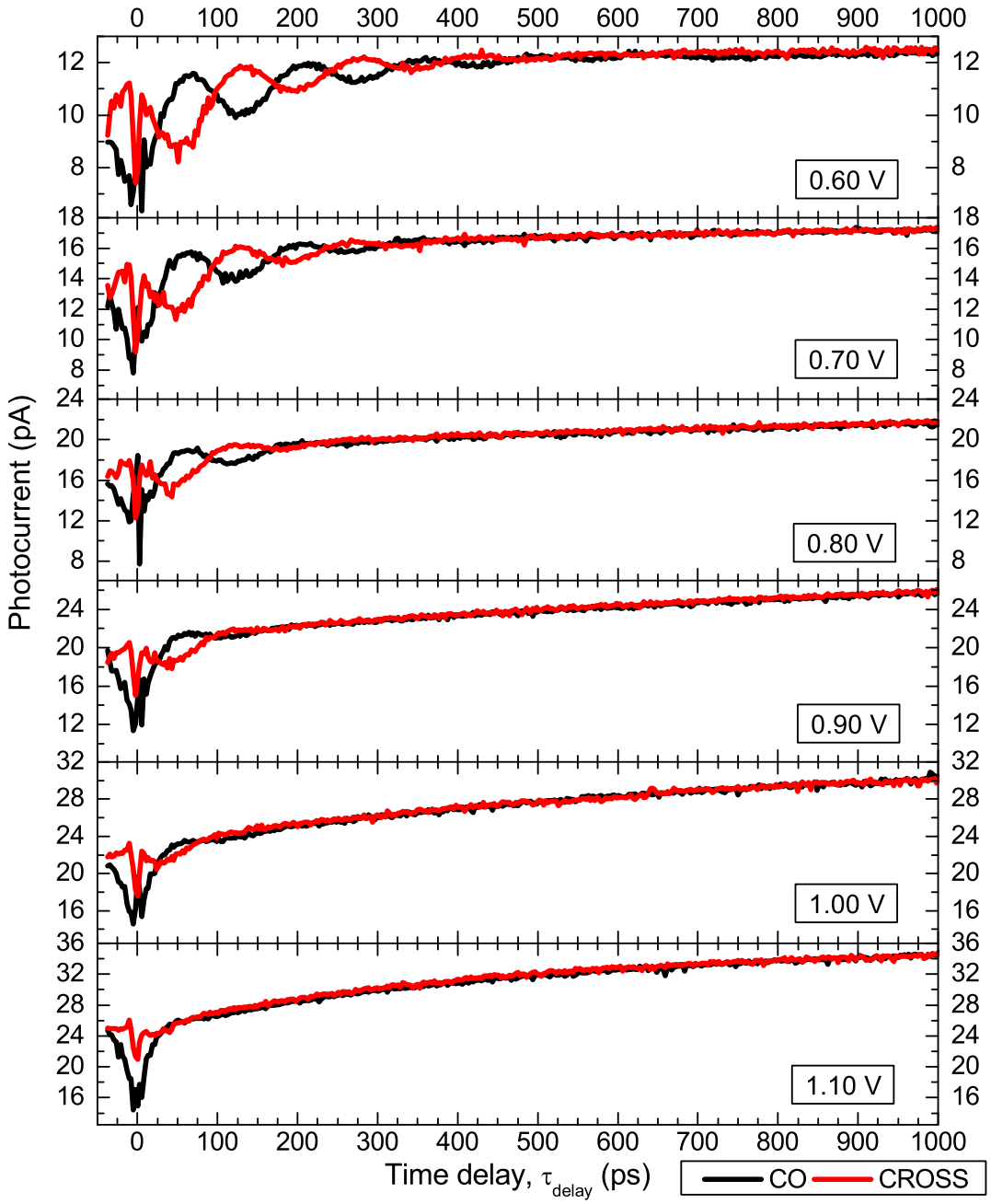

Figure 4.3: Co and cross-polarized inversion recovery measurement C2A. The photocurrent in each case is recorded as a function of the pulse time delay τ_{delay}.

Three phenomena are observed in the data in fig. 4.3. Firstly, interference is observed for delay times close to zero. This interference corresponds to the overlap of the two-pulses and is used to calibrate the zero-delay position of the linear stage that is used to extend the delay time. Secondly, for $\tau_{\text{delay}} < 750$ ps, an out of phase oscillation is observed between the co and cross-polarized traces, this is due to the precession of the neutral exciton due to its fine-structure splitting and is discussed in § 4.3.2.

Thirdly, there is an overall increase in the value of the photocurrent as the delay time is extended; this is related to the exciton lifetime, which, as discussed in § 4.3.1, is related to the electron and hole tunneling times.

4.3.1 Voltage dependent tunneling rates

The voltage-dependent tunneling rates for the three QDs C1A, C1B and C2A were extracted from the sum of the co and cross-polarized inversion recovery measurements for each dot. The photocurrent sum is initially low, corresponding to the second pulse driving a Rabi oscillation from $|X\rangle$ back to $|0\rangle$. As the time delay is increased, the electron and hole tunnel out of the dot, and at long time delay values, the second pulse is able to excite another exciton. The second electron and hole subsequently tunnel out of the dot, increasing the PC signal. For an infinite time-delay, the PC is equal to the sum of the PC from each individual pulse. This is referred to as $PC_{\tau_{\text{delay}}=\infty}$. The photocurrent sum is normalized according to eq. (4.1):

$$\Delta PC^{\text{Norm}}(\tau) = \frac{1}{2PC_{t=\infty}} \left(PC_{\text{CO}}(\tau) + PC_{\text{CROSS}}(\tau) - 2PC_{\text{BG}}^{\text{2pulse}} \right), \tag{4.1}$$

where $PC_{\text{BG}}^{\text{2pulse}}$ is the combined background photocurrent for the two pulses. Fig. 4.4 shows the normalized photocurrent sum as a function of time delay for the data in fig. 4.3.

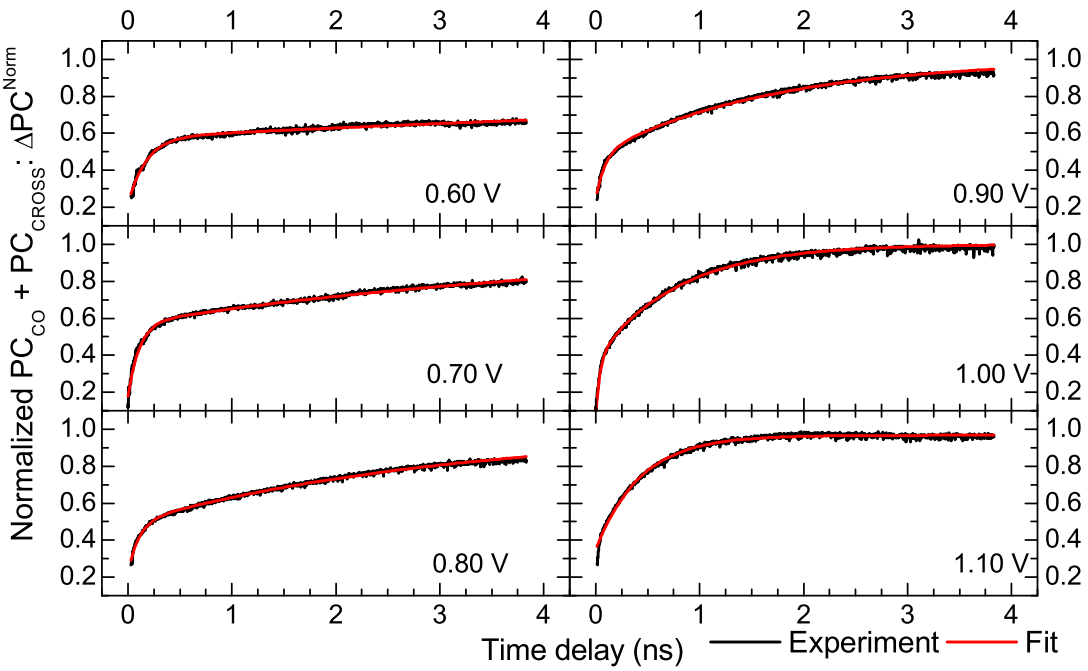

Figure 4.4: The normalized photocurrent sum ΔPC^{Norm} is plotted as a function of the interpulse time delay for the inversion recovery measurement in fig. 4.3.

In order to obtain the electron tunneling rate Γ_e and the hole tunneling rate Γ_h, the normalized sum $\Delta PC^{\mathrm{Norm}}$ in is fitted with eq. (4.2) to give two exponential coefficients t_1 and t_2, where $t_1 < t_2$. The results of the fits are shown as the red lines in fig. 4.4.

$$\Delta PC^{\mathrm{Norm}}(\tau_{\mathrm{delay}}) = 1 - A\exp(-\tau_{\mathrm{delay}}/t_1) - B\exp(-\tau_{\mathrm{delay}}/t_2). \tag{4.2}$$

Here $A \approx B \approx 0.5$. The faster decay constant, t_1 is equal to the exciton lifetime T_1^X in eq. (2.10). t_1 is related to the electron tunneling rate, Γ_e, by $\Gamma_e = 1/t_1 - \Gamma_r$, where Γ_r is the radiative recombination time. The hole tunneling rate is considered to be equal to the longer time constant: $\Gamma_h \equiv 1/t_2$. For measurements where $V > 1$ V, the electron tunneling time is fast enough to be considered instantaneous and $t_1 \to 0$. As the inversion recovery was measured as a function of the applied bias voltage, the voltage dependence of the tunneling rates can be found. Fig. 4.5 plots the values of Γ_e and Γ_h as a function of bias voltage for C1A, C1B and C2A. For all three QDs, the electron tunneling rates shown by the red triangles were obtained by taking Γ_r to be 1/400 ps, as this value was calculated explicitly for C2A (for details, see § 5.2). Since the three QDs are a similar size, it is reasonable to expect similar values for C1A and C1B. To assess the effect of the uncertainty in knowing Γ_r, each of the curves was obtained by first calculating Γ_e, as a function of Γ_r.

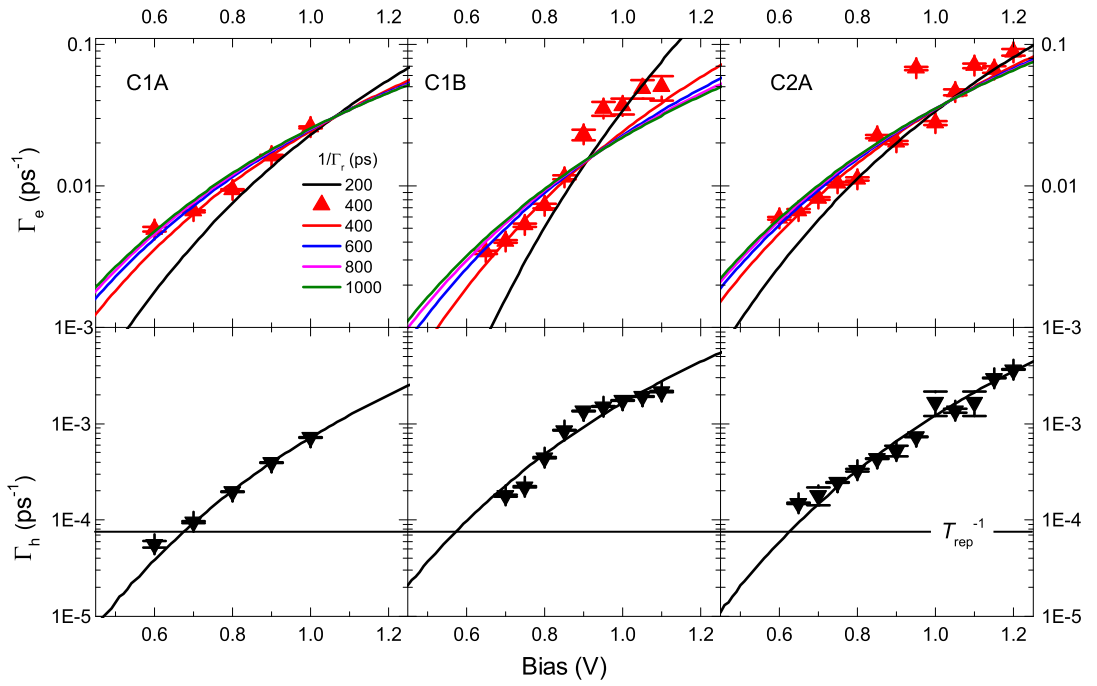

Figure 4.5: Electron (Γ_e) and hole (Γ_h) tunneling rates vs bias voltage for the three QDs: (a) C1A, (b) C1B and (c) C2A used in the experiments presented here. Solid lines are fits to the WKB expression in eq. (4.3), calculated after individually extracting Γ_e for the range of Γ_r values shown. The horizontal line in the lower panels represents the laser repetition frequency, T_{rep}^{-1}.

$1/\Gamma_r$ (ps)	200	400	600	800	1000
C1A	145	107	98	94	92
C1B	212	138	124	118	115
C2A	115	90	83	81	79

Table 4.1: Electron tunneling time $1/\Gamma_e$ in ps at a bias 0.8 V for the range of radiative recombination rates used in fig. 4.5. The error in the tunneling times is ∼1 ps.

The curves show that values of $1/\Gamma_r$ in the range $400-1000$ ps all provide a similar value for the electron tunneling rate. If the radiative lifetime is reduced to 200 ps, then the curve shifts significantly, indicating that this is not a sensible value. In table 4.1, the electron tunneling times are summarised for the full range of recombination times found in the literature [92], for the three QDs at a reverse bias of 0.8 V, as is typically used in experiments. If the values for $\Gamma_r = 1/200$ ps are excluded, then the maximum uncertainty in Γ_e if γ_r is 1/400 ps can be found, for C1A: -15 ps (14%), C1B: -23 ps (17%) and C2A: -11 ps (12%).

An exponential increase in the tunneling rates is observed with increasing voltage, as verified by the curves, which are fits to the WKB-expression given in eq. (4.3) for the voltage-dependent tunneling rates [116].

$$\Gamma_{e(h)}(V) = \Gamma_{e0(h0)} \exp\left(\frac{-V_{e0(h0)}}{V + V_{bi}}\right), \tag{4.3}$$

where V is the reverse bias, $V_{bi} = 0.76$ V is the built-in voltage (as described in §3.4) and $\Gamma_{e0(h0)}$, $V_{e0(h0)}$ are constants. The black horizontal line in fig. 4.5 indicates the repetition rate of the laser (76.2 MHz), the hole tunneling rate crosses this point when the voltage is 0.70 V for C1A, 0.59 V for C1B and 0.62 V for C2A.

4.3.2 Neutral exciton fine structure

The fine structure splitting $\hbar\delta$ is measured experimentally in the photocurrent regime as an oscillation in the polarization of the exciton in time. This oscillation is evident as a beat between the time-resolved PC signals for CO and CROSS-circularly polarized excitation. The line width of the laser is much larger than $\hbar\delta$, meaning that the splitting, which is typically of the order of 10 μeV, is too small to be resolved spectrally. The exciton states $|\Uparrow\downarrow\rangle$ and $|\Downarrow\uparrow\rangle$ are created by the absorption of σ_+ and σ_--polarized pulses, respectively. As these are both superpositions of the linear excitonic eigenstates described in eq. (2.1), the state vector coherently precesses between the two circularly-polarized states with angular frequency $\omega_{prec} = \hbar\delta$. The oscillation is observable in both traces as shown in fig. 4.3, with each trace having opposite phase. To measure the fine structure, the difference between the co and cross-polarized photocurrent ($PC_{CO} - PC_{CROSS}$) is examined as the difference clearly reveals the oscillation.

The plots in fig. 4.6 show the difference for the inversion recovery measurements for C2A for the range of applied bias values used in fig. 4.3:

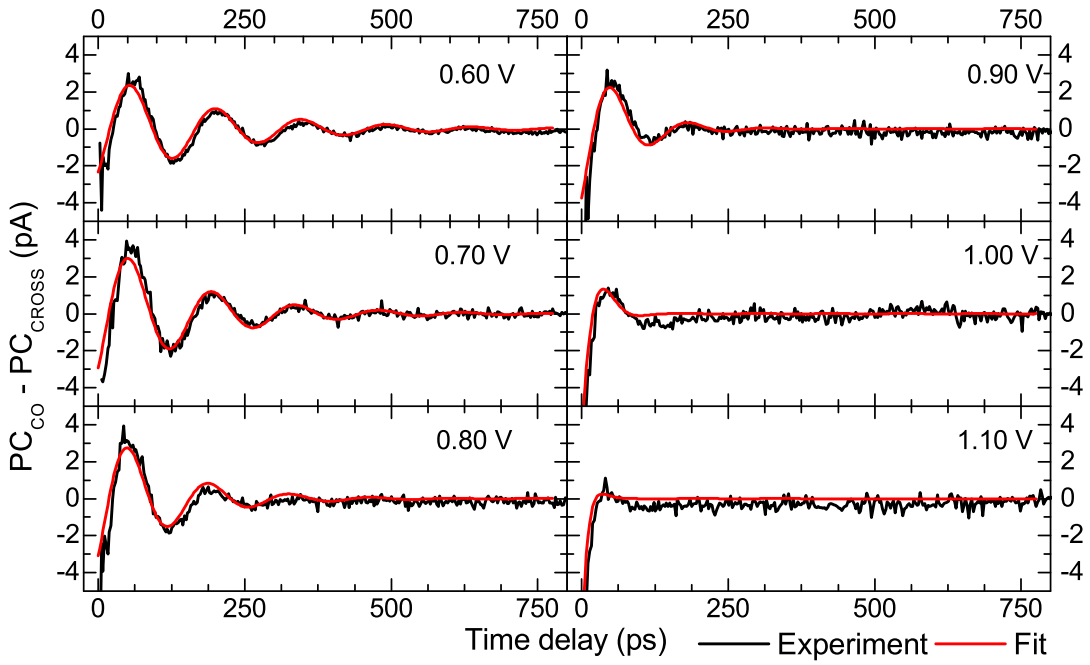

Figure 4.6: The normalized photocurrent difference $PC_{\mathrm{CO}} - PC_{\mathrm{CROSS}}$ is plotted as a function of the interpulse time delay for the inversion recovery measurement in fig. 4.3.

Similar measurements were carried out for all three dots. The curves in fig. 4.6 were fitted with eq. (4.4). The fits are shown as red lines.

$$PC_{\mathrm{CO}} - PC_{\mathrm{CROSS}} = A\exp(-\tau_{\mathrm{delay}}/t_0) \times \sin(\omega_{\mathrm{prec}}\tau_{\mathrm{delay}} - \phi), \tag{4.4}$$

where t_0 is the decay time of the oscillation and ϕ is the phase. The observed damping is due to the decay of the exciton following the first pulse and strong damping is typically observed when $V > 1.05$ V (as can be seen in the 1.10 V plot in fig. 4.6) as the electron tunnelling rate is significantly increased at high electric fields. The resulting fine structure precession time was extracted from ω_{prec}. The values of the fine structure splitting for the dots C1A and C2A are shown in fig: 4.7. C1B does not exhibit any fine structure precession in the inversion recovery data at all; the traces for both PC_{CO} and PC_{CROSS} simply show the bi-exponential decrease expected for carrier tunneling. For this QD, an estimate of the minimum energy splitting that can be resolved with the time-resolved technique is presented in lieu of the actual values.

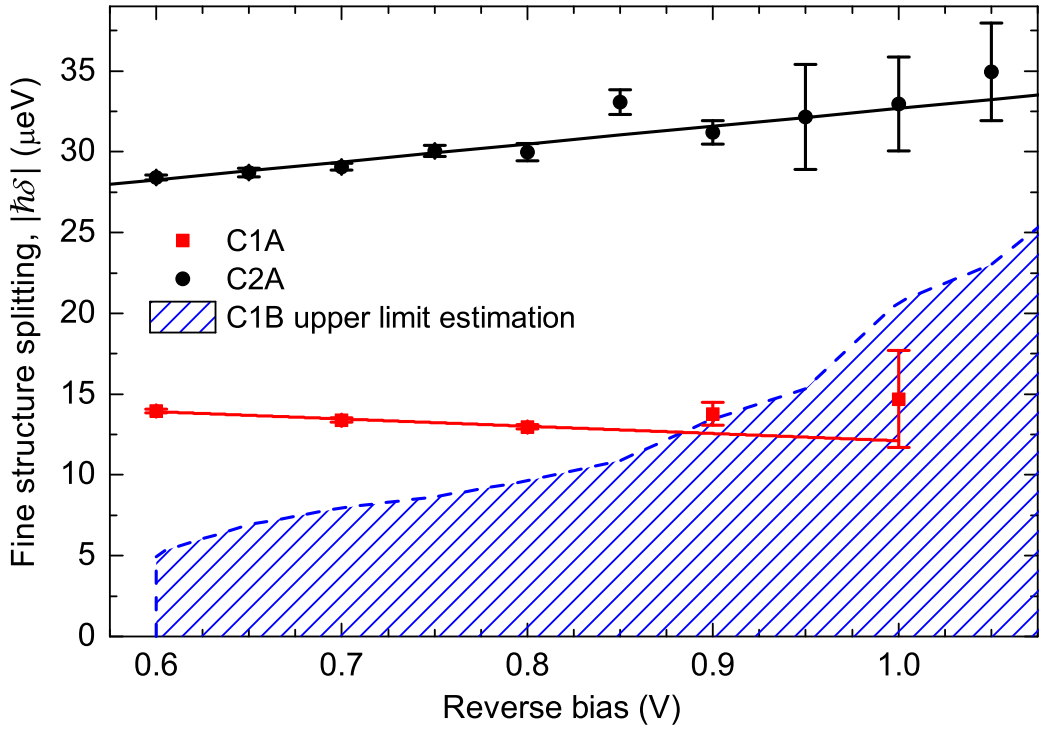

Figure 4.7: Neutral exciton fine structure splitting $\hbar\delta$ as a function of bias voltage for the QDs C1A and C2A used in the experiments presented here. C1B does not exhibit a fine structure precession so the estimate for the maximum resolvable fine structure splitting for this QD is presented. Solid lines are linear fits to the data.

The values of $\hbar\delta$ for C1A and C2A are shown to be linearly dependent on voltage, with values ∼15-12 μeV in the voltage range used in these experiments for C1A and ∼28-35 μeV for C2A. If a similar linear relation is to be expected for C1B, then the maximum values for $\hbar\delta$ are estimated to be ∼5-10 μeV, although it is possible that this dot might even have a near-zero fine structure splitting. The gradients of the fitted lines and -4.50 ± 0.98 μeV/V (-0.10 ± 0.02 μeV kV^{-1} cm) for C1A, and $+11.02\pm1.64$ μeV/V ($+0.25\pm0.04$ μeV kV^{-1} cm) for C2A. These values agree well with the values that are reported in the literature, for example results reported by Bennett *et al* [117] give a value of 0.285 μeV kV^{-1} cm for the magnitude of the gradient for the fine structure splitting of similar dots that are tuned by a vertical field. In Bennett's work, five QDs are investigated, with four of them showing a negative gradient, and one having a positive gradient in the range of fields shown in fig. 4.7 (50-80 kV cm^{-1}). A similar measurement by Trotta *et al* [118] gives a parabolic dependence of the fine structure splitting on F, although in the 50-80 kV cm^{-1} region, the curve can be approximated by a gradient of ≈ -0.15 μeV kV^{-1} cm.

4.4 DC Stark shift of neutral exciton

The application of a DC voltage to the sample shifts the neutral exciton energy according to the DC Stark shift, as described in eq. (2.3). The DC Stark shift as a function of bias voltage for the the QD C2A is presented in fig. 4.8.

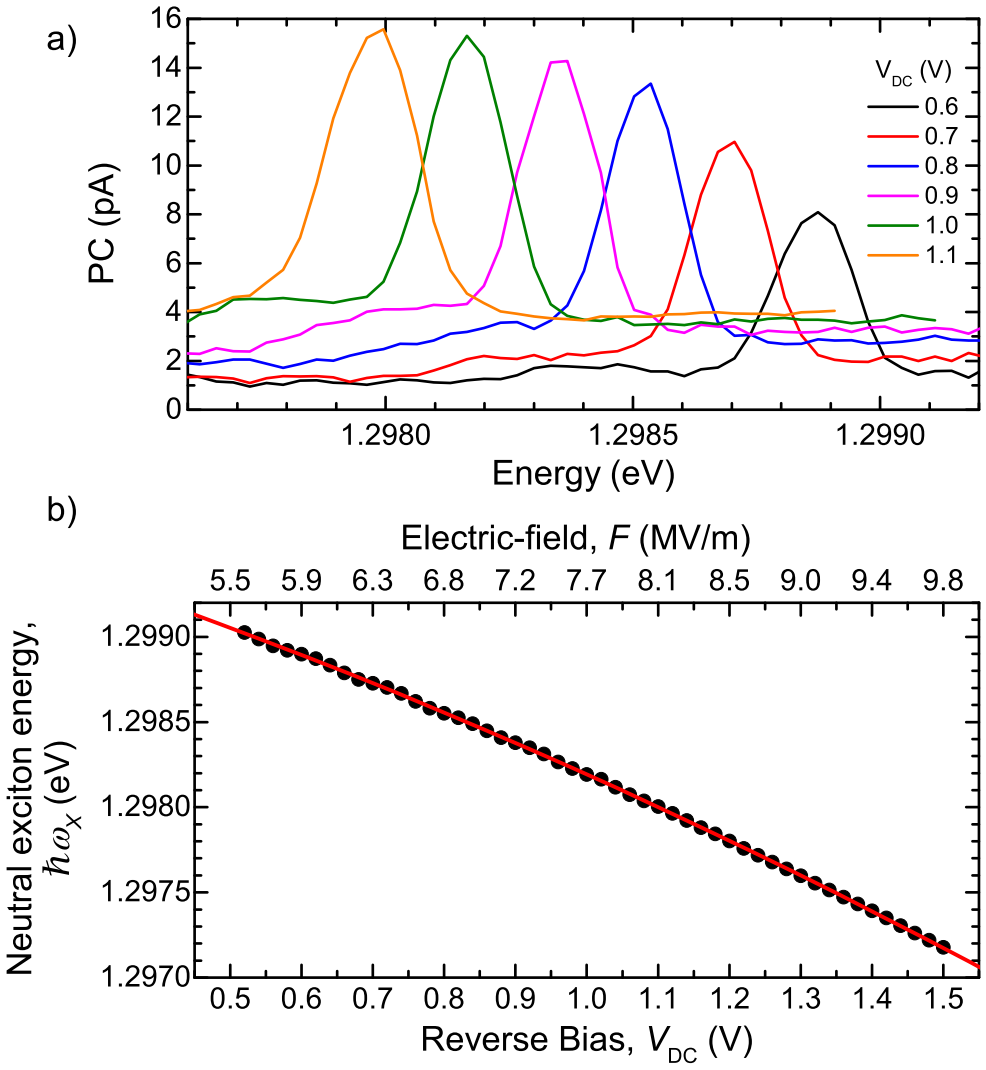

Figure 4.8: (a) Example voltage-dependent PC spectra showing the shift in energy and change in amplitude of the neutral exciton peak. (b) The energy of the peaks from a complete range of measurements that are summarized in (a) are plotted as a function of voltage to show the DC Stark shift. The red curve is a fit to eq. 2.3.

Fitting the data to eq. (2.3) yields a permanent electric dipole moment $p = -1.76 \pm 0.008 \times 10^{-4}$ eV m/V and polarizability $\beta = -1.68 \pm 0.005 \times 10^{-5}$ eV m^2/V^{-2} for this QD. These values are typical for the dots in this sample and over the voltage range used in experiments ($0.6-1.2$ V) can be approximated as a linear gradient of $\sim 1-2$ meV/V.

Chapter 5

Enhanced photocurrent readout for a quantum dot qubit by bias modulation

5.1 Introduction

Photocurrent detection is a useful technique for coherent control control schemes, as it allows the exact occupancy of the QD to be observed directly, including information about the spin state of carriers, which is determined by the optical selection rules. Since photocurrent does not require the collection of light emitted by the sample, resonant excitation can be easily used without the complcations associated with removing the excitation laser from the signal for resonance fluorescence experiments. For a QD embedded in a diode structure under pulsed excitation, the contribution to the photocurrent is ideally one electron-hole pair per π-pulse [51]. If this could be achieved, then such a device could potentially be used as an optically-triggered single electron source.

Motivation

In practice the proportion of the electron-hole pair that is converted into a measurable photocurrent is less than 1 and this fraction defines the photocurrent detection efficiency, η. The photocurrent for a π-pulse ($PC(\pi)$) is ideally equal to $T_{\text{rep}}^{-1} \times e$, where T_{rep} is the laser pulse repetition period (13.1 ns) and e is the elementary electronic charge. Thus the detection efficiency is defined by eq. (5.1) and the amplitude of a ideal π-pulse in a PC spectrum should be 12.2 pA.

$$\eta = \frac{PC(\pi)}{T_{\text{rep}} \times e} \tag{5.1}$$

5.1.1 Electron and hole tunneling scheme

To understand the factors that reduce the photocurrent detection efficiency, consider the states of the system, as shown in fig. 5.1, with the competing relaxation pathways indicated by the arrows. In this scheme the electron tunneling rate is considered to be much faster than the hole tunneling rate so the system is shelved in the hole ($|\mathrm{h}\rangle$) state if the electron tunnels before radiative recombination takes place. Non-radiative recombination processes are not considered here, for simplicity.

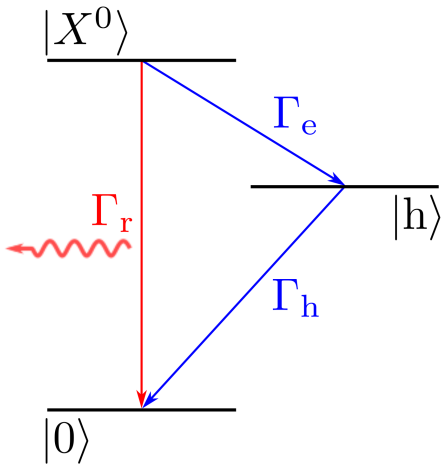

Figure 5.1: Electron and hole tunneling scheme. There are two possible pathways for the system to return to the ground state, following the population inversion by the absorption of a laser pulse. The first of these is radiative recombination, with rate Γ_r, secondly the electron and then the hole can tunnel out of the dot with rates Γ_e and Γ_h, respectively.

In practice, there are three factors that limit the photocurrent detection efficiency. Firstly, intensity damping reduces the population inversion [93]. Secondly, there is competition between radiative recombination and electron tunneling rates [35]. Thirdly, the heavy-hole tunneling rate can be slower than the repetition frequency of the laser [64,119] (T_rep^{-1}), leading to Pauli blocking when the next pulse arrives. For an optimized repetition rate, the maximum photocurrent is limited to $\sim e\Gamma_\mathrm{h}$, where Γ_h is the hole tunneling rate. The second and third factors (radiative recombination and slow hole tunneling) can be overcome by increasing the bias voltage, as this increases the electron and hole tunneling rates. However, this comes at a cost to the coherent lifetime T_X^1 of the photo-generated exciton, which is limited by the fastest (in this case electron) carrier tunneling rate. Hence high photocurrent signals are incompatible with a long exciton coherence times.

In this chapter, experimental results are presented that demonstrate the use of a time-varying bias voltage to overcome the trade-off between photocurrent detection efficiency and the carrier tunneling times that limit the coherence of both the exciton and hole spin. The work presented in this chapter was summarized in the following

publication: *Appl. Phys. Lett,* **102,** 181108 (2013).

5.1.2 Voltage modulation scheme

To illustrate the principle, consider the scenario of a square-wave modulation applied to the QD photodiode, which switches between reverse voltages V_{low} and V_{high}. This scheme is depicted in fig. 5.2.

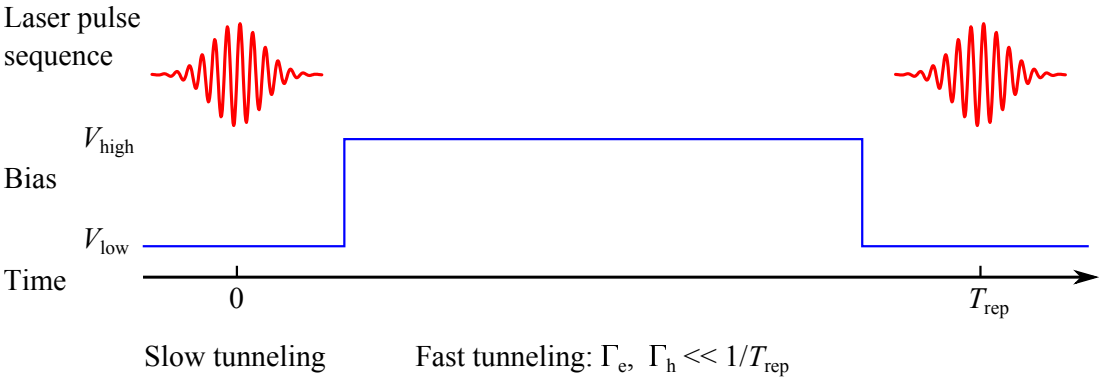

Figure 5.2: Voltage modulation scheme. In the ideal case, a square waveform bias is applied to the QD photodiode, switching between low and high voltages (V_{low} and V_{high}, respectively).

During optical manipulation, the bias is low, leading to low tunneling rates $\Gamma_{\text{e,h}}(V_{\text{low}})$ and hence higher coherence times. Afterwards, the tunneling rates are increased to $\Gamma_{\text{e,h}}(V_{\text{high}})$, sweeping the carriers from the QD ready for the next laser pulse sequence and generating a large photocurrent. The hole tunneling rate $\Gamma_{\text{h}}(V_{\text{low}})$ acting on the QD during optical control, and the maximum photocurrent signal $\sim e\Gamma_{\text{h}}(V_{\text{high}})$ are decoupled, overcoming the trade-off. To demonstrate the principle, a simpler experiment using a cosine modulation is presented. The reverse bias applied to the QD is described by the following sinusoidal function:

$$V(t, \phi) = V_{\text{DC}} + V_{\text{AC}} \cos(2\pi t/T_{\text{rep}} - \phi), \tag{5.2}$$

where t is the time after the arrival of the laser pulse, ϕ is the phase and V_{AC} is the amplitude of the modulation. The sinusoidal voltage is easier to apply in experimental conditions than a square wave due to the lower bandwidth required to generate a sinusoidal voltage and then transmit it to the photodiode device.

5.2 DC bias: determination of radiative recombination rate

In order to extract the electron tunneling rates from the t_1 exponential constants in eq. (4.2), the radiative recombination rate Γ_r needed to be determined. This was achieved by evaluating the amplitude of the neutral exciton peak for a π-pulse in a series of voltage-dependent spectra. The photocurrent detection efficiency, η was calculated for each peak according to eq. (5.1). These values are plotted as a function of bias voltage in fig. 5.3. A rate equation model based on the system shown in fig. 5.1 is used to calculate the detection efficiency, according to eq. (5.3).

$$\eta(V) = \Big(1 - \exp(-\Gamma_h(V)T_{rep})\Big) \times \frac{\Gamma_e(V)}{\Gamma_r + \Gamma_e(V)} \tag{5.3}$$

Here, the first term $\Big(1 - \exp(-\Gamma_h(V)T_{rep})\Big)$ describes the probability that the hole has tunneled out of the dot when the next laser pulse arrives and the second term, $\frac{\Gamma_e(V)}{\Gamma_r+\Gamma_e(V)}$, gives the probability that the exciton decays by electron tunneling rather than radiative recombination. A range of values of Γ_r were used to deduce the corresponding electron tunneling rates. For each value of Γ_r, the electron tunneling rate was extracted according to $\Gamma_e = 1/t_1 - \Gamma_r$, as described above. The detection efficiency, η was then calculated by eq. (5.3) as a function of voltage. These are shown as the curves in fig. 5.3. The R^2 values were calculated for each curve for the experimental data points, as shown in the insert to fig. 5.3. A radiative recombination lifetime of $1/\Gamma_r = 400 \pm 100$ ps was finally selected as this is where R^2 is maximized and the best fit to the data is observed. In the experiments presented here, the radiative recombination rate is assumed to be independent of voltage due to the relatively small shift in electric field over the voltage range used here [24]. It is worth noting that if a spectrometer is available then a more straightforward method for measuring Γ_r is to use correlated single photon counting [92], where the intensity of a single emission line is time-resolved with an avalanche photodiode. The results in ref. [92] give values of Γ_r in the range 1/1000 ps - 1/400 ps for the neutral exciton transition of QDs emitting at ∼1.3 eV, in agreement with the value obtained in this work.

At $V_{DC} =\sim 0.525$ V a discrepancy is observed between the traces and the data points in fig. 5.3. The model predicts a smooth curve with a gradual reduction of η with decreasing bias. In the experimental data, a discrete step is observed, with zero signal observed below 0.525 V. This is attributed to the QD reaching a charging threshold at low bias.

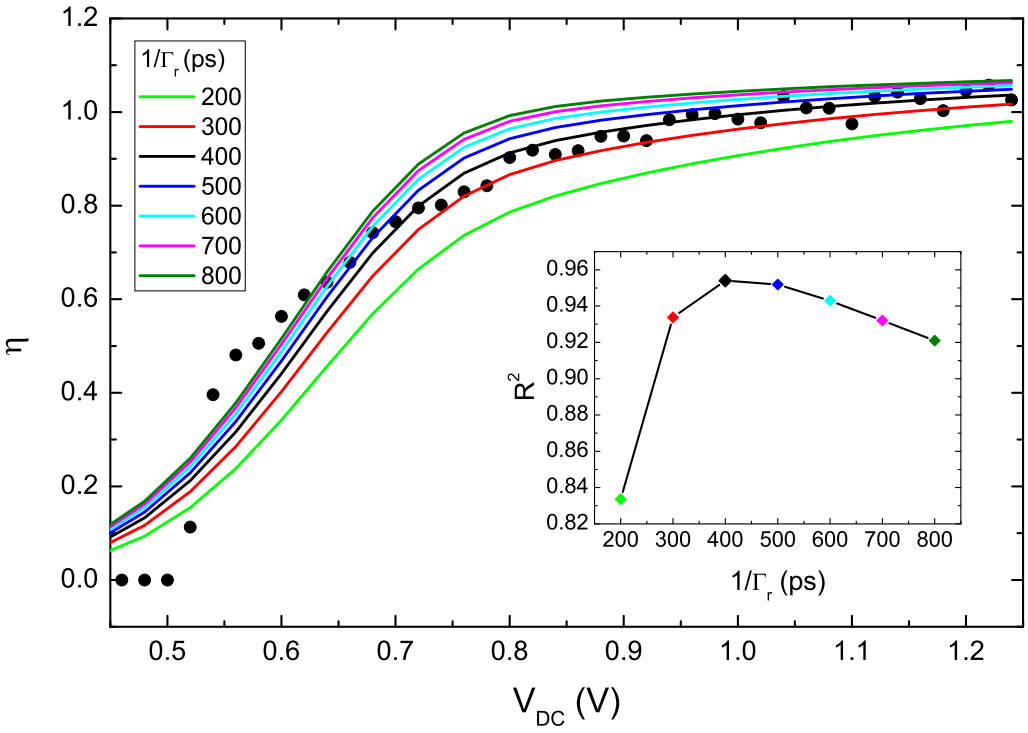

Figure 5.3: Determination of radiative recombination rate, Γ_r. The data points are the same as in fig. 5.7 (a) and the curves are calculated voltage-dependent values for η for a range of Γ_r values. The insert shows the R^2 value for each of the curves in the main figure when fitted to the data points over the entire plotted range. The best fit is obtained when $1/\Gamma_r = 400$ ps.

5.3 Application of AC bias to sample

5.3.1 Generation of synchronized AC voltage

AC modulation circuit

The circuit is adapted from the design used by de Vasconcellos *et al* [121] to apply a high-frequency modulation to a QD in order to perform electrical control of an exciton. The laser output is monitored with a photodiode inside the laser casing. This signal is spectrally filtered to remove higher harmonics and amplified to be strong enough to trigger a function generator. The system for generating an AC voltage synchronized with the laser pulses is presented in fig. 5.4. Before connecting to the sample, the AC voltage is offset by a DC voltage (V_{DC}) using a broadband bias-tee. The function generator allows direct control of the amplitude (V_{AC}, from eq. (5.2)) of the output. The phase, ϕ, of the sine wave can be determined by setting the delay between the trigger and the output signal on the function generator. Details of the signal filtering and amplification stage immediately after the laser photodiode are shown in fig. B.1 in Appendix B.

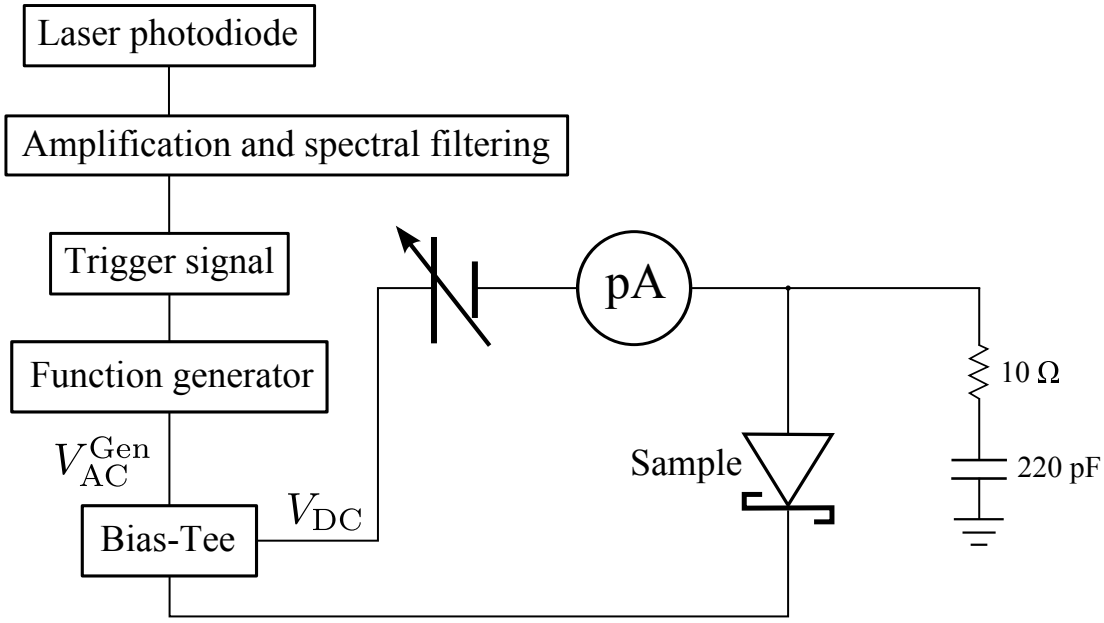

Figure 5.4: The output from the circuit in fig. B.1 is used as the trigger signal for the function generator, producing the output waveform, V_{AC}^{Gen}. The resistor and capacitor are necessary termination electronics to reduce noise in the measured photocurrent.

Figure 5.5 (a) shows typical oscilloscope traces of the laser photodiode output used as an input for the filter circuit, and the resulting synchronized AC-voltage applied to the device.

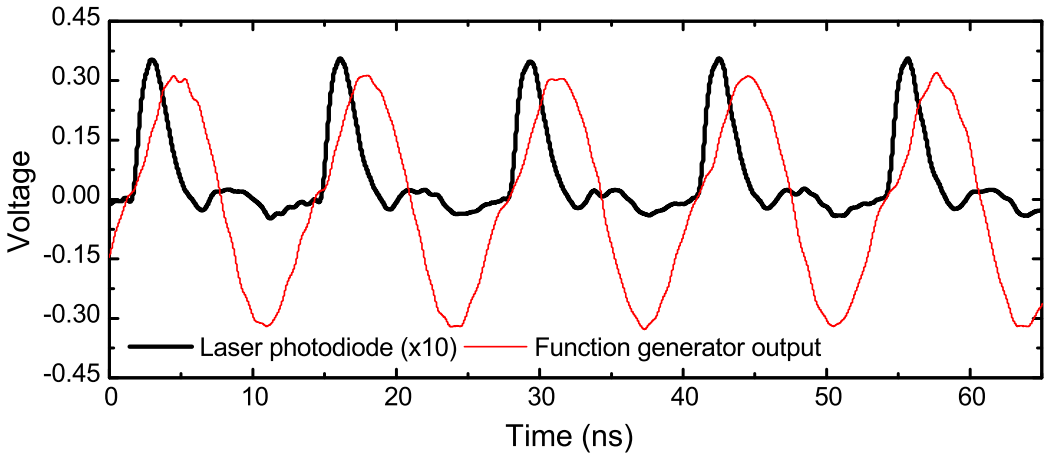

Figure 5.5: Oscilloscope traces of laser photodiode output and generated AC waveform. The laser photodiode output voltage has been amplified by a factor of 10 for clarity.

5.3.2 Observation of AC-modulated QD peak position

Figure 5.6 (a) presents timing diagrams of the laser pulse with respect to the AC-voltage waveform described in eq. (5.2) for the cases where the AC phase, ϕ is 0 and π.

To confirm that an AC voltage is applied to the QD, the energy shift of the neutral exciton peak is measured as ϕ is varied. For reference, a spectrum with only a DC bias of $V_{\mathrm{DC}} = 0.8$ V, (*i.e.* $V_{\mathrm{AC}} = 0$ V) is presented in fig. 5.6 (b). By applying an additional AC-voltage of $V_{\mathrm{AC}} = 0.23$ V, the photocurrent peak is shifted by the Stark effect, according to eq. (2.3). The energy shift is dependent on the phase, with the extreme energy shifts achieved for $\phi = 0$ and $\phi = \pi$, as presented in fig. 5.6 (b). When $\phi = \pi$, $V(0, \pi)$ is at its minimum value, shifting the peak to higher energy compared to the DC case, with $V_{\mathrm{AC}} = 0$. The opposite is true for $\phi = 0$: the peak is shifted to lower energy. The voltage ($V(0, \phi)$) applied to the QD at the time of arrival of the laser pulse is deduced from the energy of the photocurrent peak using the quantum-confined Stark-shift measured for DC voltages [122]. As shown in fig. 5.6 (c), the deduced voltage applied on arrival of the laser pulse, $V(0, \phi)$ oscillates as a function of phase ϕ with a period of 13.1 ± 0.3 MHz, identical to T_{rep}, confirming that the AC-voltage is effectively applied to the QD.

To measure the transfer of the applied AC-voltage to the QD, V_{AC} is extracted from the fit presented in fig. 5.6 (c) and plotted as a function of the amplitude of the AC voltage specified by the function generator, $V_{\mathrm{AC}}^{\mathrm{Gen}}$, in fig. 5.6 (d). From the gradient, it is deduced that 92% of the applied voltage modulation amplitude is transferred to the QD, suggesting that impedance matching is excellent.

An estimate of the RC response time (T_{RC}) of the sample is obtained by modelling the device as two parallel-plate capacitors in series, representing the 75 nm AlGaAs layer and combined 155 nm GaAs layers of the wafer. The area (A) of the device is calculated as 150 μm $\times$ 250 μm $= 3.75 \times 10^{-8}$ m^2. The capacitance of each layer, i, is calculated as $C_i = \epsilon_r \epsilon_0 A / t_i$, where ϵ_r is the relative permittivity of the material (12.05 for AlGaAs and 12.9 for GaAs), ϵ_0 is the permittivity of free space and t_i is the thickness of layer i. The total capacitance is therefore 18 pF. Multiplying the total capacitance by the impedance of the function generator (50Ω) gives an estimate for the value of T_{RC} to be 0.9 ns. This RC time gives a cut off frequency of the device as $1/(2\pi T_{\mathrm{RC}}) = 177$ MHz. The calculated diode RC time allows the 76.2 MHz voltage modulation to be applied successfully, but is not fast enough for the third harmonic (and therefore a 76.2 MHz square wave) to be applied to the QD. Photodiodes that have been designed for a high-frequency response, by reducing the diode area, for example those used by de Vasconcellos *et al* [121], allow the application of signals with frequencies >10 GHz to the QD.

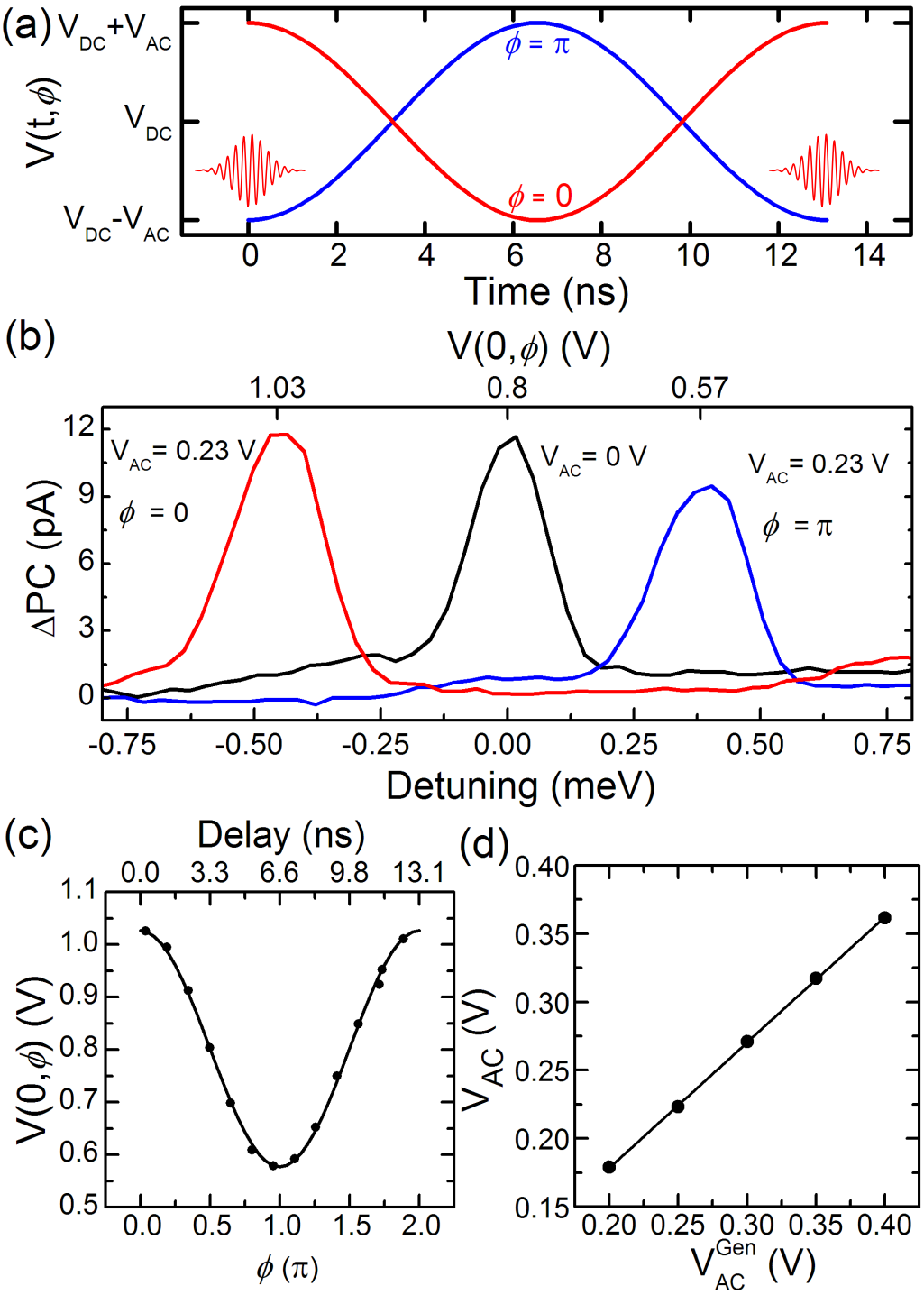

Figure 5.6: AC modulation of QD exciton transition. (a) The time-varying bias, $V(t, \phi)$ is shown with respect to laser pulse arrival, as indicated by the red shaded pulses. (b) The neutral exciton peak in photocurrent spectra with $V_{\mathrm{DC}} = 0.8$ V and $V_{\mathrm{AC}} = 0.23$ V for $\phi = \pi$ and $\phi = 0$, compared with the equivalent peak in a reference spectrum with $V \equiv V_{\mathrm{DC}} = 0.8$ V and $V_{\mathrm{AC}} = 0$ V. Background PC is subtracted from all spectra. (c) The reverse bias on pulse arrival $V(0, \phi)$ is plotted as a function of ϕ. (d) The AC voltage amplitude (V_{AC}) as a function of the voltage output by the function generator ($V_{\mathrm{AC}}^{\mathrm{Gen}}$), yielding a gradient of 0.918 ± 0.004.

5.4 Effect of voltage modulation on photocurrent detection efficiency

5.4.1 Measurement of detection efficiency with applied AC bias

In this section, the DC bias that is applied to the dot is modulated by the sinusoidal voltage waveform, described by eq. (5.2), and the effect on the detection efficiency is evaluated. In order to make a comparison with the detection efficiencies for DC biases, a voltage-dependent series of photocurrent π-pulse spectra were recorded with the application of the AC modulation of a defined phase, ϕ, and amplitude V_{AC}. The amplitude of these spectra was then converted into the equivalent detection efficiency, η, using eq. (5.1), as in the DC only bias case. To make a direct comparison of the detection efficiencies achieved for particular values of the electron and hole tunneling rates experienced by the QD during optical manipulation, the voltage applied on arrival of the laser pulse ($V(0,\phi)$) is deduced form the quantum confined Stark shift shown in fig. 4.8. In fig. 5.7, the detection efficiencies achieved using a DC-only bias, and with the AC-modulation scheme with $V_{\mathrm{AC}} = 0.23$ V and $\phi = 0$ and π are plotted as a function of $V(0,\phi)$.

The detection efficiency is defined in eq. (5.1), with a photocurrent of 12.2 pA corresponding to one electron per pulse, *i.e.* $\eta = 1$. In the case of a DC bias, $V_{\mathrm{AC}} = 0$ and the detection efficiency only reaches unity when V_{DC} is greater than 1.00 V. For V_{DC} below this value, due to slow hole tunneling, there is a high probability that the dot is occupied by a hole on arrival of the next pulse, preventing absorption of the laser pulse due to the Coulomb-shift in the exciton absorption energy. A sharp threshold is observed at $V_{\mathrm{DC}} \approx 0.52$ V, below which the photocurrent amplitude is negligible. The threshold is attributed to charging of the dot by a single electron, suppressing the neutral exciton transition [123].

The detection efficiency is enhanced when $V_{\mathrm{AC}} \neq 0$, $\phi = \pi$ for $V(0,\pi) < 0.8$ V, increasing the bias range where a clear signal can be measured. Here the laser pulse arrives at the minimum in the applied voltage. Afterwards, the hole tunneling rate is increased via the increasing reverse voltage. The hole is swept from the QD ready for the next laser pulse to be absorbed, thereby increasing the detection efficiency. The photocurrent is suppressed for all bias values below 1.2 V when $\phi = 0$. Here the laser pulse arrives at the maximum in the applied reverse voltage. Afterwards, the hole tunneling rates are decreased, increasing the probability that the hole remains in the dot when the next laser pulse arrives, thereby blocking absorption, and hence reducing the photocurrent.

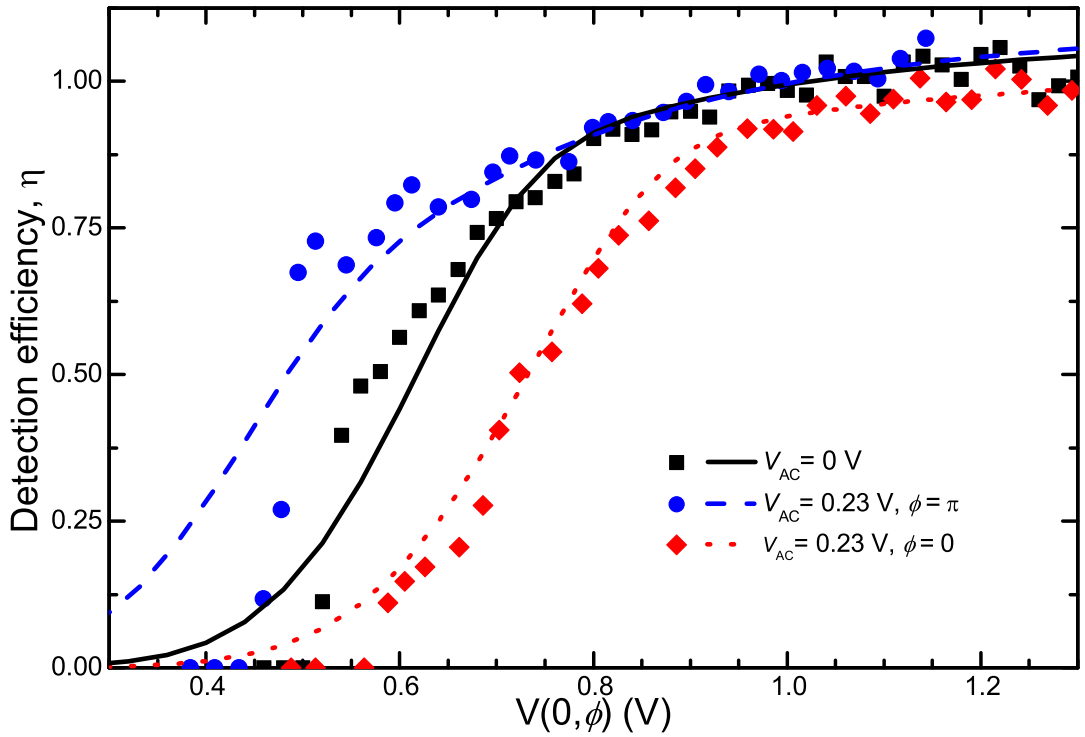

Figure 5.7: Detection efficiency with applied AC bias. The detection efficiency (η) of the neutral exciton peak in PC spectra as a function of instantaneous voltage at pulse arrival, $V(0,\phi)$. Values of η extracted from a series of voltage-dependent spectra with a DC-only bias are presented for comparison. The PC is enhanced by the AC modulation for the same $V(0,\phi)$, with $V_{\mathrm{AC}} = 0.23$ V and $\phi = \pi$.

As an illustration of the improvement in the coherence times that can be achieved by using the AC-modulation scheme, consider that to achieve a detection efficiency of $\eta = 0.68$, a DC bias of 0.67 V is required. However, by applying an AC-modulation ($V_{\mathrm{AC}} = 0.23$ V $\phi = \pi$), $V(0,\pi)$ is reduced by 0.1 V to 0.57 V. The corresponding electron and hole tunneling rates for equivalent DC biases of 0.67 and 0.57 V are found in fig. 5.1. The reduced voltage when the pulse is absorbed means that during coherent optical control, the carrier tunneling times are $\Gamma_{\mathrm{e}}^{-1} = 200$ ps and $\Gamma_{\mathrm{h}}^{-1} = 20$ ns, compared to 120 ps and 7 ns for the DC-only bias. In principle, the effective coherence times of the exciton and the hole spin have been approximately doubled at no cost to the detection efficiency. Alternatively, a detection efficiency of 50% can be achieved for an effective hole tunneling rate of 100 ns, which would be impossible for a DC-only bias.

5.4.2 Optimum amplitude of modulation

To determine if increasing the amplitude of the AC modulation would increase the enhancement to the detection efficiency, measurements were carried out as a function of V_{AC}. The principle of the measurement is that when $\phi = \pi$, there would be a greater

change in the carrier tunneling rates if V_{AC} was increased. Therefore there would be a higher photocurrent signal for the same bias ($V(0,\pi)$). The detection efficiency is presented in fig. 5.8 for a range of V_{AC} values.

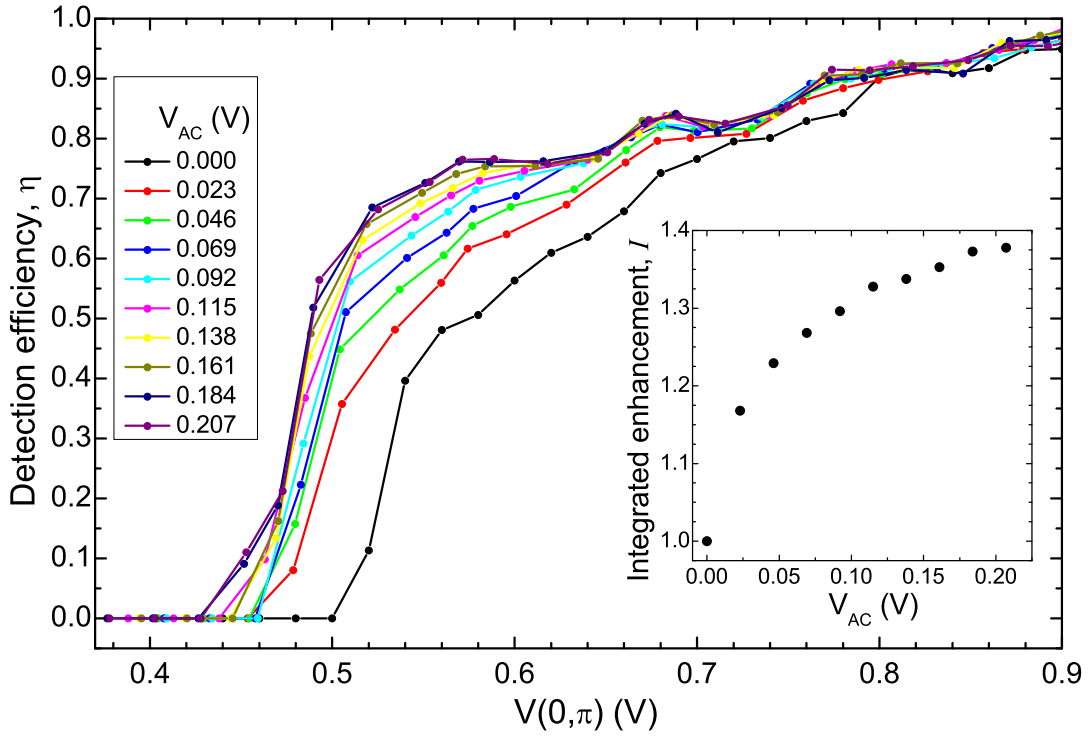

Figure 5.8: The detection efficiency as a function of $V(0,\pi)$ is presented for a range of modulation amplitude V_{AC} values. In all cases $\phi = \pi$. The inset shows the integrated enhancement to the detection efficiency over the bias range $0 \leq V(0,\pi) \leq 0.8$ V as a function of V_{AC}. The lines are a guide to the eye.

To quantify the enhancement to the detection efficiency, the integrated efficiency, I, is calculated by eq. (5.4):

$$I = \frac{\int_0^{0.8\ \mathrm{V}} \eta_{\mathrm{AC}}(V)\,\mathrm{d}V}{\int_0^{0.8\ \mathrm{V}} \eta_{\mathrm{DC}}(V)\,\mathrm{d}V}, \tag{5.4}$$

where $\eta_{\mathrm{AC}}(V)$ is the detection efficiency when $V_{\mathrm{AC}} \neq 0$ and $\eta_{\mathrm{DC}}(V)$ is the detection efficiency for an unmodulated DC bias. The integrated efficiency is plotted as a function of V_{AC} in the insert in fig. 5.8 and shows a diminishing return when V_{AC} is increased. Once the hole has been fully removed from the dot, hole-tunneling will no longer be the limiting factor for the detection efficiency. Also, at this value of V_{AC}, $\Gamma_{\mathrm{e}} \gg \Gamma_{\mathrm{r}}$, as shown in fig. 4.5. Further increasing V_{AC} would be expected to cause I to asymptotically approach a maximum value of approximately 1.38, where η is maximized for the largest possible range of $V(0,\phi)$.

5.4.3 Rate equation model

To confirm the understanding of the AC-modulation scheme, the detection efficiency is calculated and presented as the curves in fig. 5.7 (a). The rate equation model is illustrated in fig. 4.5 (b) and considers the population of the crystal ground, exciton and hole states [64]. The carrier tunneling rates $\Gamma_{\mathrm{e,h}}(V)$ depend on the instantaneous applied voltage $V(t,\phi)$, and the calculated photocurrent detection efficiency is given by eq. (5.5):

$$\eta = f(\Gamma_{\mathrm{h}}) \times g(\Gamma_{\mathrm{e}}), \tag{5.5}$$

where

$$f(\Gamma_{\mathrm{h}}) \approx 1 - \exp\left(-\int_0^{T_{\mathrm{rep}}} \Gamma_{\mathrm{h}}(t)\,\mathrm{d}t\right) \tag{5.6}$$

and

$$g(\Gamma_{\mathrm{e}}) = \int_0^{T_{\mathrm{rep}}} \Gamma_{\mathrm{e}}(t) \exp\left(-\int_0^{t} (\Gamma_{\mathrm{r}} + \Gamma_{\mathrm{e}}(\tau))\,\mathrm{d}\tau\right) \mathrm{d}t. \tag{5.7}$$

Here, $f(\Gamma_{\mathrm{h}})$ is the probability that the hole no longer remains in the QD when the next pulse arrives and $g(\Gamma_{\mathrm{e}})$ is the probability that the exciton decays via electron tunneling instead of radiative recombination. $\Gamma_{\mathrm{h}}(t)$ and $\Gamma_{\mathrm{e}}(t)$ are calculated from the fitted values in fig. 4.5. A full derivation of eqs. (5.6 and 5.7) is provided in Appendix A. The detection efficiency predicted by the model closely matches the experimental data for higher voltages ($V(0,\phi) > 0.6$ V), as can be seen in fig. 5.7. However, the model does not explain the threshold behaviour observed in the photocurrent at lower bias, which, as explained above, is related to a single electron charging threshold. In the case where only a DC bias is applied to the sample, as described in § 5.2 the rate equations are no longer themselves time-dependent and eq. (5.5) reduces to eq. (5.3).

5.4.4 Enhancement of Rabi oscillation amplitude

To test that the AC-modulation does not degrade the contrast of an exciton Rabi rotation, Rabi rotations of the neutral exciton transition for DC-only bias and for AC modulation are compared in fig. 5.9. For both traces, $V(0,\phi) = 0.530$ V, as this provides the largest increase in detection efficiency η, compared with the DC-only bias situation as can be seen in fig. 5.7. The amplitude of the AC-modulated Rabi-rotation is increased to 8.4 ± 0.3 pA compared to the DC case 3.3 ± 0.2 pA for a pulse-area of π. Additionally, the contrast of the rotations defined as $(PC(\pi) - PC(2\pi))/PC(\pi)$ for the case with AC modulation is 0.83 ± 0.06 and 0.70 ± 0.1 for the DC-only bias. As the two contrasts are similar within experimental error, it is inferred that on the timescale of the laser pulse, no additional dephasing is introduced by the AC voltage and the voltage modulation scheme successfully improves the coherent readout efficiency for the Rabi oscillation.

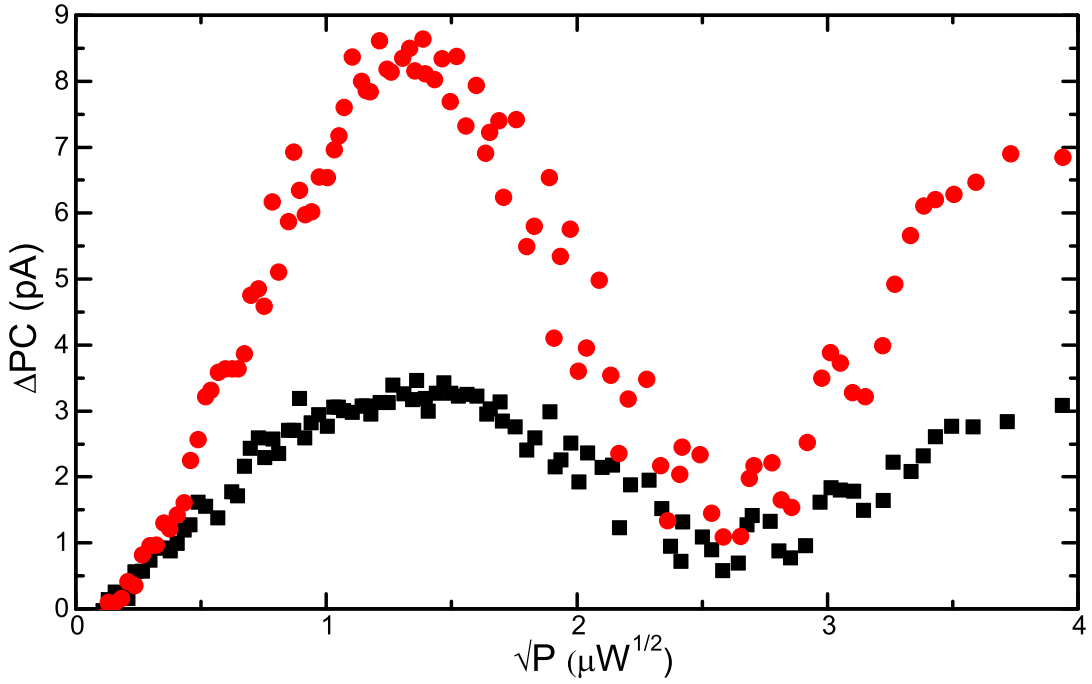

Figure 5.9: Rabi rotations of the neutral exciton transition, for a DC bias of 0.530 V (■) and with AC modulation ($V_{\mathrm{DC}} = 0.842$ V, $\phi = \pi$ and $V_{\mathrm{AC}} = 0.312$ V) (●). P is the laser power transmitted to the sample. A linear background PC with laser power is subtracted from the data.

5.5 Conclusions

In summary, this chapter demonstrates a voltage modulation scheme for overcoming the inherent limit for coherent control experiments using the photocurrent technique, where the detection efficiency and coherence times are both inversely determined by the carrier tunneling rates. In this scheme, coherent control is performed at low reverse bias where exciton coherence times are long. Afterwards, the bias is increased to sweep the carriers from the dot to be detected as a photocurrent, thus achieving high coherence during manipulation with a high readout efficiency. A possible further direction for this technique is to use a time-varying electric field for rapidly switching between non-degenerate photonic crystal waveguides, by modulating the Stark shift of a QD emitter coupled to both waveguide modes [124].

Chapter 6

Phonon-assisted population inversion of a single Quantum Dot

6.1 Introduction

Motivation

Exciton Rabi rotations have been studied extensively in our group, as our unique experimental set up allows us to reach very high pulse areas. In particular, the damping of the rotations due to the interaction of the quantum dot exciton with acoustic phonons propagating through the GaAs lattice has been the subject of several experiments [93–95]. In this chapter a new regime is investigated, where the phonon sideband of the exciton transition is strongly driven with the laser, instead of the laser being resonant with the transition. In this case, it is possible to create an exciton population as a result of the interaction with phonons. The presence of the phonons is actually useful in this scheme as it allows robust state preparation by using an off-resonant laser.

This work is currently under review for publication in *Physical Review letters* and the manuscript can be found on the ArXiv [125].

It is a basic tenet of laser physics that to achieve a population inversion of a two-level system, the duration of the laser pulse $\Delta\tau$ must be less than the coherence time T_2 of the excited state. In the incoherent regime, where $\Delta\tau > T_2$, at best the pulse can only drive the system to the transparency point, where the populations of the upper and lower levels are equal [126]. However, if both levels of a two-level system are coupled to a vibrational continuum, it has been predicted that the dressed states of the system can come into thermal equilibrium with the boson bath [127], providing an additional route to inversion. Excitons in semiconductor quantum dots reside in a solid lattice, and therefore can couple to the optical and acoustic phonons in the crystal. In

particular, the coupling to longitudinal acoustic (LA) phonons provides a mechanism to thermalize the dressed states and explore these effects. A recent comprehensive review of the field of phonon-assisted exciton generation can be found in Ref. [128].

The possibility of creating population inversion in QDs through phonon coupling was first investigated for microwave-driven point-contact dots [129] several years ago. More recently, it has been demonstrated that the conditions for population inversion can be met via a microwave analogue of the Raman effect [130,131]. In 2013, independent theoretical work by Glässl [132] and Hughes [133] has indicated that similar effects should be possible for optically driven excitons. The underlying mechanism is the coupling of the excitons to LA phonons through the deformation potential [134], which generates sidebands in the excitonic spectra that can be observed in four-wave mixing [135] and resonance fluorescence experiments [136], and also through off-resonant coupling of excitons to nano-cavities [137,138]. In a strong driving field regime evidence for phonon induced relaxation between optically dressed states is observed in the intensity damping of Rabi rotations and renormalization of the Rabi frequency [93,94], and more recently in adiabatic rapid passage experiments [139]. In this chapter, evidence is presented for the population inversion of the excitonic two-level system in a regime where the dephasing time is shorter than the laser pulse duration, which in turn is shorter than the lifetime of the exciton.

Collaboration with Universität Bayreuth

The work in this chapter was carried out in collaboration with M. Glässl, A. J. Barth and V. M. Axt at *Institut für Theoretische Physik III, Universität Bayreuth*, to provide theoretical support for our experimental results. In the theoretical treatment, a numerically correct path integral method [140] is used to calculate the final exciton population, as in the recent work by Glässl *et al.* The parameters used in the calculations were chosen to closely match our experimental conditions and result in excellent agreement with the experimental results. The theoretical results are included here with permission.

6.1.1 Photon-dressed QD states

It is convenient to use the dressed states interpretation of the QD-laser interaction to describe the physical mechanism whereby the population inversion is established. In this picture, we consider the QD interacting with an optical field, with photon energy $\hbar\omega$. The action of the laser is to manipulate the dressed state admixture, depending on the laser Rabi frequency Ω_R and detuning Δ. The transformation of the bare QD states into the photon-dressed states is summarized in fig. 6.1 for a positively detuned laser ($\Delta > 0$) and discussed in detail in § 6.1.1.

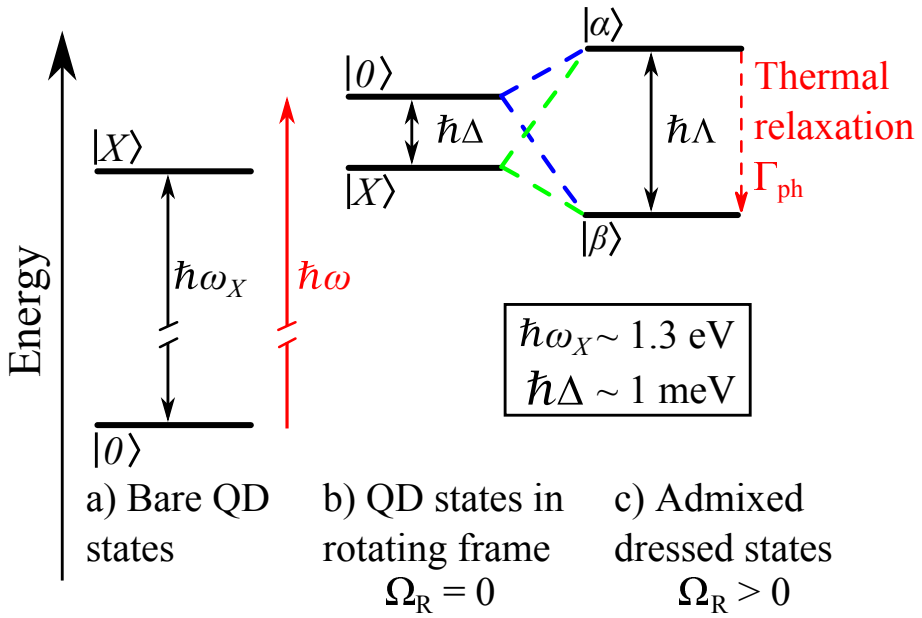

Figure 6.1: (a) Bare QD exciton $|X\rangle$ and crystal ground state $|0\rangle$. (b) In the rotating frame of the laser, the bare states are split by the laser detuning $\hbar\Delta$ and for $\hbar\Delta > 0$ $|X\rangle$ is lower in energy than $|0\rangle$ (c) Optical mixing, due to nonzero Rabi frequency, of the states in (b) results in a pair of dressed states $|\alpha\rangle$ and $|\beta\rangle$, split by the effective Rabi energy, $\hbar\Lambda$.

The bandwidth of the laser is larger than the neutral exciton fine structure $\hbar\delta$, enabling the effectively degenerate exciton spin states to be selected by choosing the polarization to be circular. The QD system is therefore reduced to only two energy levels, consisting of the crystal ground state $|0\rangle$ and spin-polarized exciton $|X\rangle$, as shown in fig. 6.1 (a). The zero of energy is taken to be the energy of the Bare QD ground state $|0\rangle$, and only one optical transition is allowed, having energy $\hbar\omega_X$. The laser is detuned by $\Delta = \omega - \omega_X$ and a positively detuned laser is shown in fig. 6.1 (a) to address the $|0\rangle - |X\rangle$ transition. The QD states become coupled when the Rabi frequency is non-zero (*i.e,* when the laser is switched on), forming the final dressed states, $|\alpha\rangle$ and $|\beta\rangle$, which are split by an effective Rabi energy $\hbar\Lambda$ and have a composition that is an admixture of the bare QD states.

Dressed states Hamlitonian

The Hamiltonian for the system is written:

$$H = H_{\text{QD}} + H_{\text{int}}, \tag{6.1}$$

where the QD Hamiltonian is:

$$H_{\text{QD}} = \hbar\omega_X |X\rangle\langle X|, \tag{6.2}$$

and the light-matter interaction term H_{int} is given by:

$$H_{\text{int}} = \frac{\hbar\Omega_{\text{R}}\cos(\omega t)}{2}\left(|0\rangle\langle X| + |X\rangle\langle 0|\right) \tag{6.3}$$

where Ω_{R} is the bare Rabi frequency, defined in eq (2.5). In the $\{|0\rangle, |X\rangle\}$ basis, H is written:

$$\frac{\hbar}{2}\begin{pmatrix} 0 & \Omega_{\text{R}}\left(e^{i\omega t} + e^{-i\omega t}\right) \\ \Omega_{\text{R}}\left(e^{i\omega t} + e^{-i\omega t}\right) & 2\omega_X \end{pmatrix}. \tag{6.4}$$

We define the operator

$$H_1 = \hbar\begin{pmatrix} 0 & 0 \\ 0 & \omega \end{pmatrix}. \tag{6.5}$$

The system is described in the rotating frame of the laser by a new Hamiltonian, given by the following unitary transformation:

$$H' = e^{iH_l t/\hbar}(H - H_1)e^{-iH_1 t/\hbar}. \tag{6.6}$$

At a wavelength of 950 nm, the laser frequency ($\omega/2\pi$) is ∼315 THz, and the rotating wave approximation is made to remove this high frequency contribution ω. The new Hamiltonian H^{RWA} in matrix form is written:

$$H^{\text{RWA}} = \frac{\hbar}{2}\begin{pmatrix} 0 & \Omega_{\text{R}} \\ \Omega_{\text{R}} & -2\Delta \end{pmatrix}. \tag{6.7}$$

Dressed state eigenvalues and admixture

The eigenvalues of H^{RWA} are the energies of the final dressed states $|\alpha\rangle$ (E_+) and $|\beta\rangle$ (E_-), as given by:

$$E_\pm = \frac{\hbar}{2}\left(-\Delta \pm \Lambda\right), \tag{6.8}$$

where Λ is an effective Rabi frequency, calculated by:

$$\Lambda = \sqrt{\Omega_{\text{R}}^2 + \Delta^2}. \tag{6.9}$$

Due to the optical coupling of the bare states, the dressed states are an admixture of $|0\rangle$ and $|X\rangle$, as illustrated in fig. 6.1 (c). The admixture is determined by the instantaneous bare Rabi frequency $\Omega_{\text{R}}(t)$ and detuning Δ, as given by:

$$|\alpha\rangle = \sin(\theta)|0\rangle + \cos(\theta)|X\rangle \tag{6.10a}$$

$$|\beta\rangle = \cos(\theta)|0\rangle - \sin(\theta)|X\rangle, \tag{6.10b}$$

where θ is a admixing angle, given by:

$$\tan(2\theta) = -\Omega_{\text{R}}/\Delta, \quad 0 \leq 2\theta \leq 90^\circ. \tag{6.11}$$

Fig. 6.2 shows the energy of the dressed states $|\alpha\rangle$ and $|\beta\rangle$ as a function of $\hbar\Delta$ for $\hbar\Omega_{\mathrm{R}} = 1$ meV. The dressed states anticross when $\omega = \omega_X$, where they are split by the bare Rabi energy $\hbar\Omega_{\mathrm{R}}$. If Ω_{R} is zero, then the dressed states tend towards the uncoupled QD states, which are now split by $\hbar\Delta$. Increasing the detuning from the transition also reduces the value of θ, again leading to the dressed states being more purely $|0\rangle$ and $|X\rangle$ in character.

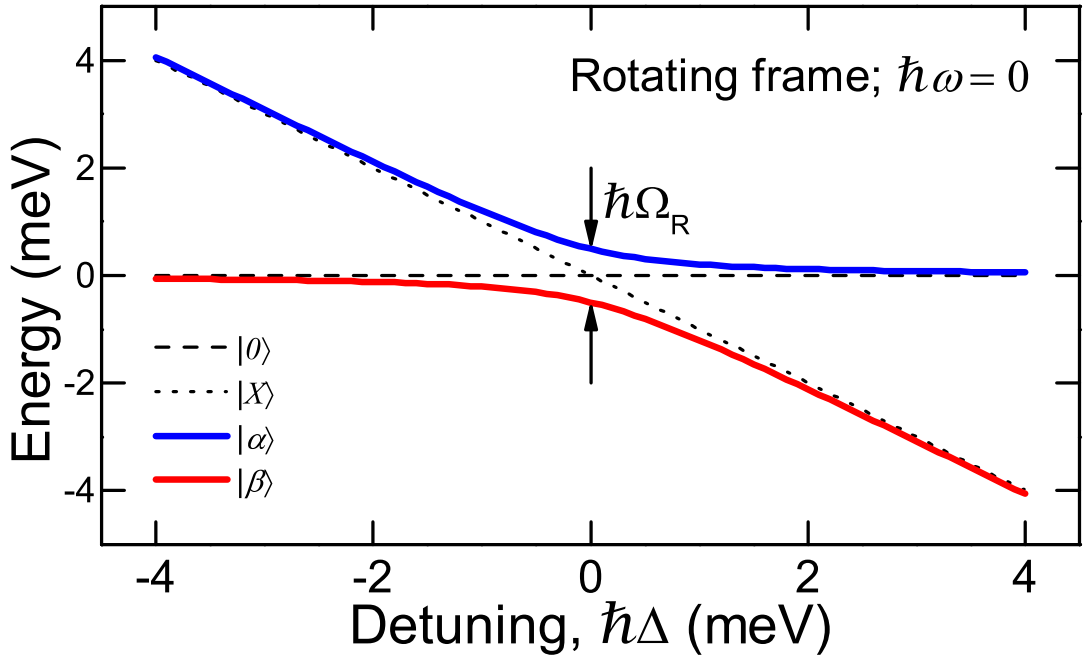

Figure 6.2: The photon-dressed QD state energies as a function of the laser detuning $\hbar\Delta$. The bare states $|X\rangle$ and $|0\rangle$ in the rotating frame of the laser are also displayed. Here $\hbar\Omega_{\mathrm{R}} = 1$ meV.

6.1.2 Phonon-assisted relaxation

The crucial reason for considering the dressed QD states is that as for positive detuning, $|\beta\rangle \to |X\rangle$ as $\hbar\Delta \to +\infty$, due to the photon energy exceeding the exciton transition energy. $|\beta\rangle$ is therefore mainly excitonic in character. If there is coupling to the phonon bath then thermal relaxation can occur between $|\alpha\rangle$ and $|\beta\rangle$, and since at $T = 4.2$ K, $\hbar\Omega_{\mathrm{R}} \gg k_{\mathrm{B}}T$, the long-time limit occupation of the system is approximately equal to a complete occupation of $|\beta\rangle$. Ultimately, the final exciton population is determined by the population that can relax into $|\beta\rangle$ during the pulse, which can exceed the population inversion threshold of 0.5 if the time-integrated relaxation rates are fast enough. Full details about the derivation of the phonon-assisted relaxation rate are beyond the scope of this work, but can be found in the supplementary material for ref. [93]. A brief summary is presented here. The Hamiltonian for the exciton-phonon interaction reads [134]:

$$H_{\mathrm{ph}} = |X\rangle\langle X| \sum_{\mathbf{k}} \left(g_{\mathbf{k}} \hat{b}^{\dagger}_{\mathbf{k}} + g^{*}_{\mathbf{k}} \hat{b}_{\mathbf{k}} \right), \tag{6.12}$$

where $\hat{b}^{\dagger}_{\mathbf{k}}$ and $\hat{b}_{\mathbf{k}}$ are the creation and annihilation operators for an LA phonon with wavevector $\mathbf{k}$ and $g_{\mathbf{k}}$ is the coupling strength for the exciton-phonon interaction. Eq. (6.12) acts as a perturbation to eq. (6.7). In the absence of the optical field, the interaction with phonons leads to non-exponential damping of the exciton dipole, as seen in four-wave mixing experiments [135]. If the system is optically driven, then the excitonic component of the dressed states couples to the phonon bath via the deformation potential. Thermal relaxation then occurs by the emission and absorption of phonons that are resonant with the effective Rabi frequency Λ.

There are three key factors that determine the phonon-assisted relaxation rate:

Mixing of bare QD states

The Hamiltonian for the interaction in eq. (6.12) only couples the excitoninc component of the dressed states admixture to the phonon bath. A greater overlap of the excitonic contributions of the wavefunctions for $|\alpha\rangle$ and $|\beta\rangle$ means that relaxation is more efficient.

Spectral dependence on the exciton-phonon interaction

The spectral dependence of the interaction strength is described by the function $J(\omega)$, which typically is proportional to ω^3 for low frequency driving, and has a Gaussian roll-off above a cut-off frequency, which is typically, $\sim$ 1-2 meV and corresponds to a phonon wavelength equal to the spatial FWHM of the carrier wavefunction (assuming equal electron and hole confinement energies and a spherically symmetric wavefunction). In § 6.4, we show that for our QD $J(\omega)$ takes the form of the sum of two Gaussian functions.

Thermal distribution of phonons

The phonon occupation is determined by Bose-Einstein statistics, giving a temperature-dependent term for the relaxation rate.

The relaxation rates can be estimated according to eq. (6.13), which is a function of the real part of the complex response function that describes the time-dependent exciton-phonon interaction [95].

$$\Gamma_{\mathrm{ph}} \approx \underbrace{\frac{\Omega_{\mathrm{R}}^2}{\Lambda^2}}_{\text{Excitonic overlap}} \times \underbrace{J(\omega)}_{spectraldensity} \times \underbrace{\coth(\hbar\Lambda/2k_{\mathrm{B}}T)}_{\text{Thermal phonon desnsity}}, \tag{6.13}$$

The rates given by eq. (6.13) overestimate the population of $|\beta\rangle$, and the expression is included for discussion only. For the calculated values presented in this chapter, the results of the path integral calculations are used, as they allow the model to be treated without any further approximations, giving a more accurate picture of the population transfer into the lower energy dressed state.

Effect of detuning on the exciton population

For resonant excitation, $\theta = 45°$, and the dressed states are an equal admixture of $|X\rangle$ and $|0\rangle$. The maximum exciton population (C_X) that can be established through relaxation is therefore 0.5, matching the level that fully damped Rabi oscillations reach, as in fig. 4.2. Detuning the pulse modifies the admixture and the final exciton population in the long time limit is given by eq. (6.14), which predicts a stationary inversion for $\Delta/\Lambda \approx 1$ and $\hbar\Lambda/2k_\mathrm{B}T \gg 1$ [132].

$$C_X(t=\infty) = \frac{1}{2}\left(1 + \frac{\Delta}{\Lambda}\tanh(\hbar\Lambda/2k_\mathrm{B}T)\right). \tag{6.14}$$

At high pulse areas, the effective Rabi splitting $\hbar\Lambda$ can be of the order of 1-2 meV, which is much greater than $k_\mathrm{B}T$ at $T = 4.2$ K. The equilibrium occupation of the two levels is therefore almost equivalent to the fully populated $|\beta\rangle$ state. For an 8.5π-pulse which is detuned by $\hbar\Delta = +1$ meV, eq. (6.14) predicts a value of $C_X(t=\infty) = 0.833$.

Time-dependence of relaxation

For pulsed excitation, as used in these experiments, the overall relaxation is limited by the timescale of the laser pulse. As the relaxation rates are dependent on the instantaneous Rabi energy, which in turn affects the admixing angle θ, they are dynamic in time following the Gaussian laser pulse shape. Fig. 6.3 (a) shows the temporal evolution of the energy of $|\alpha\rangle$ and $|\beta\rangle$ for an 8.5π-pulse that is detuned by $\hbar\Delta = +1$ meV. Before the pulse, the laser is off and the QD is unoccupied, as indicated by the "Start" label on the diagram. Thermalization of the dressed states is only possible when $\Omega_\mathrm{R}(t) > 0$, as otherwise only one state ($|\beta\rangle$) would have an excitonic component. Fig. 6.3 (b) shows the value of the admixing angle for the same pulse as (a).

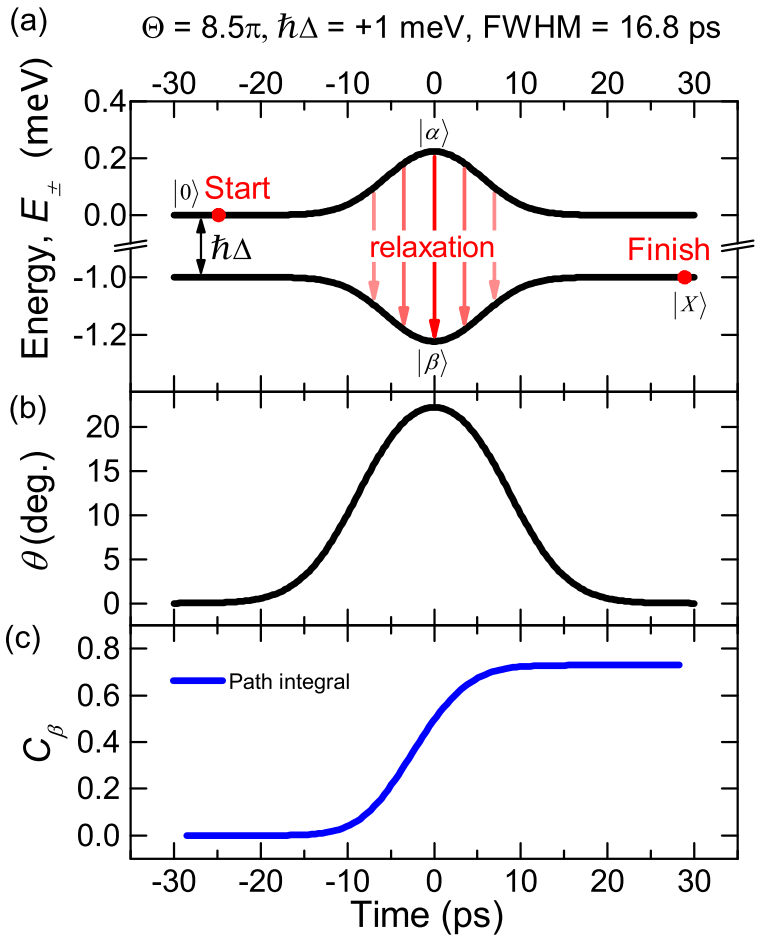

Figure 6.3: (a) The time-dependent energies of the dressed states during the pulse. Red arrows indicate the thermal relaxation pathway, with faster rates represented by darker arrows (b) The time-dependent admixing angle θ for the same pulse as (a). (c) The lower dressed state population is plotted vs time, as a result of path integral calculations.

The admixing angle is largest at the center of the pulse in time, as this is when the Rabi frequency is largest. Optimum relaxation rates are possible when, for intense pulses, the peak effective Rabi frequency approximately equals ω_c. To illustrate the speed of the relaxation, fig. 6.3 (c) shows the population of the lower energy dressed state as a function of time, as calculated directly from the path integral calculations. The path-integral approach leads to a more realistic prediction of the final value of C_β than eq. (6.13). The relaxation is fast enough that a maximum value of $C_\beta = 0.723$ is predicted to be reached during the pulse.

As the optical field is switched off at the end of the laser pulse, θ returns to zero, leaving the system with an exciton population equal to the final value of C_β. Fast phonon-assisted relaxation rates are also responsible for the damping of on-resonance driven Rabi osculations, as shown in fig. 4.2. An $n\pi$-pulse drives $n/2$ oscillations at the Rabi frequency between $|0\rangle$ and $|X\rangle$ during the pulse. These oscillations are damped

by the phonon interaction and the final occupancy of the dot is reduced compared to the undamped situation [141].

6.2 Single-pulse experimental results

The aim of this measurement was to demonstrate that an exciton population could be achieved by strongly driving the QD with a positively detuned laser. The single-pulse measurement was carried out by performing a series of measurements where the photocurrent is recorded as the laser power is increased for a given energy. The detuning is then scanned through the single QD transition and the process is repeated, allowing the 2D-plot in fig. 6.4 to be constructed, showing the photocurrent signal as a function of both the laser detuning and pulse area, which are both defined with respect to the C1A QD.

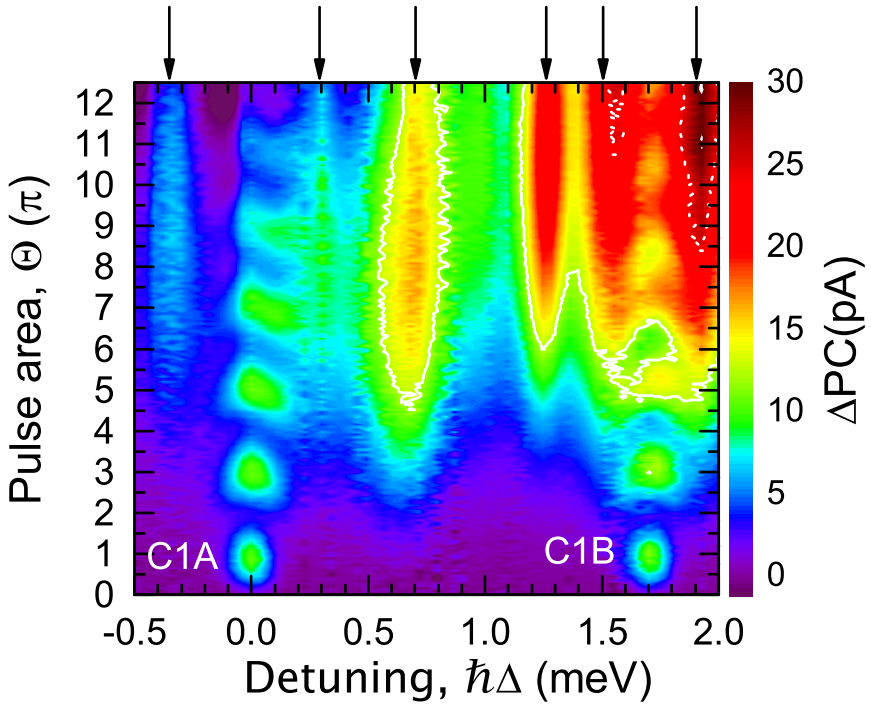

Figure 6.4: Single pulse photocurrent as a function of laser power and detuning. The bias voltage for this measurement was 0.9 V. The solid(dashed) white line represents the maximum photocurrent for a single electron-hole pair (two electron-hole pairs) per pulse. The arrows at the top of the plot indicate less-well coupled QDs than C1A and C1B.

The two QDs C1A and C1B are both observed to undergo several Rabi rotations in the spectral window in fig. 6.4. Both of these QDs are well-coupled to the optical field and high pulse areas (greater than 12π) are achievable for both dots. The solid and dashed white lines respectively indicate the maximum photocurrent for a single electron-hole pair and two electron-hole pairs tunnelling from the dot. In the detuning

range +0.2 meV < Δ < +1.4 meV, the photocurrent signal is composed of the carriers tunnelling from weakly coupled dots (indicated by the arrows) in addition to the off-resonantly generated carriers from C1A. As the pulse area is a function of the square root of the laser power, as in eq. (2.9), the optical power required to reach 12π is a factor of 144 larger than the power needed for a π-pulse. At such high powers, the spectral resolution is limited by weakly coupled dots in the wafer being addressed by the intense pulse at energies in the detuning range where the phonon-assisted population inversion would be expected. Although these QDs are present in the 2D plot, the photocurrent clearly exceeds the threshold for a single electron-hole pair in the region positively detuned from C1A, suggesting that some exciton population is created when the pulse is off-resonant, although this population is difficult to quantify.

6.2.1 Numerical subtraction of weakly coupled dots

In order to compare the single pulse data with the path integral results, the signals originating from weakly coupled QDs were numerically subtracted from the data in the spectral range close to the transition. The dot signals were modelled by extracting a fit to $PC = \sin^2(\Theta')$ at the central energy of each weakly coupled dot. Here the pulse area $\Theta' < \Theta_{\mathrm{C1A}}$. This curve was then convolved with the Gaussian spectral envelope of the laser to give the final two-dimensional feature. Here the damping due to the phonon interaction has been neglected as this is only a small effect for the first rotation. In total, three peaks were identified that were close in energy to the C1A resonance (at $\hbar\Delta$ = -0.34, 0.00 and +0.30 meV). The final result is that the photocurrent originating from C1A can be more clearly resolved for the detuning range of the laser pulsewidth, as shown in fig. 6.5 (a). Here the photocurrent has been normalized so the colorscale gives the exciton population: $C_X = PC/PC(\pi)$, where $PC(\pi)$ is the amplitude of the peak for a π-pulse. The same parameter range for the theoretical data is also shown in fig. 6.5 (b).

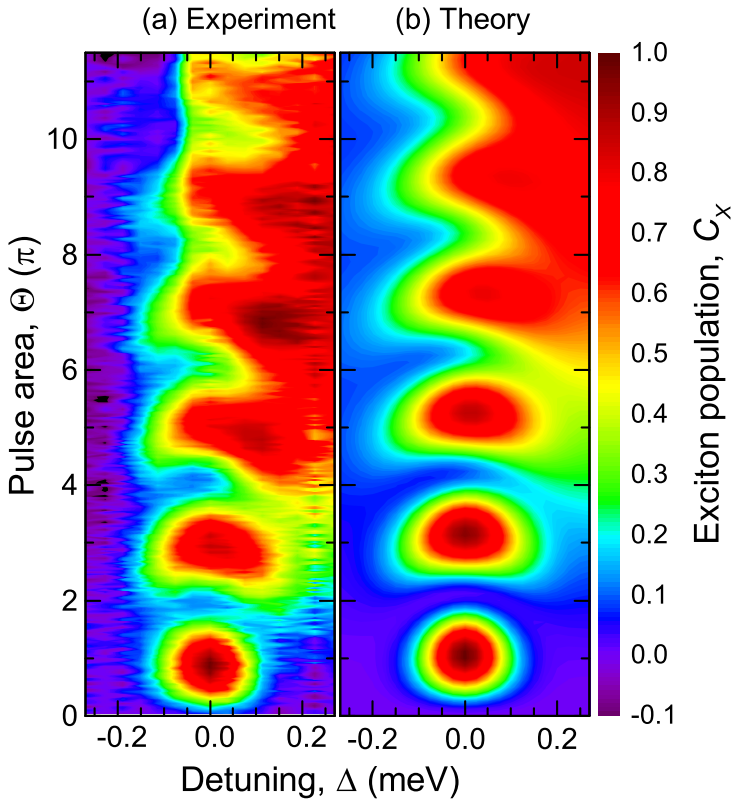

Figure 6.5: (a) close up view of the photocurrent after numerical subtraction of weakly-coupled QD peaks. Spectral region shown is -0.27 < $\hbar\Delta$ < +0.27 meV. (b) Path integral results for the same detuning and pulse area range.

Close-up on laser pulsewidth

On resonance, the rotations in fig. 6.5 (a) for $\Theta > 2\pi$ develop 'wings' and exhibit an arrowhead-like shape, whereas the first rotation replicates the Gaussian laser pulse-shape. The arrowhead has been observed previously, for pulse areas up to 4π [95, 142], and is caused by the increased effective Rabi frequency for the detuned pulse compared with a resonant pulse, leading to a faster rate of dephasing. In addition to the development of wings, the photocurrent for pulse areas greater than 5π blends smoothly into the sideband signal, rather than being isolated peaks. The increased photocurrent is further evidence that the phonon-assisted relaxation process is happening. The theoretical results in fig. 6.5 (b) show fair agreement with the experimental results, although it should be noted that this technique is not 100% reliable due to the errors associated with the numerical subtraction.

6.3 Two-pulse photocurrent spectra

Overview of the pump probe technique

To overcome the spectral resolution of the single-pulse measurement, a second pulse was introduced to probe the exciton population that is created by the off-resonant pump pulse. Since the probe pulse is low-powered, the two-pulse measurement is dot-selective and the resulting signal is dependent only on the population of C1A. Switching to the two pulse set-up reduces the optical power that is available for the pump, as some of the laser has to be channelled into the second pulse shaper. Hence the maximum possible pump pulse area in the two-pulse set up is $8.5 - 9\pi$ (c.f $> 12\pi$ for the single-pulse measurement). In these measurements, the polarization is chosen to be circular so that the selection rules in fig. 2.3 (b) apply. The pump polarization is chosen to be σ^+-polarized, so that the X-state refers to the spin up exciton: $|\Downarrow\uparrow\rangle$. The pump creates a dephased, mixed state exciton population via phonon-assisted relaxation. The probe pulse area is π for all measurements and is chosen to be either co-polarized (X), or cross-polarized ($\bar{X}$), for different experiments. First we examine the spectra for the different probe polarizations, in § 6.3.1 and § 6.3.2, and then move on to evaluating the exciton population that is generated by the pump, in § 6.3.3.

6.3.1 Co-polarized two pulse spectra

The scheme for the co-polarized experiment is shown in fig. 6.6. Here the pump is X-polarized and tuned above the exciton transition. The pump has detuning $\hbar\Delta = +0.832$ meV from the $0-X$ transition. This energy was chosen as it gives the maximum exciton population in the path integral calculations, as shown by the vertical white line in fig. 6.15 (b).

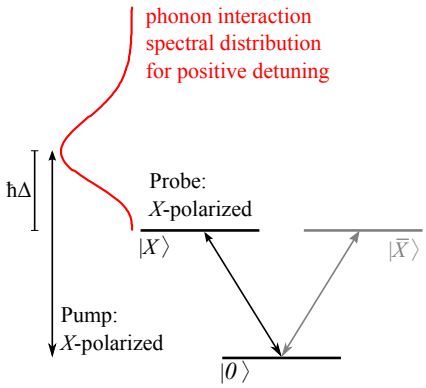

Figure 6.6: Experimental scheme for co-polarized pump and probe. The pump is X-polarized and is tuned to the peak of the exciton-phonon spectral density $J(\omega)$ at positive detuning. The red curve shows an estimation of $J(\omega)$, used for illustrative purpose only. The probe is also X-polarized, addressing the $0 - X$ transition.

To interpret the two-pulse spectra, we consider the action of the π-pulse probe on the two-level system $|0\rangle - |X\rangle$, when the probe is resonant with the transition, as shown in fig. 6.6. The pulse induces a rotation of the state vector through π rads on the Bloch sphere, inverting the z-component of the Bloch vector. The rotation of the state vector results in a change in photocurrent ΔPC_{0-X} that is proportional to the populations after the pump but before the probe: $\Delta PC_{0-X} \propto C_0 - C_X$. In the case where the probe examines an inverted state, $\Delta PC_{0-X} < 0$ and a characteristic gain-like dip is expected in the differential photocurrent spectrum, on resonance with the transition. The experimental results are shown in fig. 6.7 for a range of pump pulse areas, up to 8.46π.

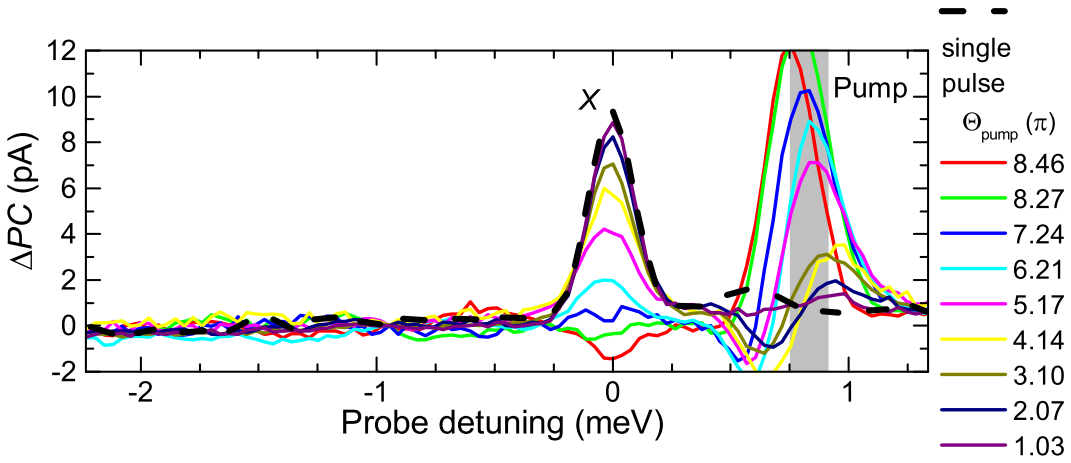

Figure 6.7: Co-polarized two-pulse differential photocurrent spectra for a high-power off-resonant pump. $\tau_{\text{delay}} = 10$ ps and the grey bar is centred on the pump detuning, +0.832 meV. The dashed line is a single-pulse probe-only spectrum and is presented for reference. A background photocurrent has been subtracted from all spectra. Bias = 0.8 V

The amplitude of the $0 - X$ peak in fig. 6.7 is reduced in the presence of the pump pulse, compared to the single-pulse (probe-only) spectrum. For pump pulse areas exceeding 8π, the peak actually turns negative, demonstrating that the system has indeed been inverted by the detuned pump. ΔPC_{0-X} can only be negative when $C_X > C_0$, irrespective of the photocurrent to exciton population calibration and any lifetime effects. It is important to note that the interpulse time delay τ_{delay} was chosen to be 10 ps to maximize the visibility of the dip. At longer time delays, due to the fast electron tunneling time (~ 50 ps at this reverse bias), the exciton population on the dot decays quickly back to a non-inverted state. For time delays shorter than 10 ps (where there is significant overlap in time of the electric field envelopes of the two pulses), the signal develops a dispersive lineshape rather than a single peak. This still has a negative component, which originates from the population inversion, however the single dip is a clearer demonstration. The change in lineshape is attributed to the AC Stark

shift of the $0 - X$ transition by the intense detuned pump laser.

A signal appears in the co-polarized data in fig. 6.7 when the pump and probe overlap spectrally. This is due to interference between the pump and probe electric field amplitudes in time, resulting in a constructive/destructive signal that affects the photocurrent background, which for the strong pump powers here is of the order of a few hundred pA (as can be seen in fig. 4.2 (b)). The signal is observed for different pump detunings, indicating that it does not originate from the occupation of other QDs. Also, if larger time-delay values are used then the interference vanishes.

6.3.2 Cross-polarized two pulse spectra

For cross-polarized (X-pump, $\bar{X}$-probe) a different situation occurs. Here the pump still creates an exciton population, but the probe examines the $0 - \bar{X}$ transition, as shown in fig. 6.8:

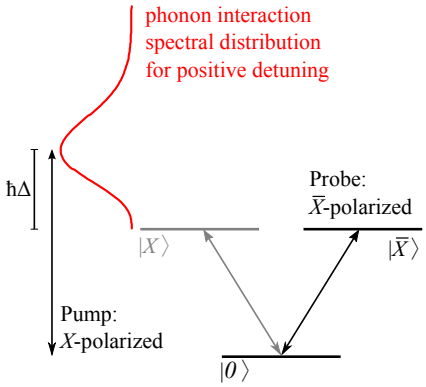

Figure 6.8: Experimental scheme for cross-polarized pump and probe. The pump is X-polarized and is tuned to the peak of the exciton-phonon spectral density $J(\omega)$ at positive detuning. The red curve shows an estimation of $J(\omega)$, used for illustrative purpose only. The probe is, in contrast to the pump, $\bar{X}$-polarized, addressing the $0 - \bar{X}$ transition.

In this case, when the probe is resonant with the exciton transition, it acts to invert the z-component of the orthogonally polarized $0 - \bar{X}$ two-level system, in contrast to the co-polarized probe discussed above. Here, the probe provides a measure of the ground state population C_0. Fig. 6.9 presents the cross-polarized differential spectra for the same pump pulse area range as in fig. 6.7.

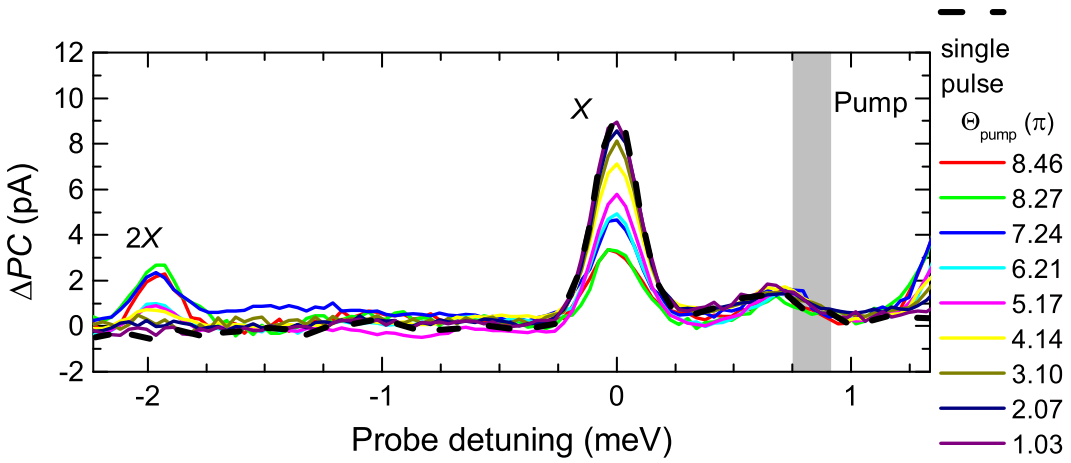

Figure 6.9: Cross-polarized two-pulse differential photocurrent spectra for a high-power off-resonant pump. $\tau_{\text{delay}} = 10$ ps and the grey bar is centred on the pump detuning, +0.832 meV. The dashed line is a single-pulse probe-only spectrum and is presented for reference. A background photocurrent has been subtracted from all spectra. Bias = 0.8 V

The exciton peak at zero detuning falls to below half the amplitude measured in the single-pulse spectrum for high pump pulse areas. This again confirms that the $0 - X$ system has been inverted, since $\Delta PC_{0-\bar{X}} \propto C_0 - C_{\bar{X}}$. A second peak is observed in the cross-polarized spectra, at a detuning of -1.96 meV from the exciton. This peak corresponds to the $X - 2X$ biexciton transition shown in fig. 2.3 (b) and is conditional on the dot being occupied by an X-population, and as in § 6.3.3, provides a third measure of the exciton population.

6.3.3 Evaluation of the exciton population

The amplitudes of the X and $2X$ peaks in the two-pulse spectra provide direct methods of extracting the value of C_X that is initially established by the pump pulse. The exciton lifetime dynamics need to be considered in order to account for the time delay τ_{delay} between the pulses, which means that there is a difference between the population that is created by the pump and the population that is detected by the probe pulse, since electron tunneling occurs on a similar timescale. For this QD, at a reverse bias of 0.8 V (as used experimentally), the exciton fine structure $\hbar\delta$ is 13 μeV, corresponding to a precession time of ~300 ps between the exciton spin states. As τ_{delay} is much less than the precession period, the population transfer into the $\bar{X}$ state is assumed to be negligible. The radiative recombination time for C1A is at least ~400 ps and so is also left out of the analysis here, as only a negligible population can recombine in 10 ps. As discussed in detail in § 5.1, the exciton lifetime is determined by the fast electron tunneling rate and when the exciton decays, it leaves the system shelved in the single hole state.

Here, the probe is weak, so we can exclude phonon-related effects related to the probe. Also, when the probe is resonant with $|0\rangle - |X\rangle$, it is far detuned from any biexciton or positive trion transitions, so we exclude the possibility of populating these states. The effect of the pump pulse is approximated to instantaneously establish an exciton population C_X at time $t = 0$. The probe is also treated as acting instantaneously at time τ_{delay}. At $t = \tau_{\text{delay}}$, the populations of the exciton and hole state are given by:

$$C_X(t) = C_X \times e^{-t/T_1} \tag{6.15a}$$

$$C_{\text{h}}(t) = C_X - C_X(t), \tag{6.15b}$$

and it is only possible for the system to be in the ground state, exciton or single hole state:

$$C_0(t) + C_X(t) + C_{\text{h}}(t) \equiv 1. \tag{6.16}$$

Co-polarized $0 - X$-peak

For co-polarized pulses, the probe inverts the values of C_0 and C_X. Any population that remains in the single-hole state prevents the absorption of the co-polarized pulse and the holes will tunnel from the dot before the next pulse cycle. The photocurrent signal ΔPC_{0-X} is written:

$$\Delta PC_{0-X}/PC(\pi) = C_0(\tau_{\text{delay}}) - C_X(\tau_{\text{delay}}) + C_{\text{h}}(\tau_{\text{delay}}), \tag{6.17}$$

where $PC(\pi)$ is the single π-pulse exciton peak amplitude. Using eqs. (6.15a) and (6.15b), we can extract C_X:

$$C_X = \frac{1}{1 + e^{-\tau_{\text{delay}}/T_1}} \left(1 - \frac{\Delta PC_{0-X}}{\Delta PC(\pi)}\right). \tag{6.18}$$

Here T_1 is the exciton lifetime; $T_1 \approx 1/\Gamma_{\text{e}} = 53$ ps. Eq. (6.18) gives an inversion threshold where $C_X = 0.5$ when $\Delta PC_{0-X} = 0.18\Delta PC(\pi)$.

Cross-polarized $0 - \bar{X}$-peak

When the pump and probe pulses are cross-polarized, the exciton decay does not affect the photocurrent signal. This is because the pulse inverts the $|0\rangle - |\bar{X}\rangle$ transition. $C_{\bar{X}}$ is zero as the pump pulse has no effect on this transition, provided that no spin-flip interactions take place. The time scale for spin-flipping is much longer than the delay values that are used here, as discussed in § 2.6.2 and can therefore be neglected. $\Delta PC_{0-\bar{X}}$ represents the ground state population that is transferred to the $\bar{X}$ state by the probe pulse. Population in both $|X\rangle$ and $|\text{h}\rangle$ reduce the available ground state population. Using eq. (6.16), we can write:

$$C_X = 1 - PC_{0-\bar{X}}/\Delta PC(\pi), \tag{6.19}$$

giving an inversion threshold when $\Delta PC_{0-\bar{X}} = 0.5PC(\pi)$.

Cross-polarized $X - 2X$-peak

The biexciton peak is observed in the cross-polarized spectra only at a detuning of -1.96 meV. In accordance with the selection rules in fig. 2.3 (b), the biexciton is allowed for cross-circularly polarized pulses only and the transition is conditional on the presence of an exciton in the dot. The biexciton lifetime is again limited by the electron tunnelling time. A conditional Rabi-oscillation [71] on the biexciton transition for this QD shows that the dipole moment and therefore pulse area is similar within experimental error to that of the exciton transition. Fig. 6.10 shows two-pulse spectra measured for π-pulse pump, resonant with $|0\rangle - |X\rangle$, with a 10 ps delay time. The amplitude of the biexciton peak $\Delta PC_{X-2X}(\pi)$ is 3.6 pA. A similar consideration of the number of carriers that tunnel when the biexciton is populated gives the third value for C_X in eq. (6.20). The inversion threshold is given when $\Delta PC_{X-2X} = 0.4\Delta PC_{X-2X}(\pi)$.

$$C_X = \frac{\Delta PC_{X-2X}}{\Delta PC_{X-2X}(\pi)} \tag{6.20}$$

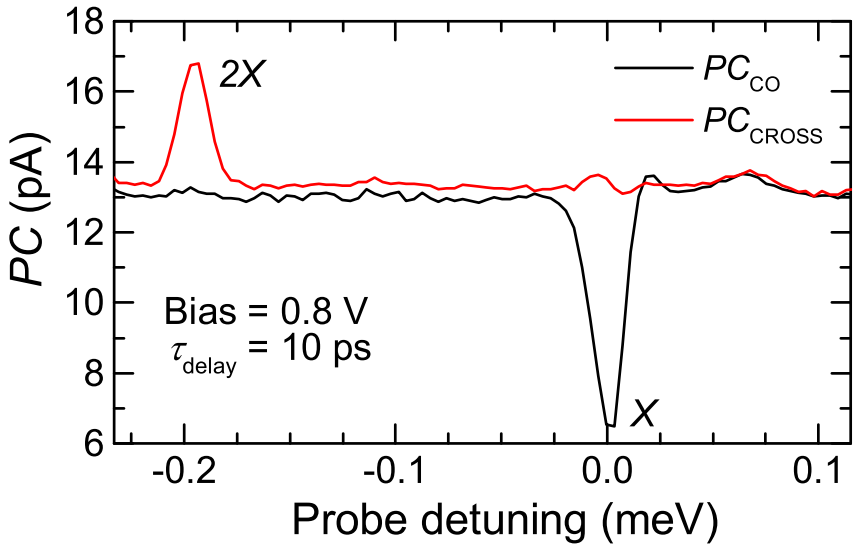

Figure 6.10: Two-pulse spectra with pump pulse area π resonant with $0 - X$ transition.

6.3.4 Effect of pump pulse area on the exciton population

Fig. 6.11 presents the exciton population generated by the pump as a function of the pump pulse area, calculated using the photocurrent signal from all three transitions: PC_{0-X}, $PC_{0-\bar{X}}$ and PC_{X-2X}. The three different measurements all agree well, confirming the accuracy of the values of C_X that are obtained from the data and the assumption that the pump only populates the X-state. The transparency threshold is surpassed for all three datasets when $\Theta_{\text{pump}} > 6.7\pi$. The largest value of Θ_{pump} that

was possible experimentally was 8.46π. Here, the mean value for the exciton population from the three transitions $0 - X$, $0 - \bar{X}$ and $X - 2X$ is $C_X = 0.658 \pm 0.001$. The theoretical curve for the same detuning, corresponding to the vertical line in the path integral calculations in fig. 6.15 (b), is also plotted and agrees excellently with the experimental results. The path integral results also predict that the exciton population could increase further if a higher power could by used for the pump. The theoretical results predict a maximum possible exciton population of ~0.9, for $\Theta = 15\pi$ [132].

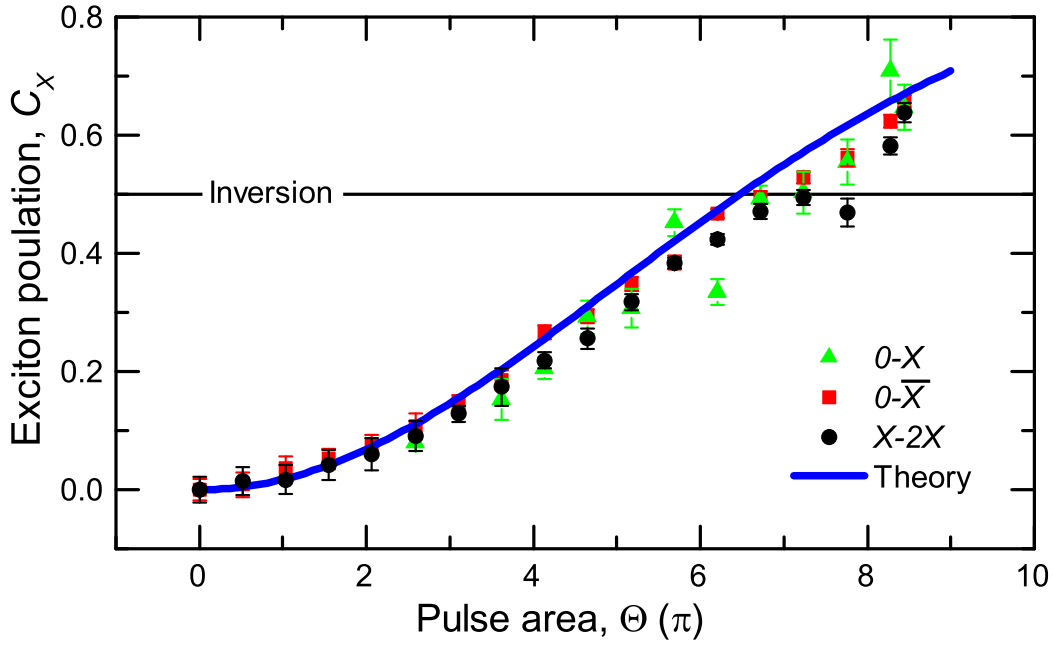

Figure 6.11: The exciton populations C_X, extracted from exciton and biexciton peak amplitudes in figs. 6.7 and 6.9, using eqs. (6.18, 6.19 and 6.20), and are plotted as a function of pump pulse area. The pump detuning $\hbar\Delta$ is +0.832 meV for all measurements and τ_{delay} is 10 ps. The path integral results are also shown for a pulse with the same detuning as the pump.

6.3.5 Effect of pump detuning on the exciton population

In order to investigate the spectral behaviour of the phonon-assisted exciton preparation scheme, the pump detuning $\hbar\Delta$ is scanned for a fixed value of $\Theta = 7.24\pi$, corresponding to the horizontal line in fig. 6.15 (b). C_X is measured for each individual detuning step by probing the exciton energy, and the resulting exciton population is shown in fig. 6.12. Only the values from $PC_{0-\bar{X}}$ are presented as the co-polarized two-pulse spectra exhibit interference when the pump detuning is less than 0.25 meV from the exciton transition.

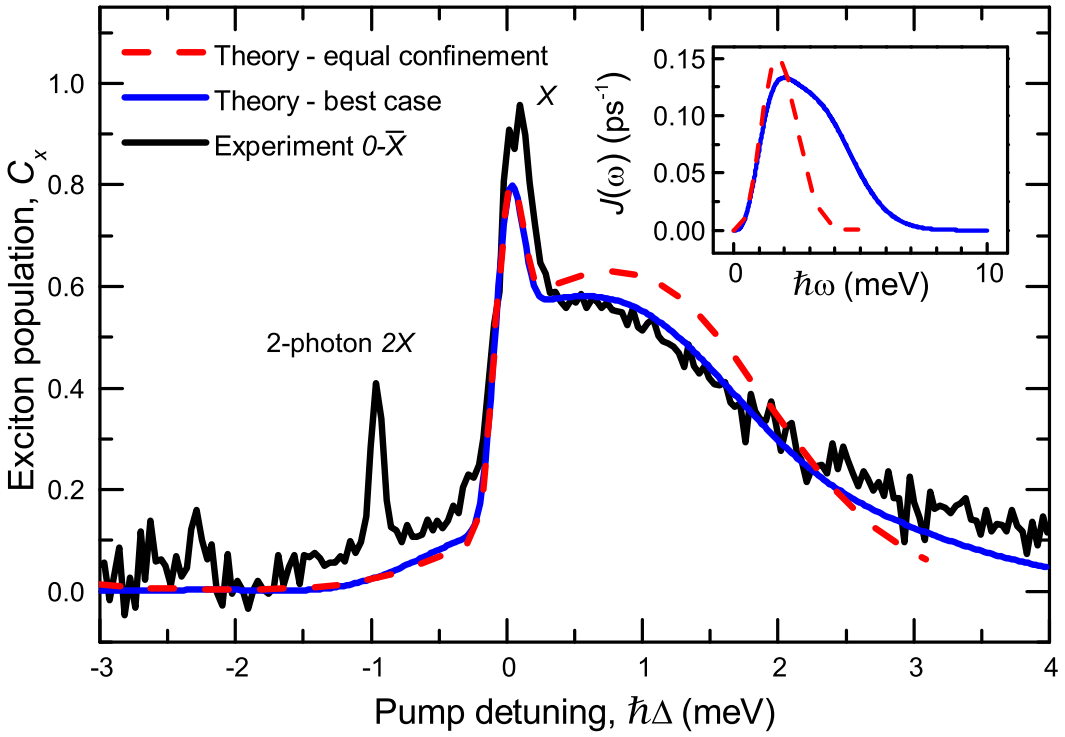

Figure 6.12: Exciton population created by a 7.24π pump as a function of the pump detuning Δ. The probe pulse area is π and $\tau_{\text{delay}} = 15$ ps (blue) Path integral results for a single 7.24π-pulse. The additional peak at Δ = -0.98 meV is attributed to the two-photon $2X$ resonance. The inset shows the spectral density of the exciton-phonon interaction $J(\omega)$ as used in the path integral calculations. The red dashed curves in the main plot and inset are the calculated values for equal electron and hole confinement energies (see § 6.4.2)

.

Three important features are shown in the experimental data in fig. 6.12. Firstly, there is a pulse-width limited peak for zero detuning, corresponding to resonant excitation of the exciton. Secondly, a broad sideband is observed at positive detuning, which is due to phonon-assisted relaxation into the exciton state. Thirdly, there is an additional peak, detuned by -0.98 meV from the neutral exciton transition, this is attributed to the two-photon $0 - 2X$ transition and is discussed later, in §. 6.3.5.

The spectral dependence provides further evidence that the exciton population is established by thermal relaxation as the exciton preparation exhibits a roll-off with increasing $\hbar\Delta$. The spectral roll-off is characteristic of the spectral dependence of the exciton-phonon interaction: $J(\omega)$. The calculated values for $J(\omega)$ as used in the path integral calculations are presented in the inset to fig. 6.4. At large effective Rabi frequencies, the phonon bath can no longer respond to the optical driving field and the thermal relaxation rate is reduced, preventing the population inversion. Fig. 6.12 also confirms that the exciton state is predominantly populated only for a positively detuned laser, in agreement with the admixture of the quantized basis states that defines the

lower energy state $|\beta\rangle$. At negative detuning, there is a slightly higher value of C_X than expected, this is attributed to sample heating by the high-powered pump (estimated sample temperature is 6-7 K).

A very good level of agreement is obtained between the experimental data shown in fig. 6.12 and the path integral prediction, which is shown by the blue curve. The anisotropy with respect to the sign of the detuning and shape of the roll-off with increasing Δ are both excellently replicated.

Two-photon $2X$-transition

The two-photon $0-2X$ transition is also visible in fig. 6.12, at a detuning $\Delta = -0.96$meV (half the biexciton binding energy). The selection rules for the two-photon resonance are linearly polarized [72], as discussed in § 2.3.2. The presence of the two-photon transition in the spectrum indicates that the experimental circular polarization is actually slightly elliptically polarized. The high intensity of the pump means that a large enough linear component is able to address the transition, creating a biexciton population of 0.315. The two-photon Rabi rotation of the $|0\rangle - |2X\rangle$ transition is shown alongside the standard $0-X$ Rabi rotation in fig. 6.13. Linear polarization is used for the $0-2X$ rotation, and circular polarization for $0-X$. The additional attenuation of the laser power by the quarter-wave plate when circular polarization is used has been compensated for in the x-axis scale. To achieve $C_{2X} = 0.315$, the equivalent pulse area required for the $0-X$ rotation is $\sim 3.75\pi$. This is a non-trivial amount of power (14 times the π-pulse power of the probe). It is likely that the linear component of the pump pulse only becomes significant in the high pulse area regime and the effect is exacerbated by the large optical powers that are used. This is why the $X-2X$ transition is observed with a high degree of circular polarization in fig. 6.10; in the low power regime, the linear component of the power is small and does not influence the selection rules for the transition.

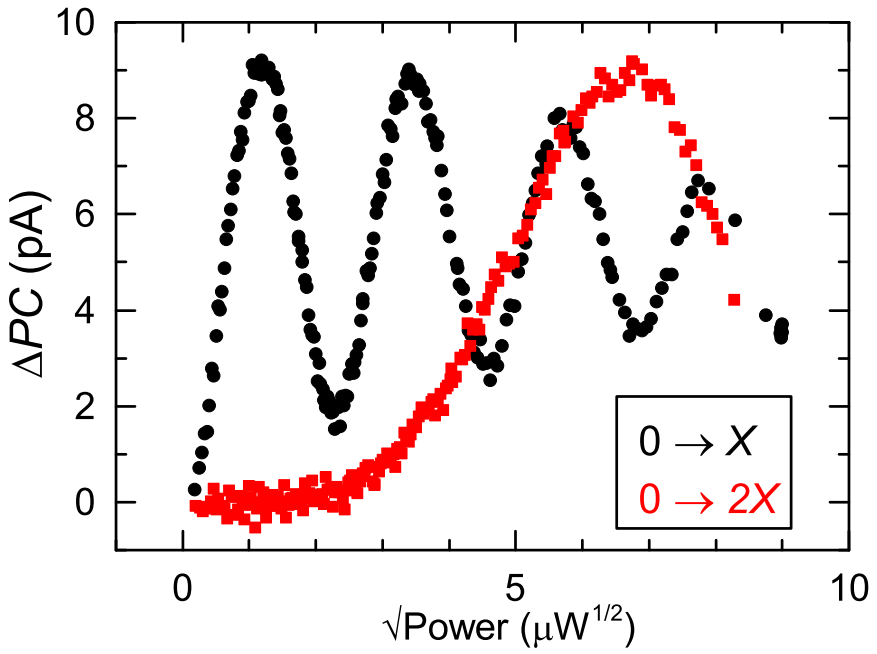

Figure 6.13: Circularly polarized Rabi rotation measurement for the $0-X$ transition and the linearly-polarized $0-2X$ two-photon transition.

6.4 Comparison with path integral results

In this section, we compare the experimentally obtained values of the exciton population with the values that are predicted by the path integral calculations. The parameters used in the calculations are discussed

6.4.1 Accuracy of coupling strength for the calculations

In order to ensure that the values used in the path integral results closely resembled the experimental results, the path integral calculations were repeated for different exciton-phonon coupling strengths. The values that were investigated started with the standard literature value of the coupling strength used theoretically for GaAs [134]. This was then increased by different factors in the calculations. The best data with which to compare the theory results is the standard Rabi rotation for zero detuning, as shown for C1A in fig. 6.14, a range of coupling strengths up to 1.3 times the GaAs standard, given by the spectral density $J(\omega)$ of the interaction, are used in the calculations.

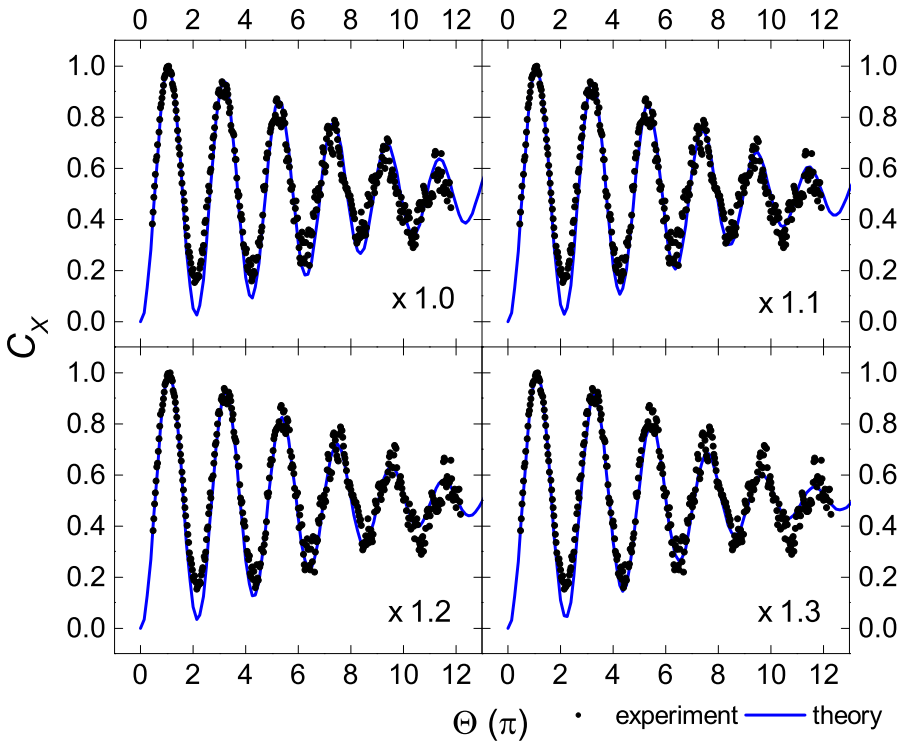

Figure 6.14: Comparison between the experimentally observed zero-detuning Rabi rotation for C1A and theoretical values when the exciton-phonon coupling strength is multiplied by the factors shown in the plots. In each case the pulse area scale for the experimental results has been adjusted manually to match the Rabi frequency re-normalization associated with each coupling strength.

The theoretical results in fig. 6.14 agree well with the experimental results, particularly when the coupling strength factor is 1.0 and 1.1. These plots confirm that the standard coupling strength for GaAs is suitable for making an accurate comparison with the experimental results in this chapter.

6.4.2 Theory model details

In order to obtain the level of agreement with the experimental results shown in figs. 6.11 and 6.12, the exciton-phonon interaction spectral density $J(\omega)$ was adjusted by hand and fitted to the experimental data in fig. 6.12. The theory treats the QD as a spherical shape with radial height 3.5 nm and the calculations consider the laser pulse FWHM to be 16.8 ps, as in the experimental case. The QD is modelled as having spherically symmetric parabolic confinement potentials for the electron and hole. The electron (hole) wavefunction $\psi_{\mathrm{e(h)}}$ is considered to have the form:

$$\psi_{\mathrm{e(h)}}(\mathbf{r}) = \frac{1}{\pi^{3/4} a_{\mathrm{e(h)}}^{3/2}} \exp\left(\frac{-\mathbf{r}^2}{2a_{\mathrm{e(h)}}^{3/2}}\right), \tag{6.21}$$

where $a_{e(h)}$ is the electron (hole) confinement length.

In reality, the QD is likely to have a truncated pyramid shape, as in fig. 2.1, with more exotic confinement potentials than eq. (6.21). However, the spherical approximation is usually considered valid, as the height of the QD is much shorter than the base length, providing the strongest carrier confinement in the growth direction. In the theory, the phonon influence on the dot dynamics is mediated mainly by the spectral density of the interaction: $J(\omega) = \sum_{\mathbf{k}} |g_{\mathbf{k}}|^2 \delta(\omega - \omega_{\mathbf{k}})$, where $g_{\mathbf{k}}$ is the coupling strength for a phonon with wavevector $\mathbf{k}$, as in eq. (6.12). The dispersion relation is assumed to be linear: $\omega_{\mathbf{k}} = v_c|\mathbf{k}|$, where v_c is the sound velocity. For bulk LA phonons coupled via the deformation potential, the spectral density is written [140]:

$$J(\omega) = \frac{\omega^3}{4\pi^2 \rho \hbar v_c^5} \left[D_{\mathrm{e}} \exp\left(\frac{-\omega^2 a_{\mathrm{e}}^2}{4v_c^2}\right) - D_{\mathrm{h}} \exp\left(\frac{-\omega^2 a_{\mathrm{h}}^2}{4v_c^2}\right) \right]^2, \tag{6.22}$$

where ρ is the mass density and $D_{e(h)}$ is the electron (hole) deformation potential constant. The values used in the model were taken from ref [134]: $\rho = 5370\ \mathrm{kg\,m^{-3}}$, $v_c = 5110\ \mathrm{m\,s^{-1}}$, $D_{\mathrm{e}} = 7.0$ eV and $D_{\mathrm{h}} = -3.5$ eV. The super-Ohmic $\sim \omega^3$ dependence at low frequency is characteristic bulk acoustic phonons and is independent of the QD material or shape.

The confinement lengths $a_{e(h)}$ were altered systematically until the the best agreement with the experimental results was obtained; for $a_{\mathrm{e}} = 4.5$ nm and $a_{\mathrm{h}} = 1.8$ nm, resulting in the spectral density given by the blue curve in the inset to fig. 6.12. Unless otherwise stated, these values were used for the calculations. The uncertainty in a_{e} and a_{h} is estimated from the step size used to be $\sim \pm 0.2$ nm. $J(\omega)$ exhibits a double-Gaussian shape, highlighting the difference in the electron and hole confinement potentials. The Gaussians in eq. (6.22) are the result of Fourier transforming the electron and hole probability densities. The spectral dependence of the phonon-assisted exciton population is plotted as the dashed red curve in fig. 6.12, for the simplified case where $a_{\mathrm{e}} = 3.5$ nm and $a_{\mathrm{h}} = 3.0$ nm, as used previously [132]. These values equate to equal electron and hole confinement potentials once the difference in effective mass is taken into account. The dashed red curve overestimates the exciton population for $0 < \hbar\Delta < 2$ meV and underestimates if the detuning is larger than 2 meV. The corresponding $J(\omega)$ has a single Gaussian peak, in contrast to the double-peak when individual confinement potentials are taken into account. For comparison, values for the confinement lengths from the literature are $a_{\mathrm{e}} = 7.6$ or 5.2 nm and $a_{\mathrm{h}} = 1.8$ nm [143, 144]. The shorter confinement lengths that give the best agreement with our experimental data suggest that the carriers are more strongly confined in our experimental QD than in the QDs examined in refs. [143] and [144]. a_{h} is consistently less than a_{e} for all the values discussed here.

6.4.3 Mapping the phonon sideband signal

Fig. 6.15 (a) shows the exciton population that is measured experimentally as a function of both pump laser pulse area and detuning. Here, the interpulse delay time is increased to 33.6 ps to eliminate any possible pulse overlap effects. The same measurements as in fig. 6.12 were performed, and C_X was extracted from $\Delta PC_{0-\bar{X}}$ only. The corresponding path integral results are presented in fig. 6.15 (b).

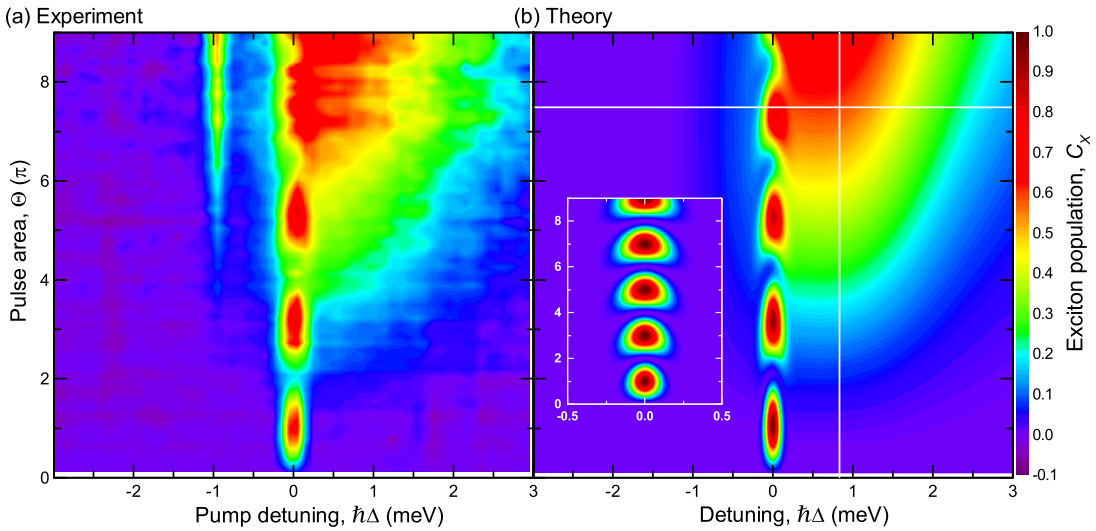

Figure 6.15: (a) Experimentally obtained C_X vs Θ and $\hbar\Delta$. (b) Path integral results for the same pulse area and detuning range as in (a). The white lines are the constant detuning of +0.834 meV (vertical) and pulse area of 7.24π (horizontal) as used respectively in figs. 6.11 and 6.12. The inset shows the calculated values with no interaction with the phonon bath.

Fig. 6.15 (a) shows that there is a large, stable region on the 2D plot where the population can be inverted through the off-resonant process. In contrast to the on-resonance Rabi rotation, the phonon-assisted pumping is highly resilient to fluctuations in either the pulse area or the laser energy. The shape of the near-resonance regime (within the laser linewidth of the transition) demonstrates that for $\Theta > 2\pi$, the rotations develop an 'arrowhead' shape, in agreement with the data in fig. 6.5 (a). This is attributed to the increased effective Rabi frequency and is not a phonon-related effect. However, the asymmetry of the rotations is due to phonon-assisted preparation. The rotations for $\Theta > 6\pi$ show a smooth transition into the phonon sideband signal, rather than being exhibited as isolated peaks.

The expected roll-off due to the spectral density is shown in the colourplot, as in fig. 6.12, for all pulse areas. The increase in exciton population with pulse area within the experimental range is also evident, with no inversion being possible below 6π. It is important to note that similar results are presented in ref. [95], although these earlier results were taken with a less-stable experimental setup and a pulse area of only 4π

was available, meaning the measurement was restricted to the regime where inversion is impossible. Due to a sample temperature of 15 K, a more symmetric phonon-sideband was observed in [95] with respect to the detuning sign. The arrowhead shape of the second rotation was reported in this work, and also in ref. [142].

The path integral results in fig. 6.15 (b) show an excellent level of agreement with the experimental results and the overall shape of the phonon-assisted preparation is replicated extremely well. The inset to fig. 6.15 (b) shows the calculated values when the phonon coupling strength is set to zero. Here, the arrowhead shape of the high pulse area rotations is observed, but the off-resonant signal disappears, as does the damping of the rotations on resonance. Without the phonons, there is no state transfer from $|\alpha\rangle \rightarrow |\beta\rangle$ and the exciton state cannot be occupied via off-resonant driving.

6.5 Conclusions

The results presented in this chapter are the first demonstration that the two-level system consisting of the bare QD states can be inverted through off-resonantly optically driving the phonon bath. Fast relaxation into the lower energy dressed state provides a method where the interaction with phonons actually populates the dot. Also, by fitting the interaction spectral density to the experimental data, it is possible to reveal more information about the electron and hole confinement energies than simply studying resonant Rabi rotations. This scheme has the advantage over rapid adiabatic passage experiments such as those presented in refs. [111, 145] that the relaxation rates for high pulse areas can be fast compared with the laser pulse duration, meaning that the population inversion is established almost instantly on-demand, rather than the several hundred picoseconds that are required for the purely adiabatic process.

Phonon-assisted exciton preparation could potentially be useful for enabling coherent control experiments in materials such as GaN, which has a phonon coupling strength three times greater than GaAs. The increased phonon coupling strengths in such materials would be large enough to make resonantly driving the inversion difficult. In this case faster exciton preparation via the phonon-assisted process would be possible, as would a wider spectral region where the inversion is established [132]. It is also possible that off-resonant driving may provide a method for increasing the scalability of integrated quantum optical circuits, as it potentially removes the strict requirement for individual nodes to emit at exactly the same energy. Recent work by Madsen *et al* [138] suggests that phonon assisted inversion could be a robust, non-resonant deterministic pumping scheme for polarized single photon sources.

Finally it is important to note that upon completion of the work in this thesis, similar experiments were reported by Ardelt *et al* [146] and Bounouar *et al* [147]. The work in these two papers agrees well with the findings presented here, strengthening the case for phonon-assisted exciton and biexciton generation.

Chapter 7

Conclusions and future work

7.1 Conclusion

This thesis has presented the results of my experimental investigations of the coherent exciton system of single quantum dots, using ultrafast optical excitation combined with photocurrent detection. In particular, there are two principal conclusions that can be made from this work:

1. By applying a time-varying voltage signal to a QD-Schottky diode device, it is possible to enhance the detection efficiency by modifying the voltage-dependent carrier tunneling rates on the timescale of the laser pulse sequence. This overcomes the compromise when using photocurrent detection for coherent control experiments that arises due to the inverse relationship between the exciton lifetime and fast carrier tunneling rates, which are necessary for a high detection efficiency. Exciton Rabi rotations are shown to be robust against the use of the bias modulation scheme, allowing the detection efficiency to be enhanced by up to 250% without any additional exciton dephasing.

2. By strongly driving the phonon-sideband to positive detuning of the exciton transition, a population inversion in the excitonic basis can occur. The inversion is a result of phonon-assisted relaxation of the optically dressed states of the two-level system and occurs in the timescale of the laser pulse. The inversion is characterized in terms of both pulse area and detuning of the driving laser, and a stable region is observed up to a detuning of $\sim$1.5 meV above the transition energy. Combining these results with theoretical data from path integral calculations allows the values of the carrier confinement lengths for the QD: 4.5 nm for the electron and 1.8 nm for the hole. Obtaining these values allows more information to be known about the form factor of the exciton-phonon interaction than previous studies, which have focussed on resonant Rabi rotations.

In Summary, these experiments give further insights into the coherent manipulation of single QD states. The results presented in Chapter 5 provide an improvement to the existing photocurrent technique for reading out the state of a QD qubit and the results in Chapter 6 demonstrate experimentally for the first time that phonon-assisted relaxation of an optically driven QD can result in a population inversion. The interactions with phonons that are traditionally seen as a detrimental effect for the semiconductor qubit systems can actually be useful, and potentially could provide a path to new experimental schemes.

7.2 Future work

Enhanced readout for the hole-trion transition

A variation of the bias modulation technique used in Chapter 5 could be employed for interesting future experiments, particularly experiments with more complex voltage waveforms, such as a scheme designed to maximize the readout efficiency for a single hole spin, instead of the QD exciton. This proposal would make use of the ability to electrically switch the tunneling rates between high and low values for three purposes. Firstly, the exciton would be generated with the bias at a high value, V_{high}, ensuring that it is quickly ionized via electron tunneling, preventing radiative recombination. Secondly, the bias would be reduced to a low value, V_{low} so that the hole would remain in the dot during the spin control process. Thirdly, the bias would again be switched to V_{high}, clearing the hole from the dot before the arrival of the next pulse. For these experiments, a sample with a large hole tunneling potential barrier would be beneficial as then the hole would remain in the dot despite the large applied field at the beginning of the modulation cycle. A schematic showing the voltage modulation scheme for single hole spin control is shown in fig. 7.1.

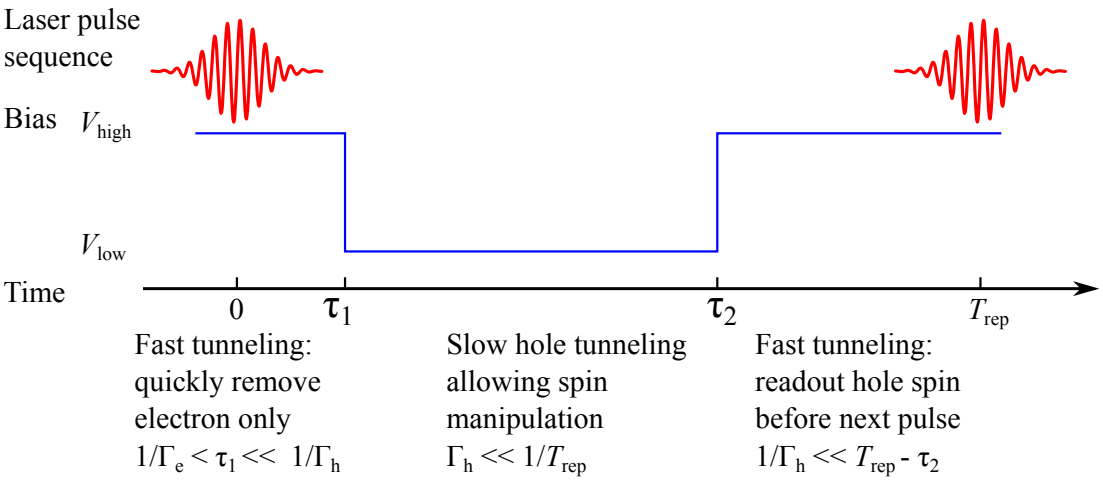

Figure 7.1: Proposed Voltage modulation scheme for hole spin initialization, control and readout. Not to scale. Here the voltage is switched between V_{low} and V_{high} several times during the cycle in order to maximize the readout efficiency of a single hole spin.

Optical rotation of a hole spin about an arbitrary axis

So far, for single-spin experiments, coherent control experiments have involved an optically induced rotation of the state vector about a single axis. The applied magnetic field provides the orthogonal rotation axis necessary for complete Bloch sphere control. Due to the small hole Zeeman energy, it is possible to realize an isolated Λ-transition in the hole-trion system shown in fig. 2.6 (b). The polarization of a control laser pulse determines the rotation axis. At a B-field of 4.7 T, the in-plane hole and electron Zeeman energies are approximately 20μeV and 125μeV, respectively. The pulse width ΔE of the control pulse needs to satisfy 20μeV$\ll \Delta E \ll$125μeV. If this condition is met then the control will address both the $\mathrm{h}_x - X_x^+$ and $\mathrm{h}_{\bar{x}} - X_x^+$ transitions, without addressing the $X_{\bar{x}}^+$-state. Here the major experimental obstacle to consider is the pulsewidth of the control pulse. Spectrally wider pulses would address the opposite polarization to the control pulse at the same time, leading to a geometric phase being acquired in the both directions, which would cancel out. Currently, the Fourier transform limit of the pulse-shapers is $\sim$150 μeV. To reduce ΔE further than this would require an improvement in the spectral resolution that is possible. This could be achieved by increasing the length of the pulse-shapers (if physical space permits), increasing the number of lines per mm on the diffraction gratings, or by redesigning the pulse shaper so that a reflected configuration is used.

Observation of reappearance of Rabi rotations

This experiment would involve driving on resonance Rabi rotations to a very high pulse area regime ($20\pi < \Theta < 30\pi$). Here, the Rabi energy exceeds the maximum in the spectral density of the exciton-phonon interaction $J(\omega)$, as shown in the inset to fig. 6.15 (a). Here, the phonon-assisted relaxation rate actually decreases when further increasing Θ, in effect decreasing the excitation induced dephasing that leads to the damping of the resonant rotations. The amplitude of the rotations is predicted to return to the pre-damped levels [148]. The pulse area where the 'revival' is predicted to occur is dependent on the pulsewidth of the laser, and the revival should be seen at smaller pulse areas for faster pulses [149]. A side-effect of this measurement would be to repeat the measurements in fig. 6.15 (a) for higher pump pulse areas so that the opposite edge of the inversion plateaux can be seen, as the off resonant exciton population will also be less efficient as the peak of $J(\omega)$ is surpassed by the effective Rabi frequency.

Appendix A

Derivation of rate equation model used in Chapter 5

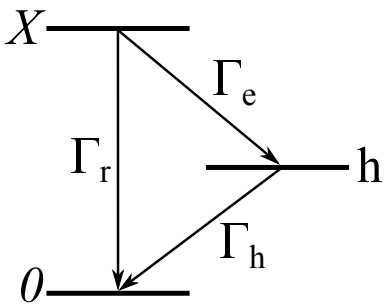

Figure A.1: QD as three-level system.

The QD is modelled as a three-level system, as in fig. A.1, where the population can be in either the neutral exciton X, single-hole h or crystal ground state, 0. The exciton decays either by radiative recombination with rate Γ_r, or by electron tunneling with rate Γ_e. Any population shelved in the single-hole state can then tunnel out of the dot at a rate Γ_h, retuning the system to 0. The tunneling rates are dependent on voltage, which with an AC bias is a function of time. Γ_r is taken to be bias-independent in the voltage range used in experiments. We can write the following rate equations to describe the populations of the three different states:

$$\dot{X} = -\left(\Gamma_\mathrm{r} + \Gamma_\mathrm{e}\right) X \tag{A.1}$$

$$\dot{\mathrm{h}} = \Gamma_\mathrm{e} X - \Gamma_\mathrm{h} \mathrm{h} \tag{A.2}$$

$$\dot{0} = \Gamma_\mathrm{r} X + \Gamma_\mathrm{h} \mathrm{h} \tag{A.3}$$

From eq. (A.1), we can write:

$$\frac{\mathrm{d}}{\mathrm{d}t} X \exp\left(-\int_0^t \left(\Gamma_\mathrm{e}(t') + \Gamma_\mathrm{r}\right)\, \mathrm{d}t'\right) = 0, \tag{A.4}$$

giving:

$$X(t) = X(0)\exp\left(-\int_0^t \left(\Gamma_\mathrm{e}(t') + \Gamma_\mathrm{r}\right)\,\mathrm{d}t'\right). \tag{A.5}$$

First we examine the case where $T_\mathrm{rep} \to \infty$ and all of the hole population is allowed to tunnel from the QD. In this case the photocurrent $PC_\text{no hole limit}$ is given by:

$$PC_\text{no hole limit} = \int_0^t \Gamma_\mathrm{e}(t')X(t')\,\mathrm{d}t', \tag{A.6}$$

substituting eq. (A.5) into eq. (A.6), we obtain:

$$PC_\text{no hole limit} = X(0)\int_0^{T_\mathrm{rep}} \exp\left(-\int_0^t \left(\Gamma_\mathrm{e}(t') + \Gamma_\mathrm{r}\right)\,\mathrm{d}t'\right)\Gamma_\mathrm{e}(t)\,\mathrm{d}t. \tag{A.7}$$

To check that this is correct, we replace $\Gamma_\mathrm{e}(t)$ with Γ_e, and eq. (A.7) reduces to

$$PC_\text{no hole limit} = X(0)\frac{\Gamma_\mathrm{e}}{\Gamma_\mathrm{e}+\Gamma_\mathrm{r}}, \tag{A.8}$$

which gives the same result as in ref. [64], where the model considers a DC bias only. Now, we consider the case where T_rep is finite, and similar in magnitude to $1/\Gamma_\mathrm{h}$. Here there is a nonzero probability that the hole will remain in the dot when the next pulse arrives, preventing absorption. From eq. (A.2), we can write:

$$\left(\dot{\mathrm{h}} + \Gamma_\mathrm{h}\mathrm{h}\right) = \Gamma_\mathrm{e}X, \tag{A.9}$$

leading to

$$\frac{\mathrm{d}}{\mathrm{d}t}\left(\mathrm{h}\exp\left(\int_0^t \Gamma_\mathrm{h}(t')\,\mathrm{d}t'\right)\right) = \Gamma_\mathrm{e}(t')\exp\left(\int_0^t \Gamma_\mathrm{h}(t')\,\mathrm{d}t'\right)\exp\left(-\int_0^t \left(\Gamma_\mathrm{r}+\Gamma_\mathrm{e}(t'')\right)\,\mathrm{d}t''\right), \tag{A.10}$$

which has the solution:

$$\mathrm{h}(t) - \mathrm{h}(0) = \exp\left(-\int_0^t \Gamma_\mathrm{h}(t')\,\mathrm{d}t'\right)\int_0^t \Gamma_\mathrm{e}(\tau)\exp\left(\int_0^t \Gamma_\mathrm{h}(t')\,\mathrm{d}t'\right) \exp\left(-\left(\int_0^\tau \left(\Gamma_\mathrm{r}+\Gamma_\mathrm{e}(t')\right)\,\mathrm{d}t'\right)\right)\mathrm{d}\tau. \tag{A.11}$$

Making the assumption $\Gamma_\mathrm{h} \ll \Gamma_\mathrm{e}$, then:

$$\exp\left(\int_0^t \Gamma_\mathrm{h}(t')\,\mathrm{d}t'\right) \approx 1,$$

we also assume that $\mathrm{h}(0) = 0$, to give:

$$\mathrm{h}(t) = g(\Gamma_\mathrm{e}) \times \exp\left(-\int_0^t \Gamma_\mathrm{h}(t')\,\mathrm{d}t'\right), \tag{A.12}$$

where:

$$g(\Gamma_\mathrm{e}) = \int_0^{T_\mathrm{rep}} \Gamma_\mathrm{e}(t)\exp\left(-\int_0^t (\Gamma_\mathrm{r}+\Gamma_\mathrm{e}(\tau))\,\mathrm{d}\tau\right)\,\mathrm{d}t, \tag{A.13}$$

as given in eq. (5.6). In the long-time limit ($T \gg T_X^1$), the photocurrent is given by $PC = 1 - \mathrm{h}(T) - X(T)$ and, since $X(T) \approx 0$, we can write:

$$PC = 1 - h(T) \tag{A.14}$$

or, equivalently:

$$PC = 1 - g(\Gamma_\mathrm{e}) \exp\left(-\int_0^T \Gamma_\mathrm{h}(t')\,\mathrm{d}t'\right). \tag{A.15}$$

The detection efficiency is defined as $\eta = PC/PC_\mathrm{ideal}$, and as $PC_\mathrm{ideal} \equiv 1$, eq. (A.15) can be written:

$$\eta = g(\Gamma_\mathrm{e})\left(\frac{1}{g(\Gamma_\mathrm{e})} - \exp\left(-\int_0^t \Gamma_\mathrm{h}(t')\,\mathrm{d}t'\right)\right). \tag{A.16}$$

The following approximation is made:

$$\frac{1}{g(\Gamma_\mathrm{e})} \approx 1,$$

so that eq. (A.16) can be written:

$$\eta = f\left(\Gamma_\mathrm{h}\right) \times g\left(\Gamma_\mathrm{e}\right) \tag{A.17}$$

and

$$f(\Gamma_\mathrm{h}) \approx 1 - \exp\left(-\int_0^{T_\mathrm{rep}} \Gamma_\mathrm{h}(t)\,\mathrm{d}t\right), \tag{A.18}$$

as given in eq. (5.6).

Appendix B

Laser photodiode amplification and spectral filter

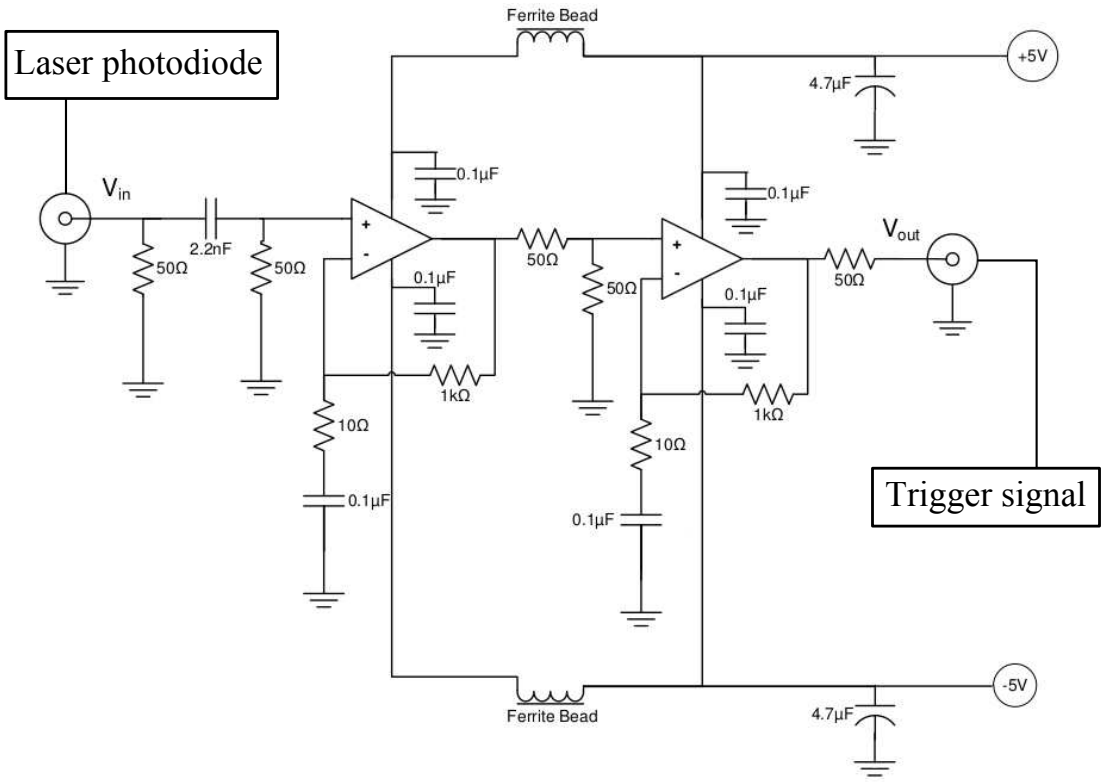

Figure B.1: Circuit for amplifying the laser photodiode to a suitable level for the function generator trigger signal. Higher laser harmonics are also filtered out through the use of capacitors and narrow-band operational amplifiers. This circuit was designed by R Coles as part of his MSc project [150].

Appendix C

Hole spin preparation for a near-zero exciton fine structure splitting

C.1 Introduction

One of the DiVincenzo criteria for a proposed qubit is the ability to initialize the qubit into a well-known state. As described in § 2.5, the spin of single holes has been used as a qubit in several experimental schemes [32,90,108]. Works by Godden *et al* demonstrate that for a QD with a non-zero fine structure, the hole spin preparation fidelity is reduced [82,83]. In the PC detection regime, hole initialization is achieved via ionization of the neutral exciton. In Godden's experiments, a QD with typical intermediate fine structure splitting of ∼18 μeV is used. Here, two dots are investigated: C2A, which has a relatively large fine structure splitting ($\hbar\delta \sim 30$ μeV) and C1B, which has a small fine structure splitting, which is below the resolution limit of the measurement technique (see fig. 4.7). The spin preparation fidelity is shown to be greatly improved in the case of near-zero fine structure. Although these results are only preliminary, they should provide a basis for more in-depth experiments in the future. The QD with the near-zero fine structure splitting is found to have the highest fidelity hole spin preparation for a single QD as reported at the time of writing.

C.2 Single hole spin preparation

To measure the hole spin preparation fidelity, a set of two-pulse measurements were performed. The two pulses were separated by a time delay τ_{delay} and are either co, or cross-circularly polarized. The first pulse is resonant with $0 - X$, has pulse area π and is σ^+-polarized, exciting the $|\Uparrow\downarrow\rangle$ neutral exciton, which decays via electron tunneling to the hole state $|\Uparrow\rangle$, if the spin preparation is ideal. The second pulse is

scanned through the single hole to positive trion transition, and has pulse area equal to π for the $\mathrm{h}-X^+$ transition. The co-polarized σ^+-probe addresses the $|\Downarrow\rangle - |\Downarrow\Uparrow\downarrow\rangle$ hole-trion transition and the cross-polarized σ^--probe addresses $|\Uparrow\rangle - |\Uparrow\Downarrow\uparrow\rangle$. In order to completely isolate the trion signal from weakly coupled dot peaks, a single-pulse spectrum measured with the second pulse only is subtracted form the two-pulse spectrum, these differential photocurrent spectra are presented in figs. C.1 (a) and (b), for C1B and C2A, respectively.

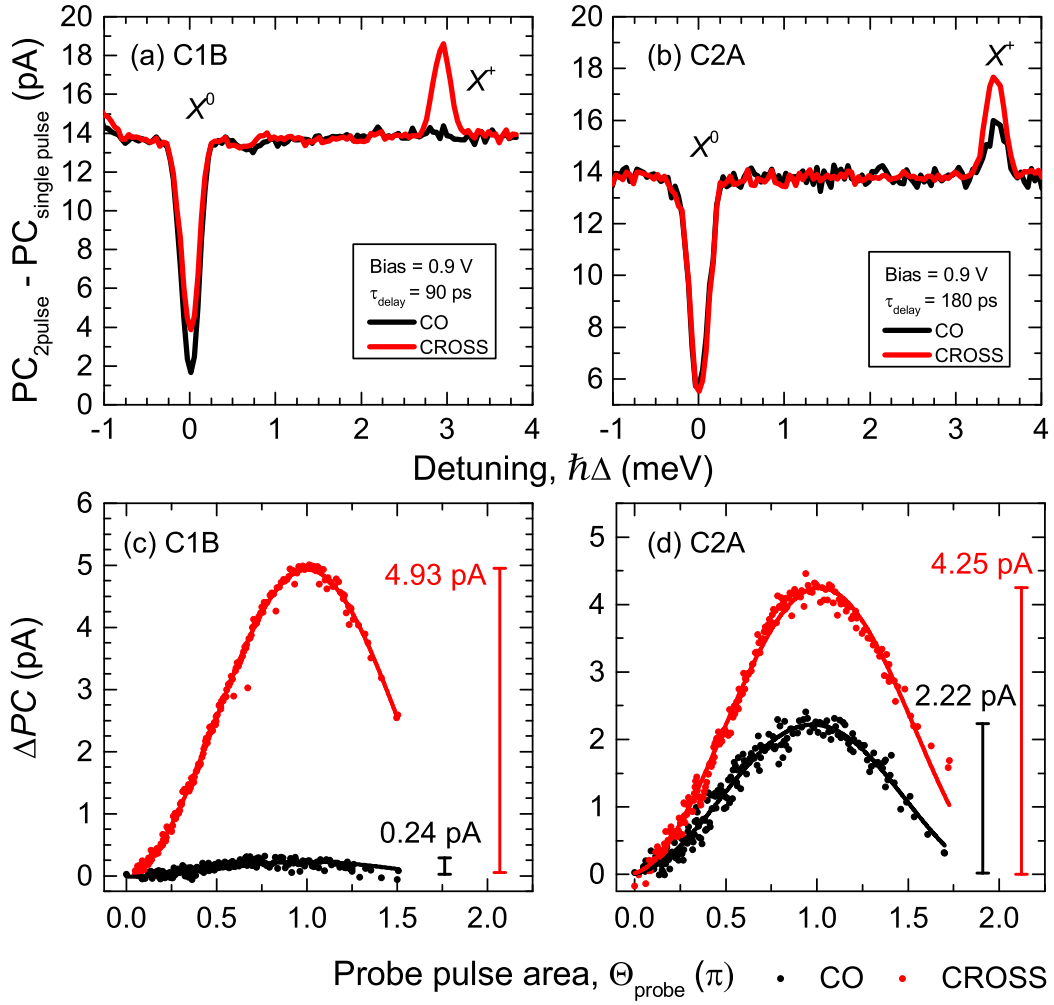

Figure C.1: Two pulse differential spectra showing the positive trion ($\mathrm{h}-X^+$) transition for C1B (a) and C2A (b). In both graphs the single-pulse spectrum is subtracted in order to remove any background features from the spectrum.

The spectra both show the $\mathrm{h}-X^+$ peak positively detuned from the neutral exciton transition by ~3 meV. The dip at the exciton resonance is an artifact from subtracting the single-pulse spectrum and not an inversion signature. For ideal spin preparation, no peak should be observed in the co-polarized trace as the presence of the hole prevents

absorption of the co-polarized probe pulse resonant with this transition. The contrast between the co and cross-polarized peaks is much greater for C1B (low $\hbar\delta$) than for C2A. The hole spin preparation fidelity is limited by the time that the exciton can precess due to the fine structure before the electron tunnels out of the QD. In these measurements, the bias was 0.9 V, so fast electron tunneling is expected (>30 ps, as in fig. 4.5). For C2A, this is enough time for the exciton to precess between the circularly polarized fine-structure split superposition states $|\Downarrow\uparrow\rangle$ and $|\Uparrow\downarrow\rangle$ before the electron tunnels, leading to the poor contrast in the trion peak for co and cross polarized excitation. For C1B, the small fine-structure means that the exciton does not precess very far out of the initially excited $|\Uparrow\downarrow\rangle$ state before the electron tunnels and the contrast is very high between the trion peaks in the two spectra.

C.3 Hole spin preparation fidelity

To quantify the spin preparation fidelity, a conditional Rabi rotation measurement was performed on the trion transitions. Here, the energy of the probe pulse was fixed to be resonant with h$-X^+$, and its pulse area increased. The results of these measuremnents are presented in fig. C.1 (c) for C1B, and (d) for C2A. The contrast from the trion peaks in (a) and (b) is replicated by the conditional rotation measurements. The curves in (c) and (d) are fits to the data and the amplitudes of the rotation: $\Delta PC_{\Uparrow-\Uparrow\Downarrow\uparrow}$ and $\Delta PC_{\Downarrow-\Downarrow\Uparrow\downarrow}$ are extracted and take the respective values: 4.93 ± 0.012 pA and 0.24 ± 0.012 pA for C1B and 4.25 ± 0.019 pA and 2.22 ± 0.019 pA for C2A. The experimental spin preparation fidelity F_{PC} is calculated by eq. (C.1) [82].

$$F_{PC} = \frac{\Delta PC_{\Uparrow-\Uparrow\Downarrow\uparrow}}{\Delta PC_{\Uparrow-\Uparrow\Downarrow\uparrow} + \Delta PC_{\Downarrow-\Downarrow\Uparrow\downarrow}}. \tag{C.1}$$

Using eq. (C.1), we can obtain $F_{PC}^{\mathrm{C1B}} = 0.954 \pm 0.004$, and $F_{PC}^{\mathrm{C2A}} = 0.65 \pm 0.004$. The extremely high spin preparation fidelity is currently the highest value reported for a single QD without the application of a magnetic field, and is similar to the value obtained in QD molecule experiments [84]. For comparison, the QD examined in ref. [82] shows $F_{PC} = 0.81$ when B = 0. A detailed mathematical description of the hole spin preparation model is also included in this reference. The QD C1B, which is studied here exhibits both a very low fine structure splitting and also a high hole spin preparation fidelity, supporting the model that hole spin information is lost due to the fine-structure precession of the neutral exciton before the electron tunnels out of the QD.

Bibliography

[1] G. E. Moore, "Cramming more components onto integrated circuits," *Electronics*, vol. 38, no. 8, 1965.

[2] R. P. Feynman, "Simulating physics with computers," *Int. J. Theor. Phys.*, vol. 21, pp. 467–488, June 1982.

[3] D. Deutsch, "Quantum theory , the Church-Turing principle and the universal quantum computer," *Proc. R. Soc. London*, vol. 400, no. 1818, pp. 97–117, 1985.

[4] P. W. Shor, "Polynomial-Time Algorithms for Prime Factorization and Discrete Logarithms on a Quantum Computer," *SIAM J. Comput.*, vol. 26, pp. 1484–1509, Oct. 1997.

[5] D. P. DiVincenzo, "The Physical Implementation of Quantum Computation," *Fortschritte Phys.*, vol. 48, no. 771, 2000.

[6] D. P. DiVincenzo, "Two-bit gates are universal for quantum computation," *Phys. Rev. A*, vol. 51, no. 2, pp. 1015–1022, 1995.

[7] P. Kok, K. Nemoto, T. C. Ralph, J. P. Dowling, and G. J. Milburn, "Linear optical quantum computing with photonic qubits," *Rev. Mod. Phys.*, vol. 79, pp. 135–174, Jan. 2007.

[8] J. I. Cirac and P. Zoller, "Quantum Computations with Cold Trapped Ions," *Phys. Rev. Lett.*, vol. 74, no. 20, p. 4091, 1995.

[9] C. Monroe, D. M. Meekhof, B. E. King, W. M. Itano, and D. J. Wineland, "Demonstration of a Fundamental Quantum Logic Gate," *Phys. Rev. Lett.*, vol. 75, no. 25, p. 4714, 1995.

[10] F. Jelezko, T. Gaebel, I. Popa, A. Gruber, and J. Wrachtrup, "Observation of Coherent Oscillations in a Single Electron Spin," *Phys. Rev. Lett.*, vol. 92, p. 076401, Feb. 2004.

[11] K. Saeedi, S. Simmons, J. Z. Salvail, P. Dluhy, H. Riemann, N. V. Abrosimov, P. Becker, H.-J. Pohl, J. J. L. Morton, and M. L. W. Thewalt, "Room-

Temperature Quantum Bit Storage Exceeding 39 Minutes Using Ionized Donors in Silicon-28," *Science*, vol. 342, pp. 830–833, Nov. 2013.

[12] L. M. K. Vandersypen, "NMR techniques for quantum control and computation," *Rev. Mod. Phys.*, vol. 76, pp. 1037–1069, 2004.

[13] G. Wendin and V. S. Shumeiko, "Quantum bits with Josephson junctions (Review Article)," *Low Temp. Phys.*, vol. 33, no. 9, p. 724, 2007.

[14] A. J. Ramsay, "A review of the coherent optical control of the exciton and spin states of semiconductor quantum dots," *Semicond. Sci. Technol.*, vol. 25, p. 103001, 2010.

[15] T. Ishikawa, S. Kohmoto, and K. Asakawa, "Site control of self-organized InAs dots on GaAs substrates by in situ electron-beam lithography and molecular-beam epitaxy," *Appl. Phys. Lett.*, vol. 73, no. 12, p. 1712, 1998.

[16] M. H. Baier, S. Watanabe, E. Pelucchi, and E. Kapon, "High uniformity of site-controlled pyramidal quantum dots grown on prepatterned substrates," *Appl. Phys. Lett.*, vol. 84, no. 11, p. 1943, 2004.

[17] K. H. Lee, A. M. Green, R. A. Taylor, D. N. Sharp, J. Scrimgeour, O. M. Roche, J. H. Na, A. F. Jarjour, A. J. Turberfield, F. S. F. Brossard, D. A. Williams, and G. A. D. Briggs, "Registration of single quantum dots using cryogenic laser photolithography," *Appl. Phys. Lett.*, vol. 88, no. 19, p. 193106, 2006.

[18] D. Leonard, M. Krishnamurthy, C. M. Reaves, S. P. Denbaars, and P. M. Petroff, "Direct formation of quantum-sized dots from uniform coherent islands of InGaAs on GaAs surfaces," *Appl. Phys. Lett.*, vol. 63, no. 23, p. 3203, 1993.

[19] D. M. Bruls, J. W. A. M. Vugs, P. M. Koenraad, H. W. M. Salemink, J. H. Wolter, M. Hopkinson, M. S. Skolnick, F. Long, and S. P. A. Gill, "Determination of the shape and indium distribution of low-growth-rate InAs quantum dots by cross-sectional scanning tunneling microscopy," *Appl. Phys. Lett.*, vol. 81, no. 9, p. 1708, 2002.

[20] P. Hawrylak and M. Korkusinki, "Electronic Properties of Self-Assembled Quantum Dots," in *Single Quantum Dots Fundamentals, Applications and New Concpets* (P. M. Petroff, ed.), ch. 2, pp. 25–91, Springer, 2003.

[21] Y. H. Huo, B. J. Witek, S. Kumar, J. R. Cardenas, J. X. Zhang, N. Akopian, R. Singh, E. Zallo, R. Grifone, D. Kriegner, R. Trotta, F. Ding, J. Stangl, V. Zwiller, G. Bester, A. Rastelli, and O. G. Schmidt, "A light-hole exciton in a quantum dot," *Nat. Phys.*, vol. 9, Nov. 2013.

[22] T. Belhadj, T. Amand, A. Kunold, C.-M. Simon, T. Kuroda, M. Abbarchi, T. Mano, K. Sakoda, S. Kunz, X. Marie, and B. Urbaszek, "Impact of heavy hole-light hole coupling on optical selection rules in GaAs quantum dots," *Appl. Phys. Lett.*, vol. 97, no. 5, p. 051111, 2010.

[23] A. Koudinov, I. Akimov, Y. Kusrayev, and F. Henneberger, "Optical and magnetic anisotropies of the hole states in Stranski-Krastanov quantum dots," *Phys. Rev. B*, vol. 70, p. 241305, Dec. 2004.

[24] P. W. Fry, I. E. Itskevich, D. J. Mowbray, M. S. Skolnick, J. J. Finley, J. A. Barker, E. P. O'Reilly, L. R. Wilson, I. A. Larkin, P. A. Maksym, M. Hopkinson, M. Al-Khafaji, J. P. David, A. G. Cullis, G. Hill, and J. C. Clark, "Inverted electron-hole alignment in InAs-GaAs self-assembled quantum dots.," *Phys. Rev. Lett.*, vol. 84, pp. 733–6, Jan. 2000.

[25] R. Seguin, A. Schliwa, S. Rodt, K. Pötschke, U. Pohl, and D. Bimberg, "Size-Dependent Fine-Structure Splitting in Self-Organized InAs/GaAs Quantum Dots," *Phys. Rev. Lett.*, vol. 95, p. 257402, Dec. 2005.

[26] R. M. Stevenson, R. J. Young, P. Atkinson, K. Cooper, D. A. Ritchie, and A. J. Shields, "A semiconductor source of triggered entangled photon pairs.," *Nature*, vol. 439, pp. 179–82, Jan. 2006.

[27] N. Akopian, N. Lindner, E. Poem, Y. Berlatzky, J. Avron, D. Gershoni, B. Gerardot, and P. Petroff, "Entangled Photon Pairs from Semiconductor Quantum Dots," *Phys. Rev. Lett.*, vol. 96, p. 130501, Apr. 2006.

[28] N. Kleemans, J. van Bree, M. Bozkurt, P. van Veldhoven, P. Nouwens, R. Nötzel, A. Silov, P. Koenraad, and M. Flatté, "Size-dependent exciton g factor in self-assembled InAs/InP quantum dots," *Phys. Rev. B*, vol. 79, p. 045311, Jan. 2009.

[29] M. Bayer, S. Walck, T. Reinecke, and A. Forchel, "Exciton binding energies and diamagnetic shifts in semiconductor quantum wires and quantum dots," *Phys. Rev. B*, vol. 57, pp. 6584–6591, Mar. 1998.

[30] M. Bayer, G. Ortner, O. Stern, A. Kuther, A. Gorbunov, A. Forchel, P. Hawrylak, S. Fafard, K. Hinzer, T. Reinecke, S. Walck, J. Reithmaier, F. Klopf, and F. Schäfer, "Fine structure of neutral and charged excitons in self-assembled In(Ga)As/(Al)GaAs quantum dots," *Phys. Rev. B*, vol. 65, May 2002.

[31] A. Schwan, B. Meiners, A. Greilich, D. R. Yakovlev, M. Bayer, and A. D. B. Maia, "Anisotropy of electron and hole g-factors in (In,Ga)As quantum dots," *Appl. Phys. Lett.*, vol. 221914, p. 221914, 2011.

[32] T. M. Godden, J. H. Quilter, A. J. Ramsay, Y. Wu, P. Brereton, S. J. Boyle, I. J. Luxmoore, J. Puebla-Nunez, A. M. Fox, and M. S. Skolnick, "Coherent Optical Control of the Spin of a Single Hole in an InAs/GaAs Quantum Dot," *Phys. Rev. Lett.*, vol. 108, p. 017402, Jan. 2012.

[33] J. J. Finley, M. Sabathil, P. Vogl, G. Abstreiter, R. Oulton, A. I. Tartakovskii, D. J. Mowbray, M. S. Skolnick, S. Liew, A. Cullis, and M. Hopkinson, "Quantum-confined Stark shifts of charged exciton complexes in quantum dots," *Phys. Rev. B*, vol. 70, p. 201308 (R), Nov. 2004.

[34] R. Warburton, C. Schaflein, D. Haft, F. Bickel, A. Lorke, K. Karrai, J. Garcia, W. Schoenfeld, and P. Petroff, "Optical emission from a charge-tunable quantum ring," *Nature*, vol. 405, p. 926, June 2000.

[35] P. W. Fry, I. E. Itskevich, S. R. Parnell, J. J. Finley, L. R. Wilson, K. L. Schumacher, D. J. Mowbray, M. S. Skolnick, M. Al-Khafaji, A. G. Cullis, M. Hopkinson, J. C. Clark, and G. Hill, "Photocurrent spectroscopy of InAs/GaAs self-assembled quantum dots," *Phys. Rev. B*, vol. 62, p. 16784, Dec. 2000.

[36] M. Baier, F. Findeis, A. Zrenner, M. Bichler, and G. Abstreiter, "Optical spectroscopy of charged excitons in single quantum dot photodiodes," *Phys. Rev. B*, vol. 64, p. 195326, 2001.

[37] D. Regelman, E. Dekel, D. Gershoni, E. Ehrenfreund, A. Williamson, J. Shumway, A. Zunger, W. Schoenfeld, and P. Petroff, "Optical spectroscopy of single quantum dots at tunable positive, neutral, and negative charge states," *Phys. Rev. B*, vol. 64, p. 165301, Sept. 2001.

[38] K. Kowalik, O. Krebs, A. Lemaître, S. Laurent, P. Senellart, P. Voisin, and J. A. Gaj, "Influence of an in-plane electric field on exciton fine structure in InAs-GaAs self-assembled quantum dots," *Appl. Phys. Lett.*, vol. 86, no. 4, p. 041907, 2005.

[39] B. D. Gerardot, S. Seidl, P. A. Dalgarno, R. J. Warburton, D. Granados, J. M. Garcia, K. Kowalik, O. Krebs, K. Karrai, A. Badolato, and P. M. Petroff, "Manipulating exciton fine structure in quantum dots with a lateral electric field," *Appl. Phys. Lett.*, vol. 90, no. 4, p. 041101, 2007.

[40] T. Stievater, X. Li, D. Steel, D. Gammon, D. Katzer, D. Park, C. Piermarocchi, and L. Sham, "Rabi Oscillations of Excitons in Single Quantum Dots," *Phys. Rev. Lett.*, vol. 87, p. 133603, Sept. 2001.

[41] A. M. Fox, *Quantum Optics: An Introduction.* Oxford University Press, 2006.

[42] F. Bloch, "Nuclear Induction," *Phys. Rev.*, vol. 70, no. 7, pp. 460–473, 1946.

[43] N. Bonadeo, J. Erland, D. Gammon, D. Park, D. Katzer, and D. Steel, "Coherent optical control of the quantum state of a single quantum Dot," *Science*, vol. 282, pp. 1473–6, Nov. 1998.

[44] Y. Toda, T. Sugimoto, M. Nishioka, and Y. Arakawa, "Near-field coherent excitation spectroscopy of InGaAs/GaAs self-assembled quantum dots," *Appl. Phys. Lett.*, vol. 76, no. 26, p. 3887, 2000.

[45] H. Kamada, H. Gotoh, J. Temmyo, T. Takagahara, and H. Ando, "Exciton Rabi Oscillation in a Single Quantum Dot," *Phys. Rev. Lett.*, vol. 87, pp. 10–13, Nov. 2001.

[46] H. Htoon, T. Takagahara, D. Kulik, O. Baklenov, A. Holmes, and C. Shih, "Interplay of Rabi Oscillations and Quantum Interference in Semiconductor Quantum Dots," *Phys. Rev. Lett.*, vol. 88, p. 087401, Feb. 2002.

[47] L. Besombes, J. Baumberg, and J. Motohisa, "Coherent Spectroscopy of Optically Gated Charged Single InGaAs Quantum Dots," *Phys. Rev. Lett.*, vol. 90, p. 257402, June 2003.

[48] H. Htoon, D. Kulik, O. Baklenov, A. Holmes, T. Takagahara, and C. Shih, "Carrier relaxation and quantum decoherence of excited states in self-assembled quantum dots," *Phys. Rev. B*, vol. 63, p. 241303, June 2001.

[49] Q. Wang, A. Muller, P. Bianucci, E. Rossi, Q. Xue, T. Takagahara, C. Piermarocchi, A. MacDonald, and C. Shih, "Decoherence processes during optical manipulation of excitonic qubits in semiconductor quantum dots," *Phys. Rev. B*, vol. 72, p. 035306, July 2005.

[50] Q. Wang, A. Muller, M. Cheng, H. Zhou, P. Bianucci, and C. Shih, "Coherent Control of a V-Type Three-Level System in a Single Quantum Dot," *Phys. Rev. Lett.*, vol. 95, p. 187404, Oct. 2005.

[51] A. Zrenner, E. Beham, S. Stufler, F. Findeis, M. Bichler, and G. Abstreiter, "Coherent properties of a two-level system based on a quantum-dot photodiode.," *Nature*, vol. 418, p. 612, Aug. 2002.

[52] B. Patton, U. Woggon, and W. Langbein, "Coherent Control and Polarization Readout of Individual Excitonic States," *Phys. Rev. Lett.*, vol. 95, p. 266401, Dec. 2005.

[53] A. J. Ramsay, R. S. Kolodka, F. Bello, P. Fry, W. K. Ng, A. Tahraoui, H. Liu, M. Hopkinson, D. Whittaker, A. M. Fox, and M. S. Skolnick, "Coherent response of a quantum dot exciton driven by a rectangular spectrum optical pulse," *Phys. Rev. B*, vol. 75, p. 113302, Mar. 2007.

[54] H. Takagi, T. Nakaoka, K. Watanabe, N. Kumagai, and Y. Arakawa, "Coherently driven semiconductor quantum dot at a telecommunication wavelength.," *Opt. Express*, vol. 16, pp. 13949–54, Sept. 2008.

[55] R. Melet, V. Voliotis, A. Enderlin, D. Roditchev, X. Wang, T. Guillet, and R. Grousson, "Resonant excitonic emission of a single quantum dot in the Rabi regime," *Phys. Rev. B*, vol. 78, p. 073301, Aug. 2008.

[56] X. Xu, B. Sun, P. R. Berman, D. G. Steel, A. S. Bracker, D. Gammon, and L. J. Sham, "Coherent optical spectroscopy of a strongly driven quantum dot," *Science*, vol. 317, p. 929, 2007.

[57] G. Jundt, L. Robledo, A. Högele, S. Fält, and A. Imamolu, "Observation of Dressed Excitonic States in a Single Quantum Dot," *Phys. Rev. Lett.*, vol. 100, p. 177401, Apr. 2008.

[58] M. Kroner, C. Lux, S. Seidl, A. W. Holleitner, K. Karrai, A. Badolato, P. M. Petroff, and R. J. Warburton, "Rabi splitting and ac-Stark shift of a charged exciton," *Appl. Phys. Lett.*, vol. 92, no. 3, p. 031108, 2008.

[59] S. J. Boyle, A. J. Ramsay, A. M. Fox, A. P. Heberle, and M. Hopkinson, "Beating of exciton-dressed states in a single semiconductor InGaAs/GaAs quantum dot," *Phys. Rev. Lett.*, vol. 102, p. 207401, May 2009.

[60] B. D. Gerardot, D. Brunner, P. A. Dalgarno, K. Karrai, A. Badolato, P. M. Petroff, and R. J. Warburton, "Dressed excitonic states and quantum interference in a three-level quantum dot ladder system," *New J. Phys.*, vol. 11, p. 013028, Jan. 2009.

[61] A. N. Vamivakas, Y. Zhao, C.-Y. Lu, and M. Atatüre, "Spin-resolved quantum-dot resonance fluorescence," *Nat. Phys.*, vol. 5, pp. 198–202, Jan. 2009.

[62] E. B. Flagg, A. Muller, J. W. Robertson, S. Founta, D. G. Deppe, M. Xiao, W. Ma, G. J. Salamo, and C. K. Shih, "Resonantly driven coherent oscillations in a solid-state quantum emitter," *Nat. Phys.*, vol. 5, pp. 203–207, Jan. 2009.

[63] S. Stufler, P. Ester, A. Zrenner, and M. Bichler, "Quantum optical properties of a single $In_xGa_{1x}As$-GaAs quantum dot two-level system," *Phys. Rev. B*, vol. 72, p. 121301(R), Sept. 2005.

[64] R. S. Kolodka, A. J. Ramsay, J. Skiba-Szymanska, P. W. Fry, H. Y. Liu, A. M. Fox, and M. S. Skolnick, "Inversion recovery of single quantum-dot exciton based qubit," *Phys. Rev. B*, vol. 75, p. 193306, May 2007.

[65] S. Stufler, P. Ester, A. Zrenner, and M. Bichler, "Ramsey Fringes in an Electric-Field-Tunable Quantum Dot System," *Phys. Rev. Lett.*, vol. 96, p. 037402, Jan. 2006.

[66] Y. Kodriano, I. Schwartz, E. Poem, Y. Benny, R. Presman, T. Truong, P. Petroff, and D. Gershoni, "Complete control of a matter qubit using a single picosecond laser pulse," *Phys. Rev. B*, vol. 85, p. 241304, June 2012.

[67] S. Economou, L. Sham, Y. Wu, and D. Steel, "Proposal for optical U(1) rotations of electron spin trapped in a quantum dot," *Phys. Rev. B*, vol. 74, Nov. 2006.

[68] S. Economou and T. Reinecke, "Theory of Fast Optical Spin Rotation in a Quantum Dot Based on Geometric Phases and Trapped States," *Phys. Rev. Lett.*, vol. 99, p. 217401, Nov 2007.

[69] K. Müller, T. Kaldewey, R. Ripszam, J. S. Wildmann, A. Bechtold, M. Bichler, G. Koblmüller, G. Abstreiter, and J. J. Finley, "All optical quantum control of a spin-quantum state and ultrafast transduction into an electric current.," *Sci. Rep.*, vol. 3, p. 1906, Jan. 2013.

[70] X. Li, Y. Wu, D. Steel, D. Gammon, T. H. Stievater, D. S. Katzer, D. Park, C. Piermarocchi, and L. J. Sham, "An all-optical quantum gate in a semiconductor quantum dot.," *Science*, vol. 301, pp. 809–11, Aug. 2003.

[71] S. J. Boyle, A. J. Ramsay, F. Bello, H. Y. Liu, M. Hopkinson, A. M. Fox, and M. S. Skolnick, "Two-qubit conditional quantum-logic operation in a single self-assembled quantum dot," *Phys. Rev. B*, vol. 78, p. 075301, Aug. 2008.

[72] S. Stufler, P. Machnikowski, P. Ester, M. Bichler, V. Axt, T. Kuhn, and A. Zrenner, "Two-photon Rabi oscillations in a single $In_xGa_{1x}AsGaAs$ quantum dot," Mar. 2006.

[73] T. Flissikowski, A. Betke, I. Akimov, and F. Henneberger, "Two-Photon Coherent Control of a Single Quantum Dot," *Phys. Rev. Lett.*, vol. 92, p. 227401, June 2004.

[74] D. Press, T. D. Ladd, B. Zhang, and Y. Yamamoto, "Complete quantum control of a single quantum dot spin using ultrafast optical pulses.," *Nature*, vol. 456, pp. 218–21, Nov. 2008.

[75] M. Atatüre, J. Dreiser, A. Badolato, A. Högele, K. Karrai, and A. Imamoglu, "Quantum-dot spin-state preparation with near-unity fidelity.," *Science*, vol. 312, pp. 551–3, Apr. 2006.

[76] J. M. Elzerman, R. Hanson, L. H. Willems van Beveren, B. Witkamp, L. M. K. Vandersypen, and L. P. Kouwenhoven, "Single-shot read-out of an individual electron spin in a quantum dot," *Nature*, vol. 430, pp. 431–435, 2004.

[77] M. Kroutvar, Y. Ducommun, D. Heiss, M. Bichler, D. Schuh, G. Abstreiter, and J. J. Finley, "Optically programmable electron spin memory using semiconductor quantum dots," *Nature*, vol. 432, no. 7013, pp. 81–84, 2004.

[78] X. Xu, Y. Wu, B. Sun, Q. Huang, J. Cheng, D. G. Steel, A. S. Bracker, D. Gammon, C. Emary, and L. J. Sham, "Fast spin state initialization in a singly charged inas-gaas quantum dot by optical cooling," *Phys. Rev. Lett.*, vol. 99, p. 097401, 2007.

[79] B. D. Gerardot, D. Brunner, P. A. Dalgarno, P. Ohberg, S. Seidl, M. Kroner, K. Karrai, N. G. Stoltz, P. M. Petroff, and R. J. Warburton, "Optical pumping of a single hole spin in a quantum dot.," *Nature*, vol. 451, pp. 441–4, Jan 2008.

[80] X. Xu, B. Sun, P. R. Berman, D. G. Steel, A. S. Bracker, D. Gammon, and L. J. Sham, "Coherent population trapping of an electron spin in a single negatively charged quantum dot," *Nat. Phys.*, vol. 4, pp. 692–695, Aug. 2008.

[81] D. Brunner, B. D. Gerardot, P. a. Dalgarno, G. Wüst, K. Karrai, N. G. Stoltz, P. M. Petroff, and R. J. Warburton, "A coherent single-hole spin in a semiconductor.," *Science*, vol. 325, pp. 70–2, Jul 2009.

[82] T. M. Godden, S. J. Boyle, A. J. Ramsay, A. M. Fox, and M. S. Skolnick, "Fast high fidelity hole spin initialization in a single InGaAs quantum dot," *Appl. Phys. Lett.*, vol. 97, no. 6, p. 061113, 2010.

[83] T. M. Godden, J. H. Quilter, A. J. Ramsay, Y. Wu, P. Brereton, I. Luxmoore, J. Puebla, A. M. Fox, and M. S. Skolnick, "Fast preparation of a single-hole spin in an InAs/GaAs quantum dot in a Voigt-geometry magnetic field," *Phys. Rev. B*, vol. 85, p. 155310, Apr. 2012.

[84] K. Müller, A. Bechtold, C. Ruppert, C. Hautmann, J. S. Wildmann, T. Kaldewey, M. Bichler, H. J. Krenner, G. Abstreiter, M. Betz, and J. J. Finley, "High-fidelity optical preparation and coherent Larmor precession of a single hole in an (In,Ga)As quantum dot molecule," *Phys. Rev. B*, vol. 85, p. 341306(R), June 2012.

[85] P. Chen, C. Piermarocchi, L. Sham, D. Gammon, and D. Steel, "Theory of quantum optical control of a single spin in a quantum dot," *Phys. Rev. B*, vol. 69, p. 075320, Feb. 2004.

[86] J. Berezovsky, M. H. Mikkelsen, N. G. Stoltz, L. A. Coldren, and D. D. Awschalom, "Picosecond coherent optical manipulation of a single electron spin in a quantum dot.," *Science*, vol. 320, pp. 349–52, Apr. 2008.

[87] O. Gywat, H. J. Krenner, and J. Berezovsky, *Spins in Optically Active Quantum Dots - concepts and methods*. Wiley-VCH, 2010.

[88] G. Solomon, J. Trezza, A. Marshall, and J. Harris, "Vertically aligned and electronically coupled growth induced InAs islands in GaAs.," *Phys. Rev. Lett.*, vol. 76, pp. 952–955, Feb. 1996.

[89] D. Kim, S. G. Carter, A. Greilich, A. S. Bracker, and D. Gammon, "Ultrafast optical control of entanglement between two quantum-dot spins," *Nat. Phys.*, vol. 7, pp. 223–229, Dec. 2010.

[90] A. Greilich, S. G. Carter, D. Kim, A. S. Bracker, and D. Gammon, "Optical control of one and two hole spins in interacting quantum dots," *Nat. Photonics*, vol. 5, pp. 702–708, 2011.

[91] W. Langbein, P. Borri, U. Woggon, V. Stavarache, D. Reuter, and A. D. Wieck, "Radiatively limited dephasing in InAs quantum dots," *Phys. Rev. B*, vol. 70, p. 033301, July 2004.

[92] P. A. Dalgarno, J. M. Smith, J. McFarlane, B. D. Gerardot, K. Karrai, A. Badolato, P. M. Petroff, and R. J. Warburton, "Coulomb interactions in single charged self-assembled quantum dots: Radiative lifetime and recombination energy," *Phys. Rev. B*, vol. 77, p. 245311, 2008.

[93] A. J. Ramsay, A. V. Gopal, E. M. Gauger, A. Nazir, B. W. Lovett, A. M. Fox, and M. S. Skolnick, "Damping of Exciton Rabi Rotations by Acoustic Phonons in Optically Excited InGaAs/GaAs Quantum Dots," *Phys. Rev. Lett.*, vol. 104, p. 017402, Jan. 2010.

[94] A. J. Ramsay, T. M. Godden, S. J. Boyle, E. M. Gauger, A. Nazir, B. W. Lovett, A. M. Fox, and M. S. Skolnick, "Phonon-Induced Rabi-Frequency Renormalization of Optically Driven Single InGaAs/GaAs Quantum Dots," *Phys. Rev. Lett.*, vol. 105, p. 177402, Oct. 2010.

[95] A. J. Ramsay, T. M. Godden, S. J. Boyle, E. M. Gauger, A. Nazir, B. W. Lovett, A. V. Gopal, A. M. Fox, and M. S. Skolnick, "Effect of detuning on the phonon induced dephasing of optically driven InGaAs/GaAs quantum dots," *J. Appl. Phys.*, vol. 109, no. 10, p. 102415, 2011.

[96] R. Hanson, J. R. Petta, S. Tarucha, and L. M. K. Vandersypen, "Spins in few-electron quantum dots," *Rev. Mod. Phys.*, vol. 79, pp. 1217–1265, Oct. 2007.

[97] D. Zumbühl, J. Miller, C. Marcus, K. Campman, and A. Gossard, "Spin-Orbit Coupling, Antilocalization, and Parallel Magnetic Fields in Quantum Dots," *Phys. Rev. Lett.*, vol. 89, p. 276803, Dec. 2002.

[98] D. J. Hilton and C. L. Tang, "Optical Orientation and Femtosecond Relaxation of Spin-Polarized Holes in GaAs," *Phys. Rev. Lett.*, vol. 89, p. 146601, Sept. 2002.

[99] C. Lü, J. Cheng, and M. Wu, "Hole spin relaxation in semiconductor quantum dots," *Phys. Rev. B*, vol. 71, p. 075308, Feb. 2005.

[100] D. Heiss, S. Schaeck, H. Huebl, M. Bichler, G. Abstreiter, J. J. Finley, D. V. Bulaev, and D. Loss, "Observation of extremely slow hole spin relaxation in self-assembled quantum dots," *Phys. Rev. B*, vol. 76, p. 241306(R), Dec. 2007.

[101] V. N. Golovach, A. Khaetskii, and D. Loss, "Phonon-Induced Decay of the Electron Spin in Quantum Dots," *Phys. Rev. Lett.*, vol. 93, p. 016601, June 2004.

[102] I. A. Merkulov, A. L. Efros, and M. Rosen, "Electron spin relaxation by nuclei in semiconductor quantum dots," *Phys. Rev. B*, vol. 65, p. 205309, 2002.

[103] J. Fischer, W. Coish, D. Bulaev, and D. Loss, "Spin decoherence of a heavy hole coupled to nuclear spins in a quantum dot," *Phys. Rev. B*, vol. 78, no. 15, p. 155329, 2008.

[104] C. Testelin, F. Bernardot, B. Eble, and M. Chamarro, "Hole˘spin dephasing time associated with hyperfine interaction in quantum dots," *Phys. Rev. B*, vol. 79, p. 195440, 2009.

[105] P. Fallahi, S. Ylmaz, and A. Imamolu, "Measurement of a Heavy-Hole Hyperfine Interaction in InGaAs Quantum Dots Using Resonance Fluorescence," *Phys. Rev. Lett.*, vol. 105, p. 257402, Dec. 2010.

[106] E. A. Chekhovich, A. B. Krysa, M. S. Skolnick, and A. I. Tartakovskii, "Direct Measurement of the Hole-Nuclear Spin Interaction in Single InP/GaInP Quantum Dots Using Photoluminescence Spectroscopy," *Phys. Rev. Lett.*, vol. 106, p. 027402, Jan. 2011.

[107] E. A. Chekhovich, M. Hopkinson, M. S. Skolnick, and A. I. Tartakovskii, "Quadrupolar induced suppression of nuclear spin bath fluctuations in self-assembled quantum dots," *arXiv*, 2014. arXvID:1403.1510v2, accepted for publication in Nature Communications.

[108] K. De Greve, P. L. Mcmahon, D. Press, T. D. Ladd, Y. Yamamoto, D. Bisping, C. Schneider, M. Kamp, L. Worschech, A. Forchel, and S. Hofling, "Coherent Control and Suppressed Nuclear Feedback of a Single Quantum Dot Hole Qubit," *Nat. Phys.*, vol. 7, pp. 872–878, 2011.

[109] D. Press, K. D. Greve, P. L. Mcmahon, T. D. Ladd, B. Friess, A. Forchel, Y. Yamamoto, C. Schneider, M. Kamp, and S. Ho, "Ultrafast optical spin echo in a single quantum dot," *Nat. Photonics*, vol. 4, no. April, pp. 367–370, 2010.

[110] K. Müller, G. Reithmaier, E. C. Clark, V. Jovanov, M. Bichler, H. J. Krenner, M. Betz, G. Abstreiter, and J. J. Finley, "Excited state quantum couplings and optical switching of an artificial molecule," *Phys. Rev. B*, vol. 84, p. 081302(R), Aug. 2011.

[111] Y. Wu, I. M. Piper, M. Ediger, P. Brereton, E. R. Schmidgall, P. R. Eastham, M. Hugues, M. Hopkinson, and R. T. Phillips, "Population Inversion in a Single InGaAs Quantum Dot Using the Method of Adiabatic Rapid Passage," *Phys. Rev. Lett.*, vol. 106, p. 067401, Feb. 2011.

[112] C. Kistner, S. Reitzenstein, C. Schneider, S. Hofling, and A. Forchel, "Resonantly probing micropillar cavity modes by photocurrent spectroscopy," *Appl. Phys. Lett.*, vol. 94, no. 22, p. 221103, 2009.

[113] G. Bulgarini, M. E. Reimer, M. Hocevar, P. A. M. Bakkers, Erik, L. P. Kouwenhoven, and V. Zwiller, "Avalanche amplification of a single exciton in a semiconductor nanowire," *Nat. photonics.*, vol. 6, pp. 455–458, 2012.

[114] A. M. Weiner, "Femtosecond pulse shaping using spatial light modulators," *Rev. Sci. Instrum.*, vol. 71, no. 5, p. 1929, 2000.

[115] A. M. Weiner, "Ultrafast optical pulse shaping: A tutorial review," *Opt. Commun.*, vol. 284, pp. 3669–3692, July 2011.

[116] P. W. Fry, J. J. Finley, L. R. Wilson, A. Lemaître, D. J. Mowbray, M. S. Skolnick, M. Hopkinson, G. Hill, and J. C. Clark, "Electric-field-dependent carrier capture and escape in self-assembled InAs_GaAs quantum dots," *Appl. Phys. Lett.*, vol. 77, no. 26, pp. 4344–4346, 2000.

[117] A. Bennett, M. Pooley, R. Stevenson, M. Ward, R. Patel, A. B. de La Giroday, N. Sköld, I. Farrer, C. Nicoll, D. Ritchie, *et al.*, "Electric-field-induced coherent coupling of the exciton states in a single quantum dot," *Nature Physics*, vol. 6, no. 12, pp. 947–950, 2010.

[118] R. Trotta, E. Zallo, C. Ortix, P. Atkinson, J. D. Plumhof, J. van den Brink, A. Rastelli, and O. G. Schmidt, "Universal recovery of the energy-level degeneracy of bright excitons in ingaas quantum dots without a structure symmetry," *Phys. Rev. Lett.*, vol. 109, p. 147401, 2012.

[119] J. D. Mar, X. L. Xu, J. J. Baumberg, A. C. Irvine, C. Stanley, and D. A. Williams, "Electrically tunable hole tunnelling from a single self-assembled quantum dot embedded in an n-i-Schottky photovoltaic cell," *Appl. Phys. Lett.*, vol. 99, no. 3, p. 031102, 2011.

[120] J. H. Quilter, R. J. Coles, A. J. Ramsay, A. M. Fox, and M. S. Skolnick, "Enhanced photocurrent readout for a quantum dot qubit by bias modulation," *Appl. Phys. Lett.*, vol. 102, no. 18, p. 181108, 2013.

[121] S. M. de Vasconcellos, S. Gordon, M. Bichler, T. Meier, and A. Zrenner, "Coherent control of a single exciton qubit by optoelectronic manipulation," *Nat. Photonics*, vol. 124, no. June, p. 545, 2010.

[122] B. Alen, F. Bickel, K. Karrai, R. J. Warburton, and P. M. Petroff, "Stark-shift modulation absorption spectroscopy of single quantum dots," *Appl. Phys. Lett.*, vol. 83, no. 11, p. 2235, 2003.

[123] R. J. Warburton, C. S. Dürr, K. Karrai, J. P. Kotthaus, and P. M. Petroff, "Charged Excitons in Self-Assembled Semiconductor Quantum Dots," *Phys. Rev. Lett.*, vol. 79, no. 26, p. 5282, 1997.

[124] R. J. Coles, N. Prtljaga, B. Royall, I. J. Luxmoore, A. M. Fox, and M. S. Skolnick, "Waveguide-coupled photonic crystal cavity for quantum dot spin readout," *Opt. Express*, vol. 22, no. 3, pp. 2376–2385, 2014.

[125] J. H. Quilter, A. J. Brash, F. Liu, M. Glässl, A. M. Barth, V. M. Axt, A. J. Ramsay, M. S. Skolnick, and A. M. Fox, "Phonon-assisted population inversion of a single quantum dot," *arXiv*, 2014. arXivID: 1409.0913.

[126] A. Siegman, *Lasers*. Oxford: University Science Books, 1986.

[127] A. Leggett, S. Chakravarty, A. Dorsey, M. Fisher, A. Garg, and W. Zwerger, "Dynamics of the dissipative two-state system," *Rev. Mod. Phys.*, vol. 59, no. 1, pp. 1–85, 1987.

[128] D. E. Reiter, T. Khun, M. Glässl, and V. M. Axt, "The role of phonons for exciton and biexciton generation in an optically driven quantum dot," *J. Phys. Condens. Matter*, vol. 26, p. 423203, 2014.

[129] J. Petta, A. Johnson, C. Marcus, M. Hanson, and A. Gossard, "Manipulation of a Single Charge in a Double Quantum Dot," *Phys. Rev. Lett.*, vol. 93, p. 186802, Oct. 2004.

[130] T. M. Stace, A. C. Doherty, and S. D. Barrett, "Population Inversion of a Driven Two-Level System in a Structureless Bath," *Phys. Rev. Lett.*, vol. 95, p. 106801, Aug. 2005.

[131] J. I. Colless, X. G. Croot, T. M. Stace, A. C. Doherty, S. D. Barrett, H. Lu, A. C. Gossard, and D. J. Reilly, "Raman phonon emission in a driven double quantum dot.," *Nat. Commun.*, vol. 5, p. 3716, Jan 2014.

[132] M. Glässl, A. M. Barth, and V. M. Axt, "Proposed Robust and High-Fidelity Preparation of Excitons and Biexcitons in Semiconductor Quantum Dots Making Active Use of Phonons," *Phys. Rev. Lett.*, vol. 110, p. 147401, Apr. 2013.

[133] S. Hughes and H. J. Carmichael, "Phonon-mediated population inversion in a semiconductor quantum-dot cavity system," *New J. Phys.*, vol. 15, p. 053039, May 2013.

[134] B. Krummheuer, V. Axt, and T. Kuhn, "Theory of pure dephasing and the resulting absorption line shape in semiconductor quantum dots," *Phys. Rev. B*, vol. 65, p. 195313, May 2002.

[135] P. Borri, W. Langbein, U. Woggon, V. Stavarache, D. Reuter, and A. Wieck, "Exciton dephasing via phonon interactions in InAs quantum dots: Dependence on quantum confinement," *Phys. Rev. B*, vol. 71, p. 115328, Mar. 2005.

[136] S. Weiler, A. Ulhaq, S. M. Ulrich, D. Richter, M. Jetter, P. Michler, C. Roy, and S. Hughes, "Phonon-assisted incoherent excitation of a quantum dot and its emission properties," *Phys. Rev. B*, vol. 86, p. 241304, Dec. 2012.

[137] U. Hohenester, A. Laucht, M. Kaniber, N. Hauke, A. Neumann, A. Mohtashami, M. Seliger, M. Bichler, and J. J. Finley, "Phonon-assisted transitions from quantum dot excitons to cavity photons," *Phys. Rev. B*, vol. 80, p. 201311, Nov. 2009.

[138] K. H. Madsen, S. Ates, J. Liu, A. Javadi, S. M. Albrecht, I. Yeo, S. Stobbe, and P. Lodahl, "Efficient out-coupling of high-purity single photons from a coherent quantum dot in a photonic-crystal cavity," *Phys. Rev. B*, vol. 90, p. 155303, 2014.

[139] Y.-J. Wei, Y.-M. He, M.-C. Chen, Y.-N. Hu, Y. He, D. Wu, C. Schneider, M. Kamp, S. Höfling, C.-Y. Lu, and J.-W. Pan, "Deterministic and robust generation of single photons on a chip with 99.5% indistinguishability using rapid adiabatic passage," *Nano Letters*, vol. 14, no. 11, pp. 6515–6519, 2014.

[140] A. Vagov, M. D. Croitoru, M. Glässl, V. M. Axt, and T. Kuhn, "Real-time path integrals for quantum dots: Quantum dissipative dynamics with superohmic environment coupling," *Phys. Rev. B*, vol. 83, p. 094303, Mar. 2011.

[141] J. Förstner, C. Weber, J. Danckwerts, and a. Knorr, "Phonon-Assisted Damping of Rabi Oscillations in Semiconductor Quantum Dots," *Phys. Rev. Lett.*, vol. 91, p. 127401, Sept. 2003.

[142] E. Beham, A. Zrenner, S. Stu, F. Findeis, M. Bichler, and G. Abstreiter, "Coherent and incoherent properties of single quantum dot photodiodes," *Physica E*, vol. 16, p. 59, 2003.

[143] R. J. Warburton, B. T. Miller, C. S. Dürr, C. Bödefeld, K. Karrai, J. P. Kotthaus, G. Medeiros-Ribeiro, P. M. Petroff, and S. Huant, "Coulomb interactions in small charge-tunable quantum dots: A simple model," *Phys. Rev. B*, vol. 58, pp. 16221–16231, 1998.

[144] B. Urbaszek, R. J. Warburton, K. Karrai, B. D. Gerardot, P. M. Petroff, and J. M. Garcia, "Fine structure of highly charged excitons in semiconductor quantum dots," *Phys. Rev. Lett.*, vol. 90, p. 247403, 2003.

[145] E. R. Schmidgall, P. R. Eastham, and R. T. Phillips, "Population inversion in quantum dot ensembles via adiabatic rapid passage," *Phys. Rev. B*, vol. 81, p. 195306, May 2010.

[146] P.-L. Ardelt, L. Hanschke, K. A. Fischer, K. Müller, A. Kleinkauf, M. Koller, A. Bechtold, T. Simmet, J. Wierzbowski, H. Riedl, G. Abstreiter, and J. J. Finley, "Dissipative preparation of the exciton and biexciton in self-assembled quantum dots on picosecond time scales," *Phys. Rev. B*, vol. 90, p. 241404, 2014.

[147] S. Bounouar, M. Müller, A. M. Barth, M. Glässl, V. M. Axt, and P. Michler, "Phonon-assisted robust and deterministic two-photon biexciton preparation in a quantum dot," *arXiv*, 2014. arXivID: 1408.7027.

[148] A. Vagov, M. D. Croitoru, V. M. Axt, T. Kuhn, and F. M. Peeters, "Nonmonotonic Field Dependence of Damping and Reappearance of Rabi Oscillations in Quantum Dots," *Phys. Rev. Lett.*, vol. 98, p. 227403, June 2007.

[149] M. Glässl, M. D. Croitoru, A. Vagov, V. M. Axt, and T. Kuhn, "Influence of the pulse shape and the dot size on the decay and reappearance of Rabi rotations in laser driven quantum dots," *Phys. Rev. B*, vol. 84, p. 125304, Sept. 2011.

[150] R. J. Coles, "Towards a single slectron source using coherent voltage modulation of InAs quantum dots." MSc Dissertation, University of Sheffield, August 2011.